Relaxation dynamics of granular-heap structure under vertical vibration

鉛直振動下における粉体ヒープ構造の緩和ダイナミクス

TSUJI, Daisuke

辻　大輔

A dissertation for the degree of Doctor of Science

Department of Earth and Environmental Sciences,
Graduate School of Environmental Studies, Nagoya University

名古屋大学大学院環境学研究科地球環境科学専攻学位論文　博士（理学）

2020

Acknowledgement

First and foremost I would like to express my sincere gratitude to my supervisor, Dr Hiroaki Katsuragi. He gave me an opportunity to be involved in granular physics, and has supervised me throughout my university life in Nagoya University. He always understood and accepted my thoughts, research idea, and career plan. When I faced problems in the research, he gave me various suggestions based on his comprehensive knowledge and experience. It has been an honour to study in his research group.

I am also deeply indebted to Dr Michio Otsuki, who is a collaborator of this research. He taught me numerical programming, and also gave me insightful comments, which often helped me to determine the direction of this research. Without his support, especially the numerical part in this study would never have been completed.

While I researched overseas, two professors kindly supervised me. In University of Bristol, Dr Nick Teanby offered me the research project on cratering processes and planetary seismology. Looking backwards, I feel that this experience highly inspired me to connect granular physic with planetary science. On the other hand, during the stay in The University of Manchester, Dr Nico Gray let me join the research group which investigates granular flow from mathematical approaches. This visit brought me different perspectives particularly on the continuum modelling, and also provided me with chances to introduce this research to many overseas researchers. I am sincerely grateful to these two supervisors.

In addition, I received invaluable feedbacks to improve the quality of this dissertation from the thesis committee: Dr Sei-ichiro Watanabe, Dr Toshiki Watanabe, and Dr Ikuro Sumita. Besides them, I would like to thank Dr David Schaeffer, Dr Thomas Barker, Dr Sumiyoshi Abe, Dr Sin-iti Sirono, Dr Tomokatsu Morota, Dr Hiroyuki Kumagai, and Dr Hirofumi Niiya for helpful discussions and advices. My thanks goes as well to all of the faculty members and my phd friends who supported my university life.

Last but not least, many thanks from the bottom of my heart to my family. They always backed me up in this long journey, which encouraged me to overcome difficulties many times.

Abstract

This study aims to build the continuum model for granular flow driven by vertical vibration. To this end, we investigate the relaxation dynamics of a vertically-vibrated granular heap by means of both laboratory experiment and numerical simulation. In the experiment, a conical granular heap with the angle of repose is subjected to vertical vibration. As a result, grains are fluidised and the morphological structure of the heap is gradually relaxed. To quantify the flow property, the surface profile of the relaxing heap is recorded by a high-speed laser profiler. The continuum model, which can describe how the depth-averaged velocity of the granular flow is determined, is then derived to explain the experimental data. This model is based on the previous work (Roering *et al.*, Water Resour. Res. **35**, 853–870, 1999), and named the nonlinear diffusion transport (NDT) model. In the NDT model, a new parameter is introduced, which represents the energy conversion efficiency from vertical vibration into horizontal granular transport. We demonstrate that this parameter is nearly constant (~ 0.1) by comparing the experimental data obtained under various conditions. This universality implies that only approximately 10% of the vibration energy are used for the transport of granular media in any vibration condition. Next, to explore the flow mechanism from more particle-scale point of view, numerical simulations on a basis of the discrete element method (DEM) are also conducted. We numerically reproduce the laboratory experiment, and investigate the internal velocity profile, which is difficult to access by experimental data. The numerical result shows that the flow velocity exponentially decays as going deeper from the surface, which is consistent with previous studies of granular-heap flows. However, the remarkable difference is that the characteristic thickness of the clearly-fluidised region (i.e., shear band) grows proportionally with the height of the heap. This variable shear band structure is in contrast to the conventional understanding that the thickness of the shear band is constant everywhere. We also prove that the integration of the internal velocity profile is consistent with the depth-averaged velocity predicted by the NDT model. Finally, to show the applicability of these results in geophysics, the NDT model is implemented into the crater relaxation model on asteroid Itokawa caused by impact-induced seismic shaking, and then the typical crater size erased by a single impact is estimated.

Contents

List of Figures

List of Tables

1 Research background

1.1 Overview

1.1.1 Introduction to granular matter

Granular matter is ubiquitous around our everyday life (figure 1.1). This material is usually defined as a collection of macroscopic rigid and dissipative particles (Katsuragi, 2016). Almost all people, on a daily basis, touch granular matter like food products (e.g., rice, corn, sugar, coffee beans, and breakfast cereal flakes). We also handle granular matter in numerous industrial situations, including construction, mining, agriculture, food production, pharmaceutical manufacture, and so on. In fact, more than half of the commodities used and consumed in the world are produced using granular materials at some stage (Bates, 2006). Since granular matter is the second most encountered material next to water in industry, any progress in handling and processing it could have an enormous impact on society and economy (Duran, 2000; Richard et al., 2005).

Science of granular matter has a long history, and has been of interest to many researchers including notable names. For example, Coulomb (1773), who is a pioneer of this research area in modern science, proposed the idea of static friction, Faraday (1831) revealed convective instability in vibrated powders, and Reynolds (1885) discovered dilatancy in sheared granular media. To date, various empirical knowledges have been accumulated from an engineering point of view due to the importance of solving problems related industry (e.g., storage, transportation, flow, and mixing). Particularly over the last several decades, the study of granular matter, which presents abundant phenomenology, has also fascinated a wide range of physicist in soft-matter physics, fluid physics, statistical physics, nonlinear physics, etc. However, the underlying physics, especially constitutive relations of granular dynamics, are relatively little known. In this sense, our fundamental understanding of granular matter is still limited, and it is thus desirable to keep developing the general theory, which could also optimise the way of controlling grains beyond the current common method in industry.

The benefit is also brought to some related areas of geoscience. Most geomorphological structures on the Earth involve granular matter, which plays a crucial role in the

formation process of landforms. In terms of natural disaster, as we can easily imagine, throughout history human beings have suffered from natural granular flows, such as landslide, volcanic ash flow, and debris flow. To minimise their risks, researching granular matter must be important. Moreover, we should not overlook that handling granular matter comes up for discussion even in planetary exploration. Surfaces of many rocky planets like Mars and Moon are covered with a fluffy granular bed called regolith. Therefore, a spacecraft which attempts a soft landing on any astronomical objects needs to expect the stability of the granular bed.

Figure 1.1: Examples of granular matter: (a) sugar, (b) cereal, (c) pill, and (d) sand. These images are available from
(a) https://pixabay.com/photos/sugar-calories-sweet-food-1068288/
(b) https://pixabay.com/photos/grains-food-texture-cereals-grain-4291788/
(c) https://pixabay.com/photos/headache-pain-pills-medication-1540220/
(d) https://pixabay.com/photos/dune-dunes-oman-desert-sunset-3985396/

1.1.2 Classification

According to the classification employed by Andreotti et al. (2013), the size range of a granular medium is larger than 100 μm, which this study focuses on. This macroscopic scale keeps granular matter athermal. In most cases, the interactions among grains basically work through friction and collision under Earth gravity. Smaller particles, of diameter between 1 μm and 100 μm, are classified as powder. In this size range, the interactions of air drag forces, van der Waals forces, humidity, and electric charges are no longer negligible. Regarding even smaller particles of diameter less than 1 μm, which are not visible to the naked eye, thermal agitation needs to be additionally considered.

The terms "granular matter" and "powder" usually represent dry grains. When immersed in some liquid, the terms "wet granular media" and "suspensions" are rather used. Although these materials are beyond the scope of this thesis, in general cohesive forces present rich physical properties such as cluster formation (Takada et al., 2014) and stable void structure (Shinoda et al., 2018).

1.1.3 Angle of repose

Granular matter shows both solid-like and fluid-like behaviours. When a flat granular bed is tilted, its stability can be kept like solid as long as the slope is less than a certain critical angle. However, once the inclination exceeds that certain angle, granular media begin to flow like fluid. This critical angle which differentiates these two states is called the angle of repose θ_c. In other words, the slope of a granular heap capable of holding its own stable structure is always less than or equal to the angle of repose.

There are uncountable applications of the angle of repose. For the geotechnical purpose, the angle of repose can be an indicator to judge whether the slopes are safe in mountainous areas. Figure 1.2 shows an example of the angle of repose created by nature. Even in the field of agricultural engineering, the angle of repose is practically utilised to characterise wheat moisture content. Zaalouk and Zabady (2009) report that the angle of repose increases linearly with moisture content for several kinds of wheat. In statistical physics, granular system around the angle of repose can also be regarded as being in a critical state, where power law statistics appears. Bak et al. (1987) developed a cellular automa-

Figure 1.2: Angle of repose on a dune in Great Sand Dunes National Park and Preserve, United States. An avalanche occurs when the slope increases and reaches the angle of repose due to the transport of particles by wind. This image is available from `https://www.flickr.com/photos/greatsanddunesnpp/46116909755/`

ton model to mimic avalanches on sandpiles with the angle of repose, and proposed the physical concept of self-organised criticality (SOC). The framework of SOC has been extended to many critical phenomena, such as earthquakes (Bak and Tang, 1989), volcanic events (Diodati et al., 1991), and granular deformation (Tsuji and Katsuragi, 2015).

What physical property determines the angle of repose θ_c for dry granular media? Microscopically, the granular network structure is sustained by the friction at the contact point between grains (Katsuragi, 2016). The simplest but commonly accepted idea is that, from analogy with the classical Amontons-Coulomb's friction law, $\tan\theta_c$ is approximately equal to the friction coefficient of bulk granular media μ:

$$\tan\theta_c \approx \mu, \tag{1.1}$$

where μ also physically corresponds to the static friction coefficient μ_s. Note that the macroscopic friction property of bulk granular media is not necessarily identical to the

microscopic frictional property of a single grain. There are numerous methods to measure the angle of repose, which slightly depends on the preparation process, geometrical setup, and boundary conditions. Al-Hashemi and Al-Amoudi (2018) extensively review the definition, measurement method, application, and influencing factors for the angle of repose.

Strictly speaking, the angle of repose θ_c is distinguished from the angle of movement θ_m (Duran, 2000). These two critical angles can be easily observed using a rotating drum filled with granular media. While a drum is rotated very slowly, a granular layer keeps a flat surface tilted angle θ to a horizontal plane. When θ reaches θ_m, an avalanche occurs and halts when θ is relaxed to θ_c. In this sense, $\mu = \tan\theta_m$ can be another option for the frictional law. However, in any case, the difference of these two critical angles $\delta\theta_{mc} = \theta_m - \theta_c$, which is called relaxation angle, is only $\simeq 2^\circ$ for dry granular media (Liu et al., 1991; Duran, 2000). In addition to this, the measurement of θ_c is easier than θ_m in most cases. Therefore, the simple relation (1.1) is often used when a friction law is implemented into a physical model (Katsuragi, 2016).

1.1.4 Focus point

Steady granular flows driven by gravity, which are usually observed with an angle steeper than the angle of repose, have long been studied by many researchers. In spite of continuous efforts, we have not yet established unified governing equations which can cover a diversity of granular-flow dynamics, like the one corresponding to the Navier-Stokes equations in classical fluid dynamics. To understand its fundamental physics step by step, granular flows are often divided into three different regimes (Jaeger et al., 1996): (i) gaseous regime in which the flow is very rapid and dilute and particles are agitated and interact mostly by binary collisions (Goldhirsch, 2003). (ii) dense flow (liquid-like) regime in which grains are dense but still flow like liquid and their interactions are characterised by both collisions and long-lived contacts (Pouliquen and Chevoir, 2002; GDR MiDi, 2004). (iii) quasi-static (solid-like) regime in which the deformation is very small and grains interact by only friction (Roux and Combe, 2002). Figure 1.3 illustrates the image of these three regimes. (ii) Liquid-like regime, which lies between two extreme

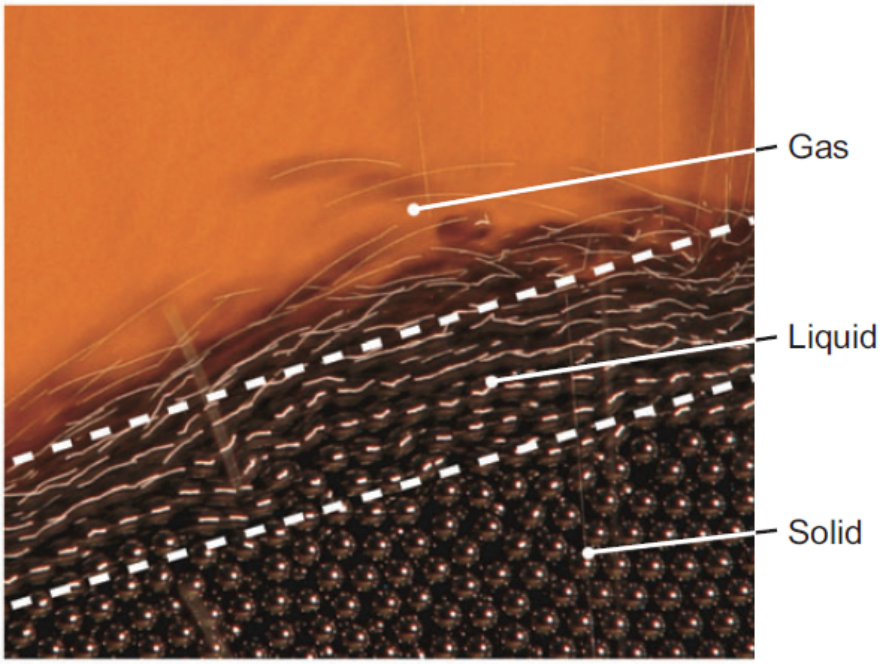

Figure 1.3: Illustration of the solid-like, liquid-like, and gaseous regimes for granular flow, obtained by pouring steel beads on a pile. Cited from Forterre and Pouliquen (2008).

cases: (i) gaseous regime and (iii) solid-like regime, is the one that we encounter in nature, industry, and everyday life most frequently. The focus of this thesis centres on this liquid-like regime, and we discuss the possibility of a continuum description on dense granular flows.

Although remarkable progresses in our understanding of constitutive relations for dense granular flow have been made so far, there are still many limitations in terms of their applicability. For example, using proposed constitutive relations, the dynamics of gravity-driven granular flows can be explained to some extent independent of geometrical configurations. However, when the system is subjected to disturbance, the same modelling cannot be applied because the rheology of granular matter dramatically changes. This can be imagined from our everyday experience: when a sandpile is shaken, grains are fluidised and surface flows are induced, even if the slope is less than the angle of repose (Jaeger et al., 1989). More technically, we can observe other various phenomena peculiar to vibro-fluidised granular matter, such as convection (Yamada and Katsuragi, 2014), segregation (Breu et al., 2003), compaction and dilation (Nowak et al., 1997; Iikawa et al.,

2015), friction weakening (Caballero-Robledo and Clément, 2009), decrease and increase in the angle of repose (Amon et al., 2013; Swisher and Utter, 2014), undulation (Sano, 2005), granular Leidenfrost (Eshuis et al., 2005). At present relatively few have been revealed regarding the fundamental mechanism of granular flows under vibration, although this vibratory fluidity appears in widespread areas of industry.

The final goal of this thesis is to promote a better understanding of vibration-induced dense granular flows, particularly surface flows, through systematic experiments and simulations. In the rest of this section, previous literatures related to this thesis are reviewed. To begin with, as a general introduction to dense granular flows, section 1.2 summarises the current understanding of the fundamental granular rheology in the absence of disturbance, and then deals with gravity-driven granular flows. Next, some key works more directly associated with the goal of this thesis are introduced in section 1.3. As commented above, the rheological model developed for gravity-driven flows (section 1.2) cannot be applied to vibration-driven flows, and different theoretical approaches are in general required. Although section 1.3 contrasts with 1.2, there are a little in common and therefore it would be helpful to introduce both gravity-driven and vibration-driven flows in this thesis. Finally, the aim and objective of this thesis are specified in section 1.4.

1.2 Rheology of granular flow

From a phenomenological point of view, dense granular flows can be considered to belong to the viscoplastic family because: materials do not flow until the stress exceeds the frictional resistance, which corresponds to the existence of yield stress as in a Bingham plastic; and at the same time the shear-rate dependence is observed when materials flow, which implies a viscous-like property (Forterre and Pouliquen, 2008). The key of understanding dense granular flows is how to relate the stress to the shear rate, which can be constrained by a dimensional analysis (Andreotti et al., 2013; Jop, 2015).

First of all, in section 1.2.1–1.2.3 we introduce the concept of the local rheology, which gives widely accepted constitutive relations for granular-flow dynamics. Additionally, it enables quantitative grouping of three regimes shown in figure 1.3. This rheological model is then applied to two configurations in which gravity-driven flows are observed: flow down an inclined plane (section 1.2.4) and flow on a granular pile (section 1.2.5). In the latter case, the sliding-block approximation, which is a very useful strategy in modelling granular flows, is also introduced.

1.2.1 Constitutive relation

To build constitutive relations, let us consider the simplest configuration that granular materials, of diameter d and material density ρ, are submitted to plane shear without gravity as illustrated in figure 1.4. Two parallel rough plates which confine particles are distance L apart from each other. With the bottom plate fixed, the top plate is horizontally slid with velocity V_{W} and confining (normal) pressure P. In a steady state without gravity, the shear stress τ and the normal stress P can be assumed to be homogeneous throughout the system, and the shear rate $\dot{\gamma} \equiv V_{\mathrm{W}}/L$ is therefore uniformly observed.

The number of relevant parameters in this problem are four: grain diameter d, grain density ρ, shear rate $\dot{\gamma}$, and confining pressure P. Note that here two conditions are assumed: the system size is sufficiently large compared to particle size (i.e., $L \gg d$) so that the distance between the plates plays no role; and particles are rigid enough to neglect the role of elasticity (i.e., $E \gg P$, where E is Young's modulus of particles). The Buckingham π theorem (Buckingham, 1914, 1915) enables us to derive a dimensionless parameter

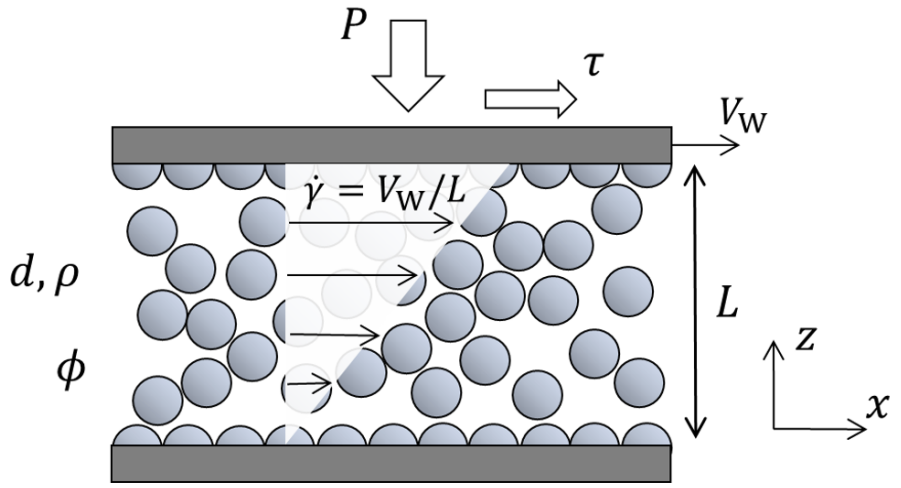

Figure 1.4: Plane shear.

using above four relevant parameters. Since the fundamental dimensions are three (mass **M**, length **L**, and time **T**), we can obtain one dimensionless parameter ($4 - 3 = 1$):

$$I = \frac{\dot{\gamma} d}{\sqrt{P/\rho}}. \tag{1.2}$$

This dimensionless number is called the inertial number. Other expressions are also possible, such as $\rho d^2 \dot{\gamma}^2 / P$ known as the Savage number (Savage, 1984) or the Coulomb number (Ancey et al., 1999). The inertial number I can be regarded as the ratio of two timescales, $\dot{\gamma}^{-1}$ and $d/\sqrt{P/\rho}$ (GDR MiDi, 2004). The former is a macroscopic timescale related to the shear rate, which is linked to the mean deformation. The latter is a microscopic timescale related to the grain rearrangements due to the confining pressure. As I increases, the system gets closer to the gaseous regime ($0.2 \leq I$), while the low I value means the quasi-static regime ($I \leq 10^{-2}$) (Andreotti et al., 2013). The intermediate ranges ($10^{-2} \leq I \leq 0.2$) correspond to the dense flow regime.

This dimensional analysis can impose the following two relationships: The packing (volume) fraction ϕ, which is dimensionless as well, is a function of only I. The shear stress τ is proportional to the normal stress P. In other words, the dimensional analysis

can give the following friction and dilatancy laws:

$$\tau = \mu(I)P, \tag{1.3}$$

$$\phi = \Phi(I), \tag{1.4}$$

where μ corresponds to an effective friction coefficient which depends on only I. Their validity has been verified by the discrete-element-method (DEM) simulation of plane shear (da Cruz et al., 2005). These relations also satisfy the Bagnold scaling (i.e., $\tau \sim \dot{\gamma}^2$), which is derived by the collisional-momentum transfer analysis (Bagnold, 1954).

There are several phenomenological equations proposed for $\mu(I)$ and $\Phi(I)$ in the dense flow regime. One of the most commonly accepted expressions, which was originally proposed by Jop et al. (2005); Pouliquen et al. (2006), is:

$$\mu(I) = \mu_{\min} + \frac{\mu_{\max} - \mu_{\min}}{I_0/I + 1}, \tag{1.5}$$

$$\Phi(I) = \phi_{\max} - (\phi_{\max} - \phi_{\min})I, \tag{1.6}$$

where coefficients are the intrinsic values of granular materials. In the case of glass beads, those typical values are $\mu_{\min} = \tan 21^\circ$, $\mu_{\max} = \tan 33^\circ$, $I_0 = 0.3$, $\phi_{\max} = 0.6$, $\phi_{\min} = 0.4$ (Forterre and Pouliquen, 2008). The DEM simulations performed by da Cruz et al. (2005) have revealed that these parameters are not influenced by the restitution coefficient of particles. The I-dependent friction and dilatancy laws (1.5) and (1.6) are drawn in figure 1.5. For the friction law (1.5), $\mu(I)$ saturates to $\mu_{\max}$ as I increases, whereas $\mu_{\min}$ is the minimum value of $\mu(I)$ in the limit of $I \to 0$, i.e., the materials are not sheared. Actually, da Cruz et al. (2005) have proposed another linear I-dependent frictional law:

$$\mu(I) = \mu_0 + bI, \tag{1.7}$$

where μ_0 and b are constants. However, they also report that saturation of μ in $I \geq 0.2$ is observed as in figure 1.5(a). In this regard, the linear frictional model of da Cruz et al. (2005) is qualitatively similar to the frictional law (1.5) proposed by Jop et al. (2005).

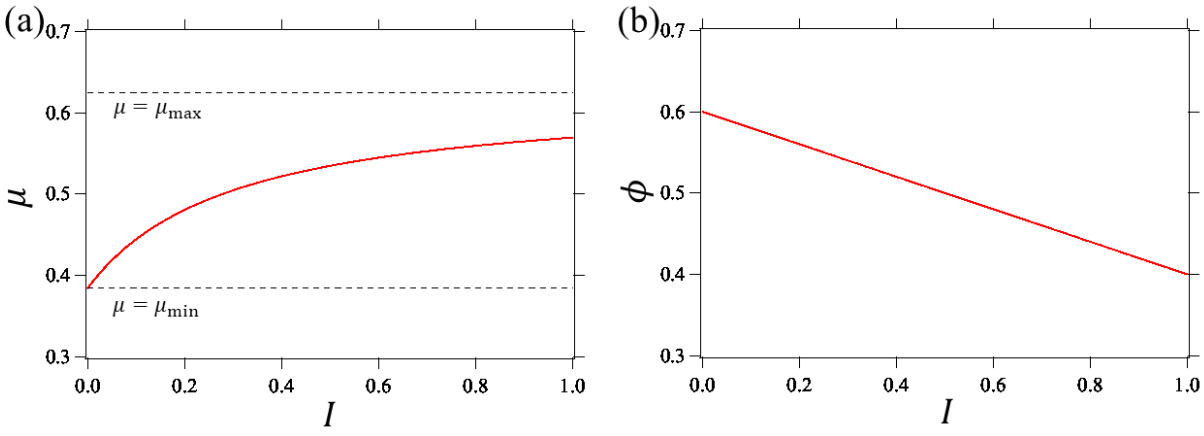

Figure 1.5: (a) Friction coefficient μ and (b) packing fraction ϕ as a function of the inertial number I. The functional forms of panels (a) and (b) are given by equations (1.5) and (1.6).

Here, it is worth noting again that the friction and dilatancy laws (1.5) and (1.6) are applicable only to the dense flow regime ($10^{-2} \leq I \leq 0.2$). In the gaseous regime ($I \leq 0.2$), their validity has not yet been tested well. Additionally, in experiments, steady homogeneous flows with high I values are difficult to achieve due to instabilities (Jop, 2015). As for the solid-like regime ($I \leq 10^{-2}$), Kuwano et al. (2013) have observed velocity weakening of friction in contrast to velocity strengthening in figure 1.5(a).

Provided that the above friction and dilatancy laws, which are obtained from homogeneous flows under plane shear, locally hold for inhomogeneous flows even in a nonsteady situation, we can easily predict velocity profiles in any configuration as well. Namely, equations (1.3)–(1.6) can be considered as the constitutive relations, if the stress depends only on the local shear rate and the local pressure. This idea is called the local rheology, the validity of which has been empirically supported by many experiments and simulations. For example, Forterre and Pouliquen (2008); Andreotti et al. (2013) collected $\mu(I)$ and $\Phi(I)$ data which are both experimentally and numerically obtained in various configurations, such as plane shear, rotating drum, inclined plane, and cylindrical Couette cell. They report that the collected data are collapsed and take identical forms of figure 1.5, thereby supporting the argument of the local rheology.

1.2.2 Tensorial formulation

To describe complex flows submitted to unidirectional shear, the generalisation of the simple scalar laws (equations (1.3) and (1.4)) to a tensorial formulation is needed. In two dimensions (to which the discussion here is restricted), the symmetric Cauchy stress tensor σ_{ij} can be decomposed into an isotropic pressure $P = -\sigma_{ii}/2$ plus a trace free tensor τ_{ij}, called the shear-stress tensor or the deviatoric stress:

$$\sigma_{ij} = -P\delta_{ij} + \tau_{ij}, \tag{1.8}$$

where δ_{ij} is the Kronecker delta function. Along with this tensorisation, the frictional law (1.3) is read as

$$||\boldsymbol{\tau}|| = \mu(I)P, \tag{1.9}$$

where the notation $||\boldsymbol{T}|| = \sqrt{\mathrm{tr}(\boldsymbol{T}^2)/2}$ denotes the second invariant of any symmetric tensor $\boldsymbol{T}$.

In the incompressible limit where the packing fraction is constant, the strain-rate tensor D_{ij} is given by

$$D_{ij} = \frac{1}{2}(\partial_j u_i + \partial_i u_j), \tag{1.10}$$

where u_i is a component of the flow velocity vector $\boldsymbol{u}$. The constitutive relation for the incompressible $\mu(I)$ rheology (Jop et al., 2006; Barker et al., 2015, 2017) is then described as

$$\tau_{ij} = \eta_{\mathrm{eff}} D_{ij}, \tag{1.11}$$

with

$$\eta_{\mathrm{eff}} = \frac{\mu(I)P}{||\boldsymbol{D}||}, \tag{1.12}$$

$$I = \frac{2d||\boldsymbol{D}||}{\sqrt{P/\rho}}. \tag{1.13}$$

Note that, to derive these relations, the assumption of the alignment below is imposed:

$$\frac{\tau_{ij}}{||\boldsymbol{\tau}||} = \frac{D_{ij}}{||\boldsymbol{D}||}, \tag{1.14}$$

which suggests that eigenvectors of the deviatoric stress tensor and the shear-rate tensor are parallel.

For compressible flows, isochoric deformations (pure shear) should be separated from the deformations related with a net change in volume. Therefore, it is practical to define the deviatoric strain-rate tensor S_{ij} as follows:

$$S_{ij} = D_{ij} - \frac{1}{2}(\operatorname{div} \boldsymbol{u})\delta_{ij}, \tag{1.15}$$

where S_{ij} is trace free. As with equations (1.11)–(1.13), the constitutive relations for the compressible $\mu(I)$ rheology (Heyman et al., 2017; Schaeffer et al., 2019) are given by

$$\tau_{ij} = \eta_{\text{eff}} S_{ij} \tag{1.16}$$

$$\phi = \Phi(I), \tag{1.17}$$

with

$$\eta_{\text{eff}} = \frac{\mu(I)P}{||\boldsymbol{S}||}, \tag{1.18}$$

$$I = \frac{2d||\boldsymbol{S}||}{\sqrt{P/\rho}}, \tag{1.19}$$

where the following alignment is also assumed:

$$\frac{\tau_{ij}}{||\boldsymbol{\tau}||} = \frac{S_{ij}}{||\boldsymbol{S}||}. \tag{1.20}$$

The constitutive laws (1.16)–(1.20) are also referred to as the $\mu(I)$, $\Phi(I)$-rheology.

In the above expression, η_{eff} can be read as the effective viscosity of dense granular flows, which depends on both the pressure and local deformation rate unlike a constant viscosity as in a Newtonian fluid. The governing equations for granular flows that resemble the Navier-Stokes equations can be easily derived by combing this effective viscosity with the mass conservation equation:

$$(\partial_t + u_j \partial_j)\phi + \phi \operatorname{div} \boldsymbol{u} = 0, \tag{1.21}$$

and the momentum conservation equation:

$$\rho\phi(\partial_t + u_j\partial_j)u_i = \partial_j\sigma_{ij},, \qquad i = 1, 2, \tag{1.22}$$

where the body force is not considered here.

These continuum modelling has led to significant progresses in modelling various granular flows (e.g., Jop et al., 2006; Lagrée et al., 2011; Gray and Edwards, 2014; Baker et al., 2016). However, Barker et al. (2015) have shown that the $\mu(I)$-rheology for two-dimensional flows is mathematically ill-posed for a large range of I (particularly very high and low I regimes). As an extension to this, Heyman et al. (2017) have revealed that the compressible $\mu(I)$-rheology is also effectively ill-posed (or unstable) in a certain condition. The ill-posedness of these models suggests that infinitesimally small perturbations in time-dependent simulations may grow at an unbounded rate in the limit that their wavelength tends to zero, which is also known as Hadamard instability (Joseph and Saut, 1990). As an example of this failure, Schaeffer et al. (2019) have demonstrated that a simulation using the $\mu(I)$, $\Phi(I)$-rheology blows up under the initial condition with a small perturbation even in a very simple problem (flow in a two-dimensional gravity-free shear cell). This behaviour is unrealistic as all physical systems more or less suffer from noise but do not blow up catastrophically, implying the possibility that some important physics is missing or the model has not been properly formulated. Therefore, for complete practical applications of the continuum model, a well-posed theory would be in general more desired. One attempt to cover this problem is briefly introduced below.

1.2.3 Inertial compressible I-dependent rheology

For compressible flows, Barker et al. (2017) modify two constitutive relations (1.16) and (1.17), retaining the others (1.18)–(1.20). Firstly, the deviatoric stress is given by

$$||\boldsymbol{\tau}|| = Y(P, I, \phi), \tag{1.23}$$

where Y, called the yield function, includes the dependence on ϕ. Secondly, by referring to critical state soil mechanics (Schofield and Wroth, 1968; Jackson, 1983), the volumetric

change evolves based on the flow rule:

$$\operatorname{div} \boldsymbol{u} = 2F(P, I, \phi)\|\boldsymbol{S}\|, \tag{1.24}$$

where F is called the dilatancy function. Barker et al. (2017) have also proved that the governing equation is linearly well-posed as long as all of the three conditions below are satisfied:

$$\frac{\partial Y}{\partial P} - \frac{I}{2P}\frac{\partial Y}{\partial I} = F + I\frac{\partial F}{\partial I}, \tag{1.25}$$

$$\frac{\partial Y}{\partial I} > 0, \tag{1.26}$$

$$\frac{\partial F}{\partial P} - \frac{I}{2P}\frac{\partial F}{\partial I} < 0. \tag{1.27}$$

They name this general framework compressible I-dependent rheology (CIDR). In principle, CIDR is able to model granular material in any regime, although there are numerous choices for Y and F leading to well-posed equations. Schaeffer et al. (2019) have determined these two functions as follows so that the $\mu(I), \Phi(I)$-rheology (1.5) and (1.6) can be reproduced in steady states:

$$Y(P, I, \phi) = \mu(\Psi(\phi))\frac{I}{\Psi(\phi)}P, \tag{1.28}$$

$$F(I, \phi) = \frac{1}{4}\mu(\Psi(\phi))\left[\frac{I}{\Psi(\phi)} - \frac{\Psi(\phi)}{I}\right], \tag{1.29}$$

where $\Psi(\phi)$ is the inverse function of $\Phi(I)$. Since these functions satisfy equation (1.25)–(1.27), the dynamic equations of the iCIDR rheology are guaranteed to be well-posed for any deformation and packing fraction. Schaeffer et al. (2019) terms this theory the inertial CIDR or iCIDR because, as explained later, it captures the inertial regime where (liquid-like) dense flows exhibiting the Bagnold scaling are observed.

In the $\mu(I), \Phi(I)$-rheology, I is rigidly tied to ϕ through $I = \Psi(\phi)$. In contrast, I in the iCIDR evolves through the flow rule (1.24) with the dilatancy function (1.29).

Substituting equation (1.29) into equation (1.24) yields the quadratic equation for I:

$$I^2 - 2\frac{\Psi(\phi)\,\mathrm{div}\,\boldsymbol{u}}{\mu(\Psi(\phi))\,\|\boldsymbol{S}\|}I - \Psi(\phi)^2 = 0, \tag{1.30}$$

where the solution with the positive root is

$$I = \frac{\Psi(\phi)\,\mathrm{div}\,\boldsymbol{u}}{\mu(\Psi(\phi))\|\boldsymbol{S}\|} + \sqrt{\left(\frac{\Psi(\phi)\,\mathrm{div}\,\boldsymbol{u}}{\mu(\Psi(\phi))\|\boldsymbol{S}\|}\right)^2 + \Psi^2(\phi)}. \tag{1.31}$$

From this relation, I is a function of the packing fraction ϕ and the ratio $\mathrm{div}\,\boldsymbol{u}/\|\boldsymbol{S}\|$. Of course, for steady isochoric (constant volume) flows, equation (1.31) reduces to $I = \Psi(\phi)$, which corresponds to the inertial number in the $\mu(I)$, $\Phi(I)$-rheology. Using I defined by equation (1.31), an equation of state for the pressure can be given by equation (1.19) as

$$P = \rho\left(\frac{2d\|\boldsymbol{S}\|}{I}\right)^2. \tag{1.32}$$

This equation satisfies the Bagnold scaling, because I defined by equation (1.31) depends on the velocity only through the ratio $\mathrm{div}\,\boldsymbol{u}/\|\boldsymbol{S}\|$, which is constant even if scaling the velocity.

However, one problem arises when calculating the pressure by equation (1.32). In the limit of $\|\boldsymbol{S}\| \to 0$, I defined by equation (1.31) approaches either zero or infinity, depending on the sign of $\mathrm{div}\,\boldsymbol{u}$, which may lead to the breakdown of the iCIDR constitutive laws. To avoid this, the calculation of I like equation (1.31) is bypassed by substituting equation (1.19) into equation (1.30), which enables us to directly obtain an alternative expression for pressure:

$$P = \rho\left(\frac{2d}{\mu(\Psi(\phi))\Psi(\phi)}\right)^2 \left[\sqrt{(\mathrm{div}\,\boldsymbol{u})^2 + \mu(\Psi(\phi))^2\|\boldsymbol{S}\|^2} - \mathrm{div}\,\boldsymbol{u}\right]^2, \tag{1.33}$$

which is well defined for all deformation rates. Finally, from equations (1.19), (1.20), (1.23), and (1.28), the deviatoric shear stress can be expressed as

$$\tau_{ij} = \frac{2d\sqrt{\rho}\mu(\Psi(\phi))}{\Psi(\phi)}\sqrt{P}\,S_{ij}, \tag{1.34}$$

which is also well defined for all deformation rates.

One might suspect whether the iCIDR appropriately captures the real behaviour of granular materials as the yield function Y (1.28) and the dilatancy function F (1.29) are just chosen to satisfy the well-posedness (1.25)–(1.27) and the $\mu(I)$, $\Phi(I)$-rheology in steady states, and there are no other theoretical supports. However, Schaeffer et al. (2019) have also performed time-dependent DEM simulations to test their validity, and consequently demonstrated that the iCIDR can correctly predict the simulated particles in a gravity-free shear cell. Although a more variety of investigations are needed, the iCIDR, which preserves the success of the $\mu(I)$, $\Phi(I)$-rheology, is a significant step for well-posed constitutive relations of granular flows.

In the following, the dynamics of gravity-driven flows under two different configurations is considered based on the idea of the local rheology introduced so far. For simplicity, we treat granular flows only in steady states under incompressible assumption, which means that only the framework of the $\mu(I)$-rheology (1.3) and (1.5) are basically used as the constitutive relation below.

1.2.4 Flow down an inclined plane

Firstly, the local rheology is applied to a steady granular flow down a rough inclined plane with slope θ (figure 1.6(a)). Granular materials are continuously supplied from the reservoir through a precisely controlled gate. When flows are steady and uniform, assuming the hydrostatic pressure, $\partial\tau/\partial z = -\rho_\phi g \sin\theta$ and $\partial P/\partial z = -\rho_\phi g \cos\theta$, where $\rho_\phi = \rho\,\phi$ (the bulk density of granular media) and g is the gravitational acceleration. Let $z = h$ be at the free surface of the flows, where τ and P vanish. Integrating $\partial\tau/\partial z$ and $\partial P/\partial z$ throughout the layer, the stress distribution can be given by $\tau = \rho_\phi g \sin\theta\,(h-z)$ and $P = \rho_\phi g \cos\theta\,(h-z)$. To predict the velocity profile as a function of depth $u(z)$, the above expressions are substituted into equations (1.2) and (1.3):

$$\mu(I) = \tan\theta \qquad \text{with} \qquad I = \frac{u'(z)\,d}{\sqrt{g\phi\cos\theta\,(h-z)}}, \tag{1.35}$$

where $u'(z) \equiv du/dz \equiv \dot{\gamma}$. Since I is constant across the layer, ϕ is also constant independent of z. Using equation (1.35) with the constitutive relation (1.5), the velocity gradient can be expressed as

$$u'(z) = I_0 \frac{\tan\theta - \mu_{\min}}{\mu_{\max} - \tan\theta} \sqrt{\frac{g\phi\cos\theta\,(h-z)}{d^2}}. \tag{1.36}$$

The velocity profile is then derived by integrating this velocity gradient from $z = 0$ to $z = h$:

$$\frac{u(z)}{\sqrt{gd}} = \frac{2}{3} I_0 \frac{\tan\theta - \mu_{\min}}{\mu_{\max} - \tan\theta} \sqrt{\phi\cos\theta} \left(\frac{h^{3/2} - (h-z)^{3/2}}{d^{3/2}} \right), \tag{1.37}$$

where the no-slip boundary condition $u(z = 0) = 0$ is imposed. This profile is obviously different from a Newtonian fluid showing a parabolic velocity profile derived from the steady Navier-Stokes equation under the no-slip boundary condition. The velocity profile exhibiting $u(z) \propto h^{3/2} - (h-z)^{3/2}$ is called the Bagnold profile, which can also be derived by the Bagnold scaling (Bagnold, 1954; Silbert et al., 2001, 2003). Finally, the depth-averaged velocity $\langle u \rangle = (1/h) \int_0^h u(z)\, dz$ is expressed as

$$\frac{\langle u \rangle}{\sqrt{gh}} = \frac{2}{5} I_0 \frac{\tan\theta - \mu_{\min}}{\mu_{\max} - \tan\theta} \sqrt{\phi\cos\theta}\, \frac{h}{d}. \tag{1.38}$$

The velocity structure presented here captures most primary behaviours of actual granular materials. The flow threshold is firstly compared. Equation (1.38) states that steady and uniform flows can be produced only when θ is between the minimum angle $\theta_{\min} = \tan^{-1}\mu_{\min}$ and the maximum angle $\theta_{\max} = \tan^{-1}\mu_{\max}$. This prediction qualitatively agrees with both experimental and numerical observations (Pouliquen, 1999; Silbert et al., 2001), which show that steady and uniform flows occur only within a limited range of the inclination. However, more specifically, the minimum angle $\theta_{\min}$ depends on the thickness h as shown in figure 1.6(b), where θ increases as the thickness h decreases, which cannot be predicted by the local rheology. Kamrin and Henann (2015) demonstrate that the nonlocal granular fluidity model captures this dependence. Next, the velocity and density profiles are compared. Using DEM simulations, GDR MiDi (2004); Baran et al. (2006) report that, for a thick layer, the shape of the velocity profile takes a form of the

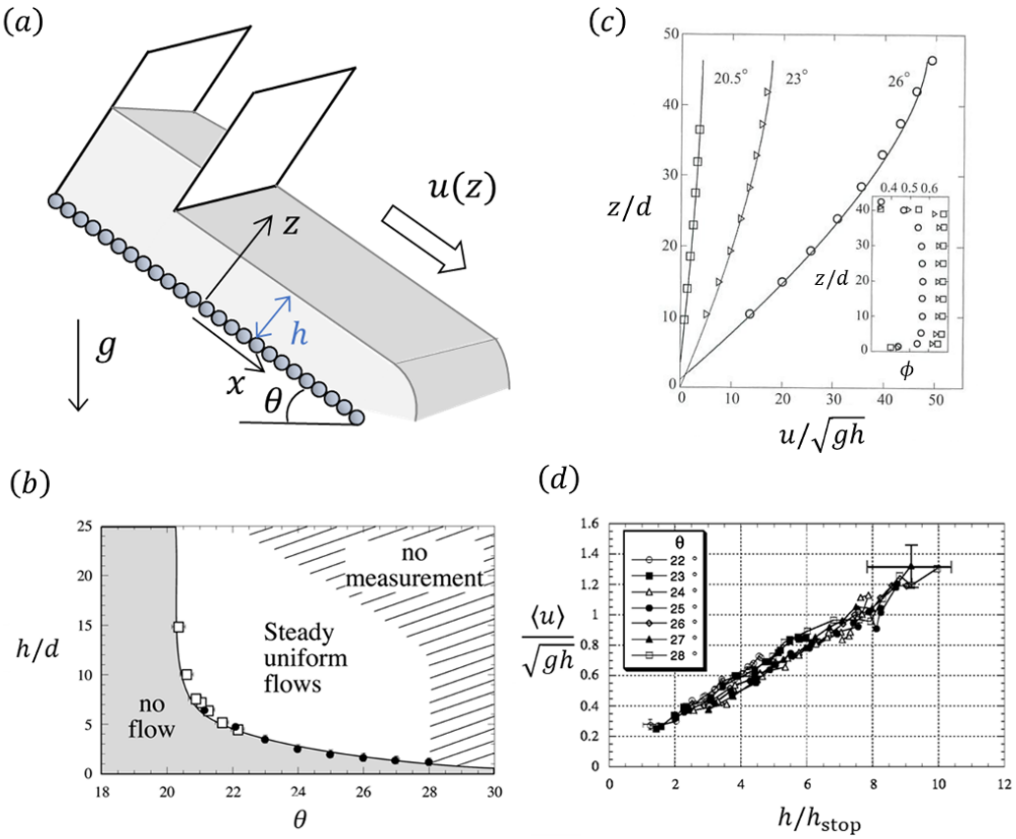

Figure 1.6: Flow down an inclined plane. (a) Image of the experimental system. (b) Region where steady uniform flows are observed in parameter space between h/d and θ. (c) Velocity profile. Simulation data (symbols) are compared with the Bagnold profile (line). The inset shows the profile of the packing fraction. (d) Relation between normalised depth-averaged velocity $\langle u \rangle / \sqrt{gh}$ and normalised thickness h/h_{stop} for various inclined angle θ. The data in panels (b) and (d) are experimentally measured (cited from Pouliquen (1999)), while the data in panel (c) are obtained by numerical simulations based on the discrete element method (cited from Baran et al. (2006); Andreotti et al. (2013)).

Bagnold profile (figure 1.6(c)). The exception is that when h approaches the minimum thickness for steady and uniform flows, the velocity profile becomes more linear (Silbert et al., 2003), which cannot be explained by the $\mu(I)$ rheology. As for the density profile, as expected, the packing fraction remains almost constant across the layer except near the bottom and free surface (inset of figure 1.6(c)). The last comparison is concerned with the depth-averaged velocity. According to experiments by Pouliquen (1999) and simulations by Silbert et al. (2003), as shown in figure 1.6(d), the relationship between $\langle u \rangle$ and

h follows

$$\frac{\langle u \rangle}{\sqrt{gh}} = \beta \frac{h}{h_{\mathrm{stop}}(\theta)}, \tag{1.39}$$

where $\beta = 0.136$ and $h_{\mathrm{stop}}(\theta)$ is the minimum thickness necessary to observe steady uniform flows with inclination angle θ. The power relation $\langle u \rangle \propto h^{3/2}$ in equation (1.39) is also consistently reproduced by equation (1.38).

1.2.5 Flow on a granular pile

As the second application of the local rheology, a flow on a granular pile shown in figure 1.7(a) is considered. This system is also a frequently-used configuration to observe steady granular flows. This type of granular flow is usually called a heap flow. To observe a heap flow, granular materials are constantly injected into two parallel walls with a gap of width W. A granular heap is then created, over which steady flows are observed. The flowing region, which is often called shear band, is localised around the surface and distinguished from the static region. The primary difference compared to a flow down an inclined plane (section 1.2.4) is that the control parameter in this heap-flow configuration is only the flux q, which is defined by the volume of flowing granular media per unit time and width . The inclination θ and the thickness of the shear band (i.e., the flowing region) h_s are spontaneously determined by the system itself. In most of the experimental observations, the typical fluidised layer consists of 10^0–10^1 grain diameters. The local rheology can give constrains on how h_s is related to θ, considering an effect of sidewalls (Jop et al., 2005).

Let us consider a granular slice of length dx sandwiched between two smooth sidewalls with a constant coefficient of friction μ_w (figure 1.7(b)). Here, for simplicity, the variation of the flow in the y direction is neglected, and the packing fraction ϕ is considered constant in granular media. The force balance along the x direction on this granular slice at depth z can be written as

$$0 = dxW\rho_\phi gz \sin\theta - dxW\mu(I(z))\rho_\phi gz\cos\theta - 2dx\int_0^z \mu_w \rho_\phi g z' \cos\theta dz', \tag{1.40}$$

where the first term is the gravity force; the second term is the friction force developing

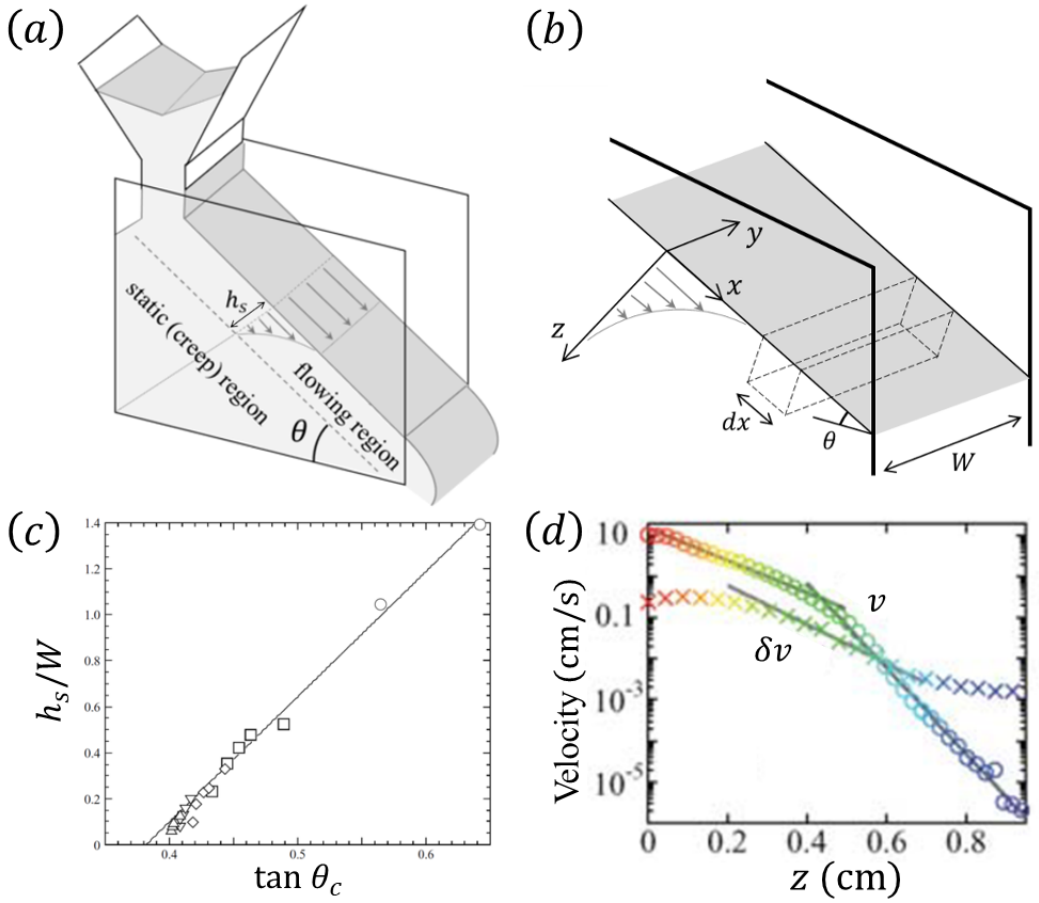

Figure 1.7: Flow on a granular pile. (a) Image of the experimental system. (b) Force balance on a granular slice. (c) Scaled thickness of the shear band h_s/W as a function of $\tan\theta$ for different widths $W = 19d$ (◯), $57d$ (□), $142d$ (◇), $283d$ (▽), $570d$ (△). Cited from Jop et al. (2005). (d) Flow velocity in the flow direction v and its fluctuation δv as a function of depth z. The velocity profile is fitted by two exponential curves with different exponents. Cited from Katsuragi et al. (2010).

on the bottom face of the granular slice; and the third term is the lateral friction force applied by both sidewalls. Note that the hydrostatic pressure is assumed. Equation (1.40) can be rewritten as

$$\tan\theta - \mu_w \frac{z}{W} = \mu(I(z)). \tag{1.41}$$

When z increases, i.e., going deeper, the friction term due to the sidewalls increases, which leads to the decrease of $\mu(I)$. However, $\mu(I)$ cannot be less than the critical value $\mu_{\min}$, which is reached when I approaches 0 (equation (1.5)). This means the existence of a critical depth below which materials cannot flow due to the resistance of the lateral

friction. This depth corresponds to the thickness of the shear band h_s, which is given by

$$\frac{h_s}{W} = \left(\frac{\tan\theta - \mu_{\min}}{\mu_w} \right). \tag{1.42}$$

As can be seen in figure 1.7(c), the fact that h_s is scaled by W has been experimentally observed by Taberlet et al. (2003); Jop et al. (2005). This scaling suggests that sidewalls considerably influence the flow property and cannot be neglected even if the width W is very large. The situation modelled by equation (1.42) can also be simply interpreted that a solid block with thickness h_s, confined between two lateral frictional sidewalls, is sliding on a rough inclined surface. Overall, the bulk dynamics of heap flows can be captured by this sliding-block approximation, which does not require the detailed information of the grains inside the flow. In granular physics, this simplified but very useful approach is often employed as a first step to model the bulk characteristics of granular flow.

Next, we go into the detailed kinematic property, especially the internal velocity profile. Actually, the unified understanding of the velocity profile has not yet been achieved. For instance, GDR MiDi (2004) showed a linearly decaying velocity profile around the surface followed by an exponential tail, whereas Lemieux and Durian (2000); Katsuragi et al. (2010) reported that the velocity is exponentially decreasing from the surface. An example of an exponential velocity profile is shown in figure 1.7(d). One can, of course, derive a more complex velocity profile by integrating the force balance (1.41) with the local friction law (1.5). Jop et al. (2005) have presented the analytical expressions of the velocity profile $v(z)$, the inclination θ, and the surface velocity v_0 as a function of the flux q for a given width W, where θ and v_0 increase as q increases or W becomes smaller. Jop et al. (2006) have also successfully modelled three-dimensional flows using the tensorial generalisation of the $\mu(I)$ rheology under an incompressible assumption as seen in section 1.2.2.

It should also be noted that some characteristics cannot be captured by the above modelling. Firstly, a critical value of the flux q exists, below which not continuous but intermittent flows are observed (Lemieux and Durian, 2000). Secondly, Komatsu et al. (2001) report that there is a creep (very slowly moving) layer exhibiting an exponentially-decaying velocity profile below a clearly fluidised region. These flow threshold and creep

motion cannot be predicted by the local rheology.

So far, the constitutive relations widely accepted for dense granular flow have been introduced, and then its universality and applicability have been validated by considering two types of granular flow in steady states. As a whole, the local rheology is able to explain major properties of dense granular flows independent of the geometry.

1.3 Vibration-induced granular flow

From this subsection, we move on to granular flows driven by vibration that this thesis puts the main focus on. When vibration is applied to a granular system, the $\mu(I)$ rheology, which successfully explains gravity-driven flows (sections 1.2.4 and 1.2.5), is no longer valid. Let us take the dimensional analysis for example. In defining dimensionless parameters under a vibrating system, parameters associated with vibration, such as amplitude A and frequency f, need to be additionally taken into consideration. The inertial number I (1.2) should therefore not be the unique parameter to govern the dynamics of granular flows. In fact, a flow down an inclined plane subjected to strong vibration does not take a form of the Bagnold profile (Gaudel and Kiesgen de Richter, 2019). Unfortunately, commonly accepted constitutive relations for vibration-driven granular flows have not yet been proposed for now. However, several important attempts have been made, which are explained below.

Firstly, in section 1.3.1 vibration strength in a granular system is characterised using dimensionless parameters. Two case studies of granular flows under vibration are then introduced in sections 1.3.2 and 1.3.3. The modelling employed in section 1.3.2 gives a good example to show that the sliding-block approximation can be a powerful tool for vibration-driven flows as well as gravity-driven flows in section 1.2.5. The all-layers-fluidisation assumption, which is also an important idea in this thesis, is additionally introduced there. Moreover, to understand how kinematic properties of granular flows are changed due to vibration, it is helpful to compare section 1.3.3 with section 1.2.5 as almost the same geometrical setup is employed. Finally, in section 1.3.4 we show how those results can contribute to the understanding of geophysical phenomena associated with natural granular flows.

1.3.1 Dimensionless vibration parameters

When sinusoidal vibration ($A \sin 2\pi f t$) is added into a granular system, usually vibration strength is quantitatively characterised by either of the following two dimensionless parameters naturally involving both the amplitude A and frequency f. One is the dimen-

sionless acceleration Γ (Evesque and Rajchenbach, 1989) defined by

$$\Gamma = \frac{A(2\pi f)^2}{g}, \tag{1.43}$$

where g is the gravitational acceleration. The other is the dimensionless squared velocity S_Γ (Pak and Behringer, 1993), also called the shaking strength or shaking parameter, which is defined by

$$S_\Gamma = \Gamma \frac{A}{d} = \frac{A^2(2\pi f)^2}{gd}, \tag{1.44}$$

where d is the grain diameter.

Γ is purely relevant to the competition between body forces due to gravity and vibration. When vibrating the system vertically with $\Gamma > 1$, grains experience free-fall duration in every vibration cycle. In this regime, the stability of granular media established by the gravity cannot be sustained, and movement of grains are easily induced by the inertial force due to vibration. Accordingly, the occurrence condition of phenomena peculiar to a vibrating granular system is often characterised by $\Gamma > 1$, an example of which will be seen later. On the other hand, S_Γ can be considered to be a modified version of Γ, involving the grain diameter as a relevant length scale. In other words, a state of granularity is taken into consideration. Physically, S_Γ represents the ratio of kinetic energy to gravitational potential energy per grain mass. For highly vibrated systems ($\Gamma \gg 1$), S_Γ is also directly related to granular temperature, i.e., velocity fluctuation. Therefore, in such a gas-like regime, S_Γ is especially relevant to characterise the state of a granular bed (Eshuis et al., 2010; Katsuragi, 2016). Note that, however, these dimensionless parameters are used just for characterisation of bulk granular behaviour under vibration. From a more microscopic point of view, as in section 1.2.1, the rheological property of local granular deformation might depend on the shear rate, pressure, density, packing fraction, etc. For now, the constitutive laws for dense granular flow in the presence of vibration have not yet been established.

To show an example of characterisation by Γ and S_Γ, the convective motion of a granular bed is considered. When a granular column is vertically shaken, particles convect as shown in figure 1.8. This granular convection can be observed when Γ exceeds

~ 1 (Taguchi, 1992; Garcimartín et al., 2002). The convective velocity exhibits an exponential decay with depth (Ehrichs et al., 1995; Knight et al., 1996). The magnitude of its characteristic velocity shows complex dependence on various control parameters, such as the vibration condition, grain size, height of a granular bed, and diameter of a container. Yamada and Katsuragi (2014) have conducted systematic experiments by varying these parameters, and proposed the unified scaling law for the maximum convective velocity obtained around the surface layer by means of a dimensional analysis. It states that S_Γ is more relevant than Γ to scale the convective velocity. Put it simply, Γ is the most relevant parameter for the occurrence condition of granular convection, whereas the velocity of convective motion is determined by S_Γ.

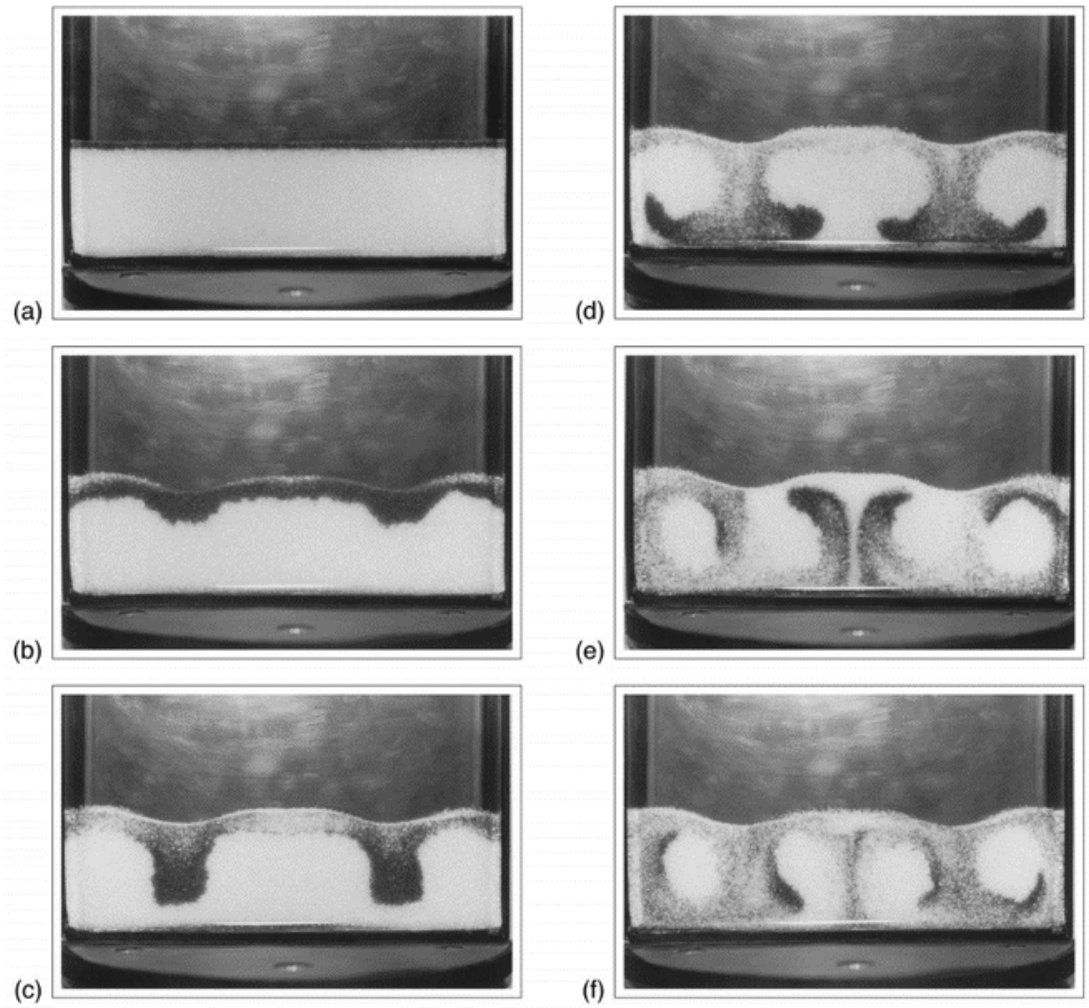

Figure 1.8: Granular convection in a quasi-two-dimensional box. Glass beads with diameter $d = 0.61$ mm are used, and the vibrational condition is $\Gamma = 6.4$ ($f = 500$ Hz). Panels (a)–(f) are pictures taken at $0, 5, 8, 14, 23, 32$ s after applying vibration. Cited from Aoki et al. (1996).

1.3.2 Spreading of a granular heap under horizontal vibration

The spreading dynamics of a granular heap on a horizontally vibrated plate has been experimentally investigated by Sánchez et al. (2007). The setup of the experiment is shown in figure 1.9(a). As an initial condition, a granular heap is created on a sand-cast rough aluminium plate, which is horizontally shaken with the frequency ranging between 15 and 30 Hz and the maximum amplitude 1 mm. After turning on the vibration generator, the granular heap is destabilised and spread with the slope getting smoother as time goes on (figure 1.9(b)). The vibration condition is set to satisfy $\Gamma > \mu_s$, in which the relative slide between the plate and heap is in principle possible. To understand this relaxation dynamics, Sánchez et al. (2007) have proposed the granular transport law as follows.

First of all, Sánchez et al. (2007) assume that all layers of the heap is uniformly fluidised (i.e., all-layers-fluidisation assumption), and then suppose an infinitesimal granular slice of width dx, length L_y, height $h(x,t)$, and slope $|\nabla h|(= |\partial h/\partial x|)$ to be a sliding block (i.e., sliding-block approximation). The image of the modelling is illustrated in figure 1.9(c). Assuming the hydrostatic pressure, the pressure gradient along the x axis can be written as $dP/dx = \rho_\phi g|\nabla h|$. The force applied to the slice due to the pressure gradient F_p is then given by

$$\begin{aligned} F_p &= \int_0^{L_y} \left(\int_0^h \frac{dP}{dx} dx dz \right) dy \\ &= \rho_\phi g h L_y dx |\nabla h| \\ &= mg|\nabla h|, \end{aligned} \tag{1.45}$$

where $m = \rho_\phi h L_y dx$ is the mass of the slice. On the other hand, the frictional force between the slice and the oscillating plate F_f is

$$F_f = \mu mg, \tag{1.46}$$

where μ is the friction coefficient.

Next, using equation (1.45) and (1.46), the equation of motion with respect to the slice

is expressed as

$$\dot{v} = A(2\pi f)^2 \sin 2\pi f t + \frac{1}{m}\left\{F_p - F_f \,\mathrm{sgn}\,(v)\right\}, \tag{1.47}$$

where v is the velocity difference between the slice and plate, and $\dot{T}$ denotes the time derivative of any physical quantity T. Employing A and $(2\pi f)^{-1}$ as a characteristic length and time, the equation of motion (1.47) is nondimensionalised as follows:

$$\Gamma\,\hat{\dot{v}} = \Gamma \sin \hat{t} + |\nabla h| - \mu \mathrm{sgn}\,(\hat{v}), \tag{1.48}$$

where $\hat{t} = 2\pi f t$ and $\hat{v} = v/A(2\pi f)$. This equation suggests that the velocity obtained for a fixed $|\nabla h|$ sinusoidally and periodically fluctuates as shown in figure 1.9(d). However, the average sliding velocity $\langle \hat{v} \rangle$ is enough to reproduce the overall relaxation process of a vibrated granular heap. By solving equation (1.48) analytically, $\langle \hat{v} \rangle$ is written as

$$\langle \hat{v} \rangle = \frac{\alpha\,(\Gamma/\mu)}{\mu} |\nabla h|, \tag{1.49}$$

where $\alpha\,(\Gamma/\mu)$ is a certain increasing function of Γ/μ, which is plotted in figure 1.9(e). See Sánchez et al. (2007) for the specific expression of the function $\alpha\,(\Gamma/\mu)$.

Since the sliding-block approximation is now employed, the volume flux can be given by $A(2\pi f)\langle \hat{v} \rangle h$, and consequently the continuity equation can be written as

$$\frac{\partial h}{\partial t} = \frac{\partial}{\partial x}\left(U \frac{\partial h^2}{\partial x}\right) \qquad \text{with} \qquad U = \frac{A(2\pi f)\,\alpha\,(\Gamma/\mu)}{2\mu}. \tag{1.50}$$

Sánchez et al. (2007) show that this continuity equation takes an exact parabolic self-similar solution:

$$\frac{h(x,t)}{H(x,t)} = 1 - \left(\frac{2x}{W(t)}\right)^2, \tag{1.51}$$

where $W(t)$ and $H(t)$ are the maximum width and height of the spreading heap. Experimental results are shown in figure 1.10(a), where the profiles are self-similar predicted by the solution (1.51).

Recently, Khefif et al. (2018) have performed DEM simulations to reproduce this experiment, and then revealed how the frictional property on the basal layer is changed by

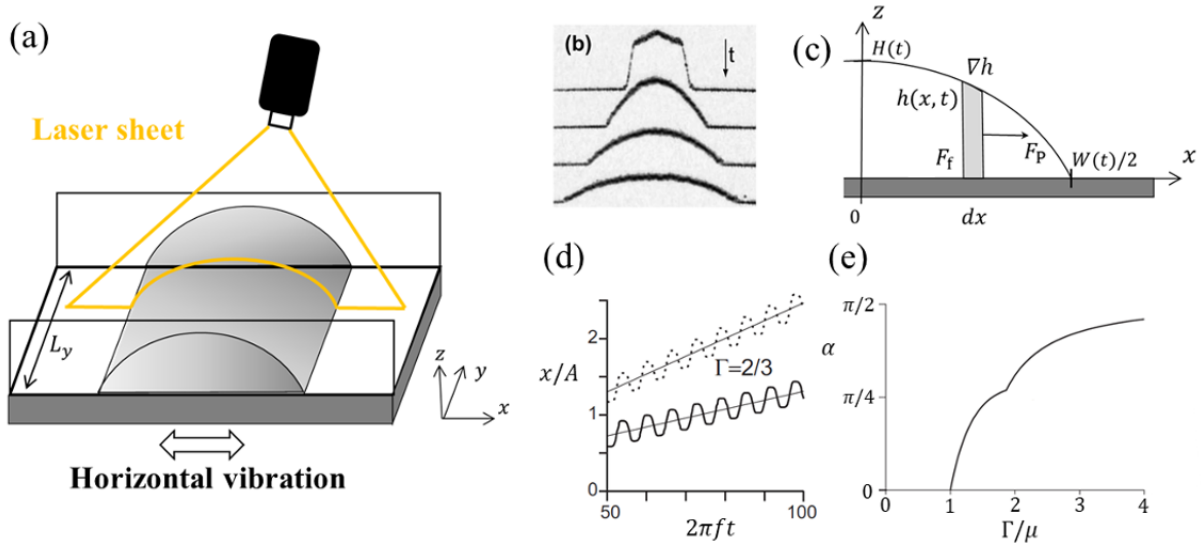

Figure 1.9: (a) Image of the experimental system. (b) Profiles obtained by a laser at different times. (c) Image of the modelling using the sliding-block approximation under the all-layers-fluidisation assumption. (d) Curves show the solution of the equation of motion (1.48) in a x–t space. The fixed conditions are $\mu = 0.5$ and $\Gamma = 2/3$. The slope is varied: $|\nabla h| = 0.01$ (solid curve) and $|\nabla h| = 0.02$ (dashed curve). The thin lines show the average sliding velocity predicted by equation (1.49). (e) Plot of the function $\alpha\,(\Gamma/\mu)$ in equation (1.49). The analytical expression is given in Sánchez et al. (2007). Panels (b), (d), and (e) are cited from Sánchez et al. (2007).

vibration. They measured the effective friction coefficient μ_{eff} defined by the ratio of the shear stress τ to the pressure P on a substrate for various vibration and basal conditions. The bumpiness is characterised by the average diameter of the basal spheres $d_s = \lambda d$, where the bumpiness value λ is varied between 0 (smooth subtract) and 1. From the analogy to the $\mu(I)$ rheology, μ_{eff} is scaled by a similar dimensionless parameter to the inertial number (1.2). Recall that the inertial number is defined by the ratio of the timescale of a microscopic grain rearrangement t_{micro} to the timescale of a macroscopic flow t_{macro}. In this vibrating system, t_{macro} can be related to the characteristic vibration velocity, i.e., $t_{\text{macro}} = d/A(2\pi f)$, while t_{micro} can be associated with the duration of free fall under gravity, i.e., $t_{\text{micro}} = d/\sqrt{gd}$, where d is grain diameter. Therefore, the inertial number in a vibrating system I_v is given by

$$I_v = \frac{t_{\text{micro}}}{t_{\text{macro}}} = \frac{A(2\pi f)}{\sqrt{gd}}, \tag{1.52}$$

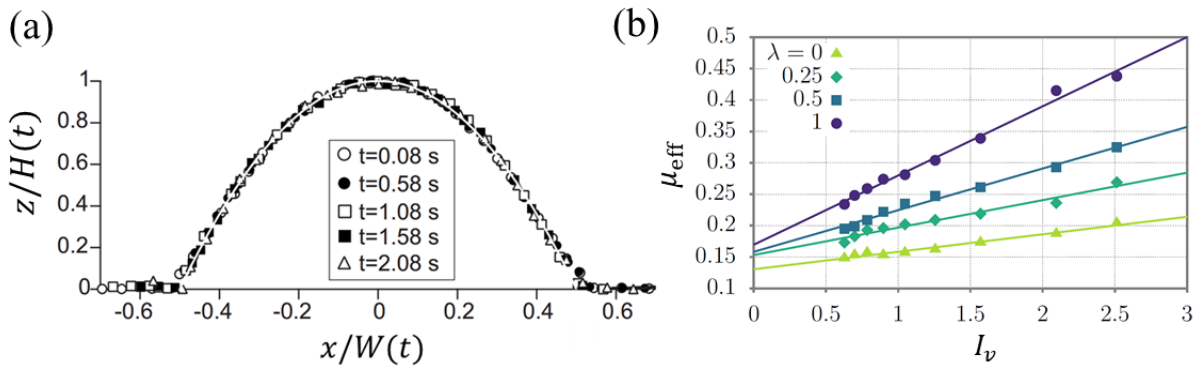

Figure 1.10: (a) Time evolution of the spreading granular droplet, showing self-similar profiles (1.51). Cited from Sánchez et al. (2007). (b) Effective friction coefficient μ_{eff} as a function of the inertial number in a vibrating system I_v for different basal bumpiness λ. The lines show the best fit by equation (1.53). Cited from Khefif et al. (2018).

which corresponds to the square root of the shaking parameter S_Γ (1.44). Figure 1.10(b) compares μ_{eff} with I_v. Since μ_{eff} is not locally measured but based on the contact between a substrate and bottom particles, it depends on the basal bumpiness as well as vibration conditions. For all basal conditions, however, μ_{eff} can be scaled by a simple linear function of I_v:

$$\mu_{\mathrm{eff}}(I_v) = \mu_0 + bI_v, \tag{1.53}$$

where μ_0 and b are the fitting parameters: μ_0 is almost constant whilst b increases with λ. This functional form is identical to the friction law (1.7) proposed by da Cruz et al. (2005). The positive correlation between μ_0 and I_v is also consistent with the $\mu(I)$ rheology in the dense flow regime. Although the rheology in a vibrating system has been gradually revealed, the model that can access even more microscopic quantity such as the local pressure or shear rate has not yet been established. There is still a long way to fully achieve the continuum description of granular flows under vibration.

1.3.3 Heap flow under acoustic noise

Next, we focus on a vibration-driven flow in a steady state. Roering et al. (2001) have observed steady heap flows using the system illustrated in figure 1.11(a), which is very similar to figure 1.7(a). They created a pile using sands of diameter 0.7 mm, enclosed in a box (1200 mm long, 600 mm high, and 100 mm wide) with open ends at both sides.

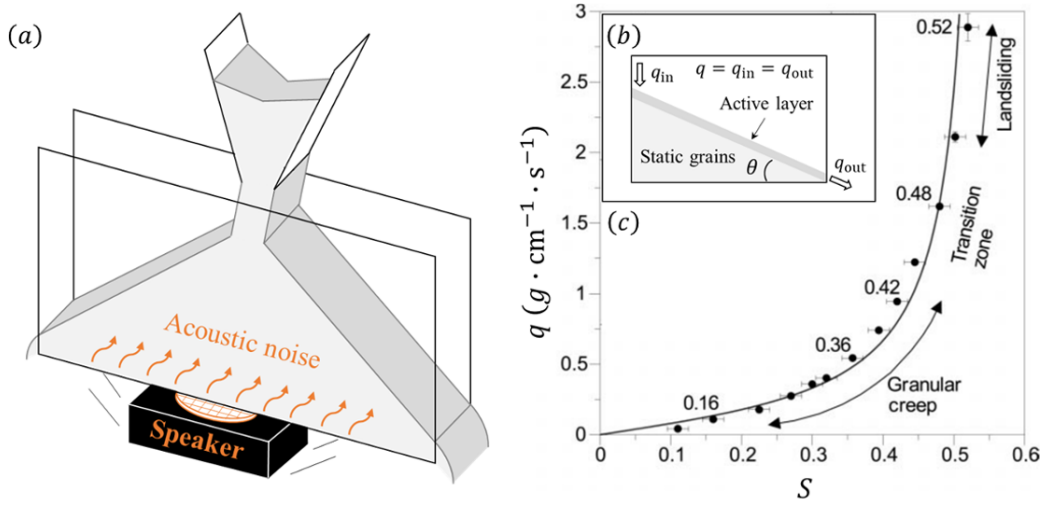

Figure 1.11: Heap flow under acoustic noise. (a) Image of the experimental system. (b) Image of the observed heap flow. The actively flowing layer is separated from the static layer. (c) Experimental result: flux q versus global slope S. The solid block curve represents the best fit by the Roering1999 model (1.54). The fitting parameters are $K_d = 0.77 \pm 0.05$ g cm^{-1} s^{-1} and $S_c = 0.56 \pm 0.02$. Cited from Roering et al. (2001).

The only difference between figures 1.7(a) and 1.11(a) is that a large speaker is coupled to the bottom of the container to agitate the granular assembly by acoustic noise. In general, acoustic noise can play a role of mechanical vibration, and unlock force chains among grains, which induces a granular flow (Doane et al., 2019). The speaker works to propagate acoustic waves with constant intensity along the box walls and through the granular bed.

In this setup, the control parameter is only the flux q as well as the gravity-driven heap flow in section 1.2.5. While applying acoustic vibration, the granular flow spontaneously achieves the steady state, where the influx q_{in} equals the outflux q_{out} (figure 1.11(b)). In the steady state, the static region exists underneath the flowing region, which means that the shear band can be observed. The resultant slope of the surface flow S depends on the flux q and the vibration intensity. This slope S is manually measured by an inclinometer, using the interior part (middle 80% of the pile), in which the slope and fluidised thickness are relatively constant (Roering, personal communication, 2019). Therefore, S can also be regarded as the global (not locally measured) slope of the entire flow. The relation between the flux q and the global slope S is shown in figure 1.11(c). In contrast to a

conventional heap flow in the absence of vibration, the flow subjected to vibration reaches the steady state even if the slope is much less than the angle of repose. Figure 1.11(c) shows that the flux q increases almost linearly with S at small gradients, while strong nonlinearity appears at large gradients.

To explain the relation between q and S, Roering et al. (1999) have proposed the phenomenological model:

$$q = \frac{K_d S}{1 - (S/S_c)^2}, \tag{1.54}$$

where K_d represents the transport coefficient, and S_c means the critical slope where the flux q diverges. Note that S_c does not necessarily correspond to the angle of repose $\tan\theta_c$. The derivation of this model is based on three fundamental assumptions below:

(i) The vibration energy inputted by the speaker and the dissipative energy due to friction and gravity always balance each other out to maintain a steady flow.

(ii) A flowing granular assembly is regarded as a solid block with constant thickness that slides on a rough inclined surface (i.e., sliding-block approximation).

(iii) The vibration energy is distributed so that the block can isotropically move in all directions with the equal probability (i.e., energy-equipartition model).

In this thesis, we refer to equation (1.54) as the Roering1999 model after the first author of the original paper and its published year (Roering et al., 1999). The solid curve in figure 1.11(c) shows the fitting by the Roering1999 model, where both K_d and S_c are left as the fitting parameters. The experimental data is well reproduced by the Roering1999 model.

It should finally be worth noting that, in addition to the Roering1999 model, others have proposed different models to explain the same nonlinear behaviour. For instance, Roering (2004) has proposed a stochastic model by considering the probability that a particle is excited enough to move beyond an adjacent one with the analogy to the rate process theory used for chemical reactions. On the other hand, Furbish et al. (2008) discuss the balance between the production and disruption rates of granular force chains to derive the transport model. Although these models can predict the flow properties in

more detail, the functional form of the Roering1999 model and the physical meaning of its fitting parameters are the clearest and simplest among the proposed model. In fact, taking the advantage of that simplicity, the Roering1999 model has been applied to many geophysical phenomena so far as introduced below.

1.3.4 Application to crater relaxation dynamics

As mentioned in the beginning, the evolution of most topographical structures on the Earth involves flows of particulate materials on the ground. Such natural granular flows also influence the terrain development even on an extraterrestrial astronomical body covered with regolith. Miyamoto et al. (2007) report that the observation of asteroid Itokawa by spacecraft Hayabusa captured the evidence of gravel migration (figure 1.12). These natural granular flows can lead to the modification of characteristic terrains over the years. In fact, on regolith-covered small bodies such as asteroid Itokawa and Eros, the number of small craters is deficient compared to the model predictions based on the crater production rate by impacts (Richardson et al., 2004; Michel et al., 2009). They predict that natural granular flows are triggered mainly by meteorite-impact-induced seismic events. Illustrated in figure 1.13 is the overview of this crater relaxation process due to natural granular flows induced by seismic vibration. In order to quantitatively evaluate the timescale of the relaxation, it is necessary to estimate how the flux of the regolith movement is determined by ground conditions and the magnitude of seismic vibration. Using the Roering1999 model (1.54), Richardson et al. (2004); Richardson Jr. et al. (2005) have proposed the fundamental theoretical framework for crater relaxation on a small asteroid.

When a meteorite strikes on the surface of a small asteroid, its body is entirely shaken even if the impactor size is centimetre scale (Yamada, 2016). If the maximum acceleration of seismic vibration exceeds the magnitude of the asteroid's gravity everywhere on its surface (i.e., $\Gamma > 1$), all regolith grains experience free fall and consequently get destabilised. Such an event is called global seismic shaking. Richardson et al. (2004) have created artificial seismic signals induced by meteorite impacts (figure 1.14(a)). The impactor size necessary to achieve the global seismic shaking on asteroid Eros is estimated as ~ 2 m in diameter. These synthetic seismograms are then applied to a numerical model

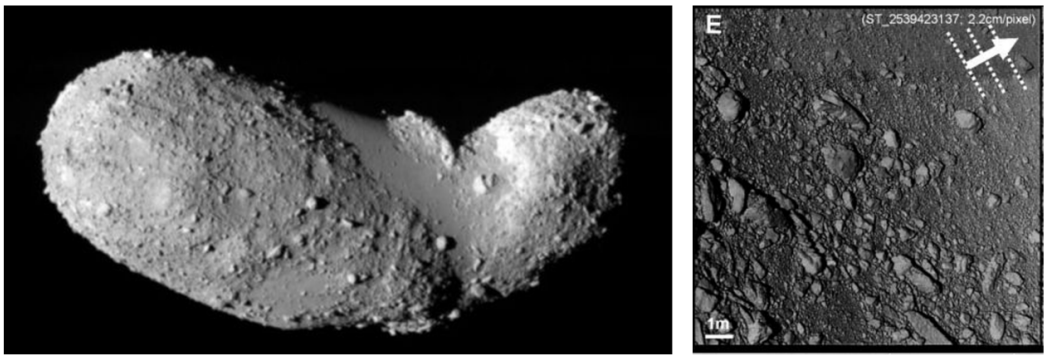

Figure 1.12: (left) Overview of asteroid Itokawa (JAXA/ISAS). (right) Evidence of regolith migration on asteroid Itokawa. White dotted lines correspond to alignments of boulders, which suggest that gravels flow in the direction perpendicular to them (arrow). Cited from Miyamoto et al. (2007).

of regolith resisting on a variety of slopes under Eros gravity conditions. These simulations were performed using the Newmark slide-block method (Newmark, 1965), which is often utilised to evaluate the landslide hazard when an earthquake occurs (e.g., Miles and Ho, 1999). This method can predict the motion of a destabilised rigid block subjected to seismic vibration by numerically solving equations of motion. Figure 1.14(b) shows the resulting downslope flux per impact q_{i} as a function of slope S. Note that q_{i} does not mean a conventional volumetric flux, but the one scaled by the height, which corresponds to the migration length along the downslope per impact (see Richardson Jr. et al. (2005) for the detailed definition). Here, the non-linear trend is consistent with the Roering1999 model (1.54). Richardson et al. (2004) have estimated the transport coefficient K_d for various impactor sizes D_p from the data of figure 1.14(b), which enables us to predict the typical erasure rate of craters due to impact-induced seismic waves. As mentioned before, the flux increases almost linearly with respect to the slope (i.e., $q_{\mathrm{i}} \propto S$) when the slope is small. Therefore, for the sake of simplicity, the crater modification process due to vibration is usually described by a diffusion equation. The observed Eros's surface morphology can be consistently explained by combining these modellings with the statistics of the impact cratering record.

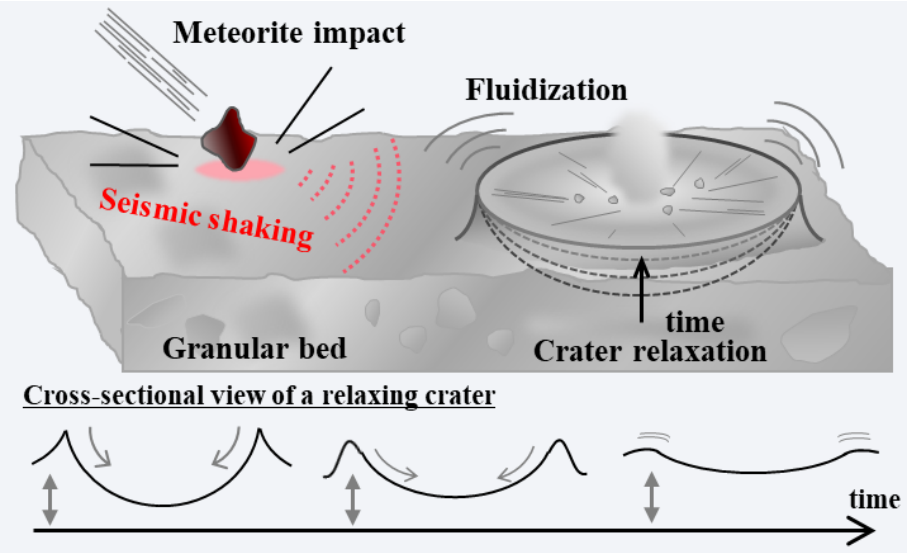

Figure 1.13: A schematic illustration of crater relaxation caused by meteorite-impact-induced seismic shaking on a small astronomical object. Cited from Tsuji et al. (2018).

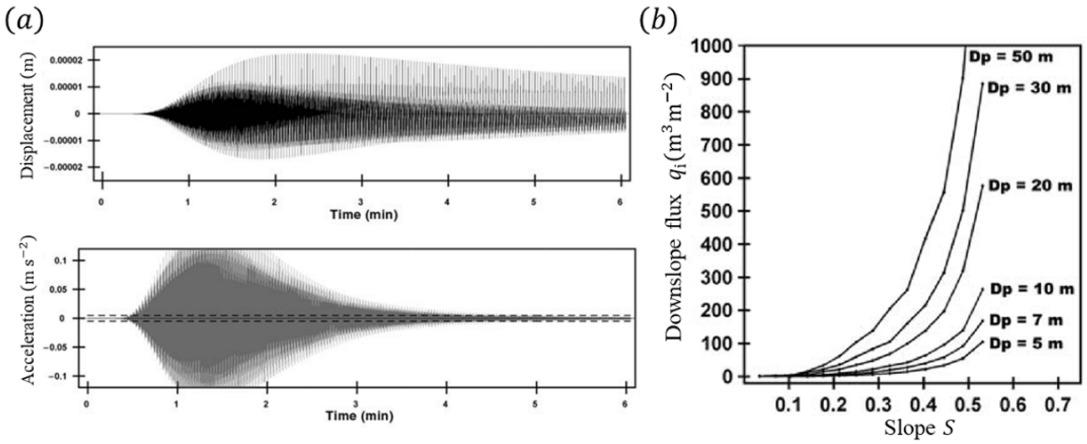

Figure 1.14: (a) Artificial seismic signals produced by the hydrocode. The upper and lower panels show the amplitude data and the acceleration data induced by a 10-m stony impactor, respectively. The dashed line depicts the gravitational acceleration on Eros's surface. (b) Downslope flux of the regolith layer for a variety of slope. Data are obtained by the Newmark slide-block method. Cited from Richardson et al. (2004).

1.4 Aim and objective

This study aims to build the dynamics model for granular flow driven by vertical vibration. We particularly investigate flows in unsteady (i.e., transient) states and then reveal the morphological evolution of a granular heap subjected to vertical vibration. Since the property of granular flows in nature changes time-dependently, putting focus on unsteady states, which has been relatively little studied so far, is also important from the aspect of application to geophysical phenomena. As introduced in section 1.3.2, Sánchez et al. (2007) have successfully modelled the relaxation dynamics of a horizontally-vibrated granular layer by building equations of motion. In contrast, when the flow is driven by vertical vibration, we cannot give the straightforward theoretical description as in the case of horizontal vibration because it is not clear how the inertial force is transmitted to a granular layer. Regarding this problem, the Roering1999 model is perhaps applicable because this can explain the flow dynamics of grains agitated against gravity (section 1.3.3). It is, however, not clear whether it can be directly used for unsteady flows under mechanical vertical vibration. Moreover, the dependence on experimental parameters (e.g., vibration strength and grain properties) and the internal velocity profile have not yet been revealed.

To comprehensively cover such open questions, we conduct the systematic study as follows. Firstly, using experimental approaches, we attempt to confirm if the Roering1999 model gives reasonable predictions for the unsteady relaxation of a vertically-vibrated granular heap. To this end, section 2 introduces the experimental setup and instruments, and then in section 3 the experimental data are analysed. Next, to further improve the understanding, we also perform particle-scale numerical simulations. The specifics of the simulation model are written in section 4, and then section 5 shows the analysis result to obtain the detailed flow property that cannot be investigated by experiment. Based on both experimental and numerical results, the characteristics of granular flow dynamics under vertical vibration are discussed from multiple points of view in section 6. Finally, the summary of this thesis is given in section 7.

2 Experimental setup

2.1 Experimental outline and data acquisition

To measure unsteady granular flows under vertical vibration, the configuration as shown in figures 2.1 and 2.2 is employed. The experiment is conducted following the procedure below: First of all, a disk with radius $R = 40$ mm is mounted onto the electromechanical vibration generator. A conical granular heap with the angle of repose is then created on that disk. The granular materials used in the experiment are summarised in table 2.1. The surface of the disk is pasted with the same kind of grains so that a heap can maintain its shape. Next, sinusoidal vertical vibration ($A \sin 2\pi f t$) is continuously applied to the disk by turning on the vibrator. Here, the amplitude A is gradually increased during the initial short period $T_a = 0.5$ s to calmly reach the stable vibration condition without burst signals. The time when the vibration achieves a stable state is defined as $t = 0$ s. The detail of this process is explained in section 2.2.2.

The amplitude A and frequency f are varied in the range of $10^{-4} - 10^{0}$ mm and 50–500 Hz. In this experiment, the condition in which granular media are fluidised is difficult to determine uniquely. Although Γ seems to be the most relevant, the critical condition Γ_c fluctuates in the range of $1 < \Gamma_c < 2$, which depends on the vibration frequency f. In fact, King et al. (2000) report a similar tendency for surface instability of an inclined granular bed subjected to vertical vibration. In addition, in the range of $1 < \Gamma < 2$, not continuous but intermittent heap flows are observed. To avoid such complexity and focus on clearly

Table 2.1: Properties of granular materials used in the experiment. Materials 1–3 are spherical, and material 4 is a rough sand. The angle of repose θ_c is estimated by the ratio of the height to the radius.

Material	Density (10^3 kg/m^3)	Diameter (mm)	Angle of repose θ_c (deg. / tanθ_c)	Note
1. Almina ball	3.9	0.5 ± 0.1	24° / 0.45	AS-ONE Corp. AL9-0.5
2. Almina ball	3.9	1.0 ± 0.1	24° / 0.45	AS-ONE Corp. AL9-1
3. Zirconia ball	5.9	0.5 ± 0.1	25° / 0.46	AS-ONE Corp. CZC0050
4. JIS sand	2.6	1.0 ± 0.3	33° / 0.65	JIS R 5201

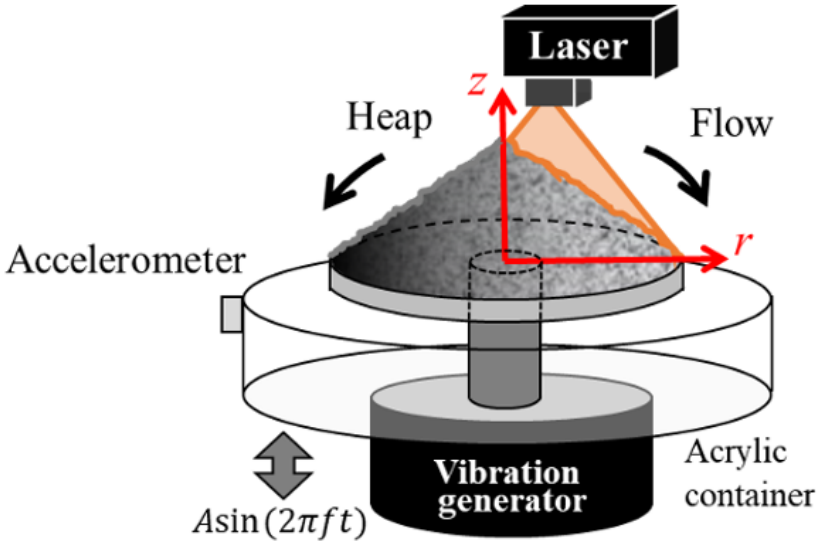

Figure 2.1: Schematic illustration of the experimental system. A heap is created on a disk mounted on a vibration generator. Grains flowing out of the disk are captured by an acrylic container. Vibration data are recorded using an accelerometer.

fluidised regimes, relatively strong vibration of $\Gamma = 2$–10 is applied in this study. Under this vibration range, the heap flow is expected to lie in the dense flow regime. When the vibration is even stronger, the granular bed can enter the Leidenfrost state or gaseous regime (e.g., Eshuis et al., 2005).

Once granular media are fluidised, grains flow to the outside of the disk, and the shape of the heap begins to relax. Outflowed grains are captured by an acrylic container surrounding the disk. The advantage of this experimental configuration is that the sidewall effect, which usually must be considered in the case of quasi-two-dimensional flows (section 1.2.5), does not appear at all.

While a heap is subjected to vibration, its surface profile is continuously recorded by the high-speed laser profiler. Figure 2.3(a) shows profiles obtained in the experimental condition of $A = 0.04$ mm and f $= 200$ Hz ($\Gamma = 6$) with material 1 in table 2.1. The measurement range is from the centre to the edge of the heap along the radial direction ($r = 0$–40 mm). The origin of the height coordinate $z = 0$ mm is calibrated to the surface of the disk. Since a heap relaxes axisymmetrically, the one-dimensional surface profile represents the whole relaxation process. The spatiotemporal visualisation of the local

height of a heap is also drawn in figure 2.3(b). The grey scale indicates the local height h for given r and t, which is measured from the surface of the disk $z = 0$. Henceforth, when experimental results are discussed in this thesis, these experimental conditions are used for subsequent plots unless otherwise noted.

In the experiment, three experimental realisations for each set of experimental conditions are performed to check the reproducibility. All instruments are controlled and synchronised using the software LabVIEW and data transfer device DAQ (National Instruments). Experimental data presented in this thesis are the same as the one used in Tsuji et al. (2018, 2019). The details of each procedure are explained in the following subsection.

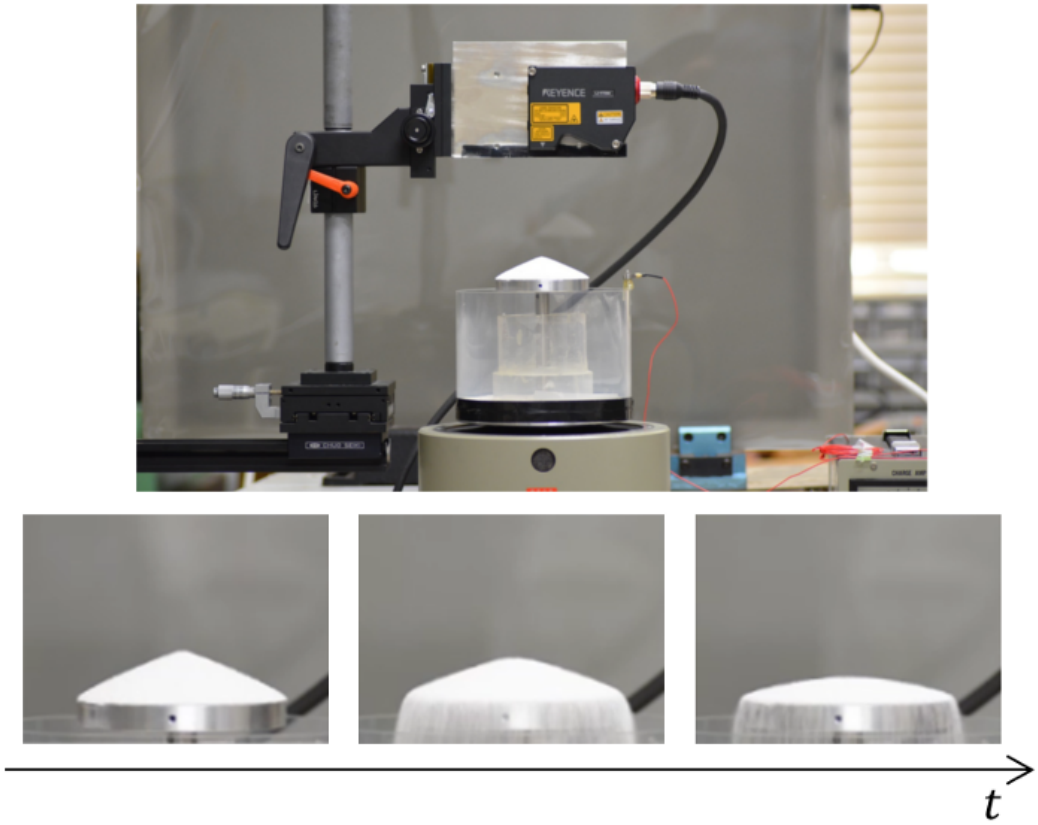

Figure 2.2: The upper panel shows a photo of the experimental system. In the lower panels, snapshots of a relaxing heap by vibration are shown. Lower images are cited from Tsuji et al. (2018).

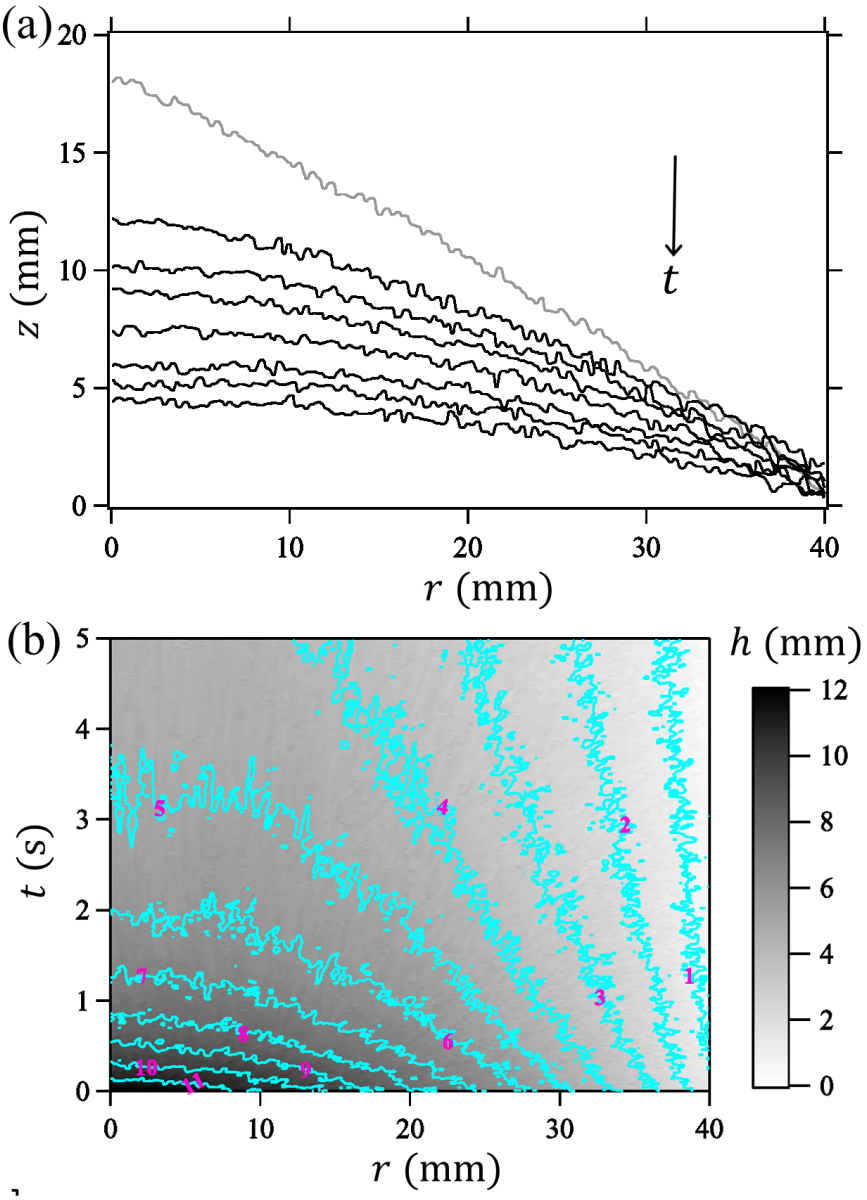

Figure 2.3: (a) Surface profiles of a relaxing heap obtained by the laser profiler. A grey curve shows the initial heap, which is measured before applying vibration, i.e., at $t = -T_a$. Black curves represent profiles obtained at $t = 0, 0.26, 0.5, 1.0, 2.0, 3.0, 5.0$ s from top to bottom. Cited from Tsuji et al. (2018). (b) Spatiotemporal visualisation of profiles. The grey scale indicates the local height of a heap h, where $h = 0$ corresponds to the bottom of the disk ($z = 0$). Light blue curves represent contours drawn at intervals of 1 mm.

2.2 Details of experimental instruments

2.2.1 Preparation of a granular heap

There are several preparation methods to create a granular heap with the angle of repose, and its shape slightly depends on the geometrical setup (Duran, 2000; Barton and Buchberger, 2003). In this study, the discharge method using a funnel is employed, which is suitable to our experimental system and allows us to reproduce almost the same initial conditions any number of times.

The discharge method that we used is illustrated in figure 2.4: (1) A funnel is attached on the disk upside down, and then grains are poured into the inside of the funnel until fulfilled by using another funnel. (2) The funnels are lifted up as carefully and slowly as possible. (3) Eventually, a granular heap with the angle of repose is spontaneously created. Note that the slope of a funnel used in the experiment is much larger than the angle of repose. Figure 2.5 shows an actual picture of a granular heap created by the above procedure.

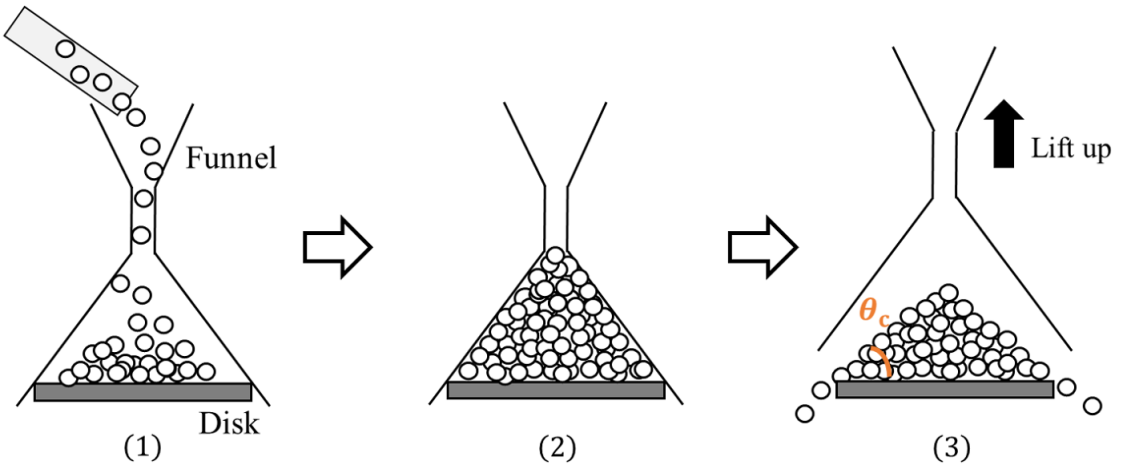

Figure 2.4: Illustration of the preparation method for a granular heap with the angle of repose.

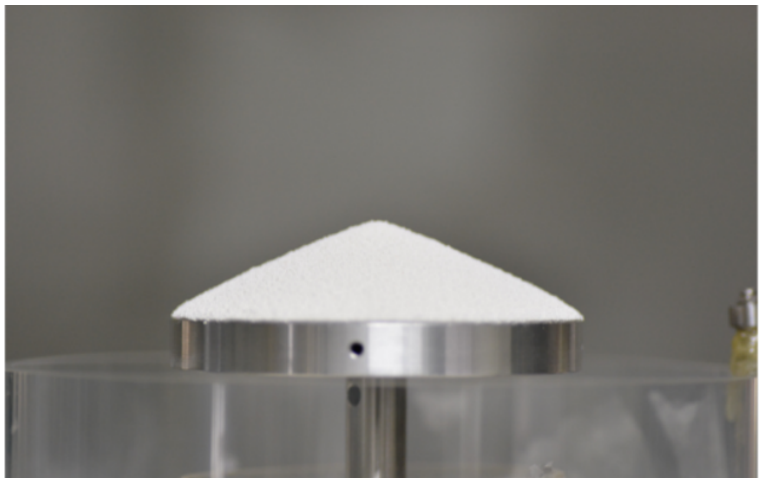

Figure 2.5: A granular heap created by the procedure in figure 2.4. Material 1 in table 2.1 is used for granular media.

2.2.2 Control of a vibrator

A granular heap is mounted on the electromechanical vibration generator (EMIC 513-B/A), which can generate continuous vertical vibration. To record vibration conditions, an accelerometer (EMIC 710-D) is attached on the top of the container. Due to the instrumental limits, the amplitude becomes unstable just after turning on the vibrator. Figures 2.6(a) and (b) show examples of acceleration data obtained by an accelerometer. The vibration generator is controlled to make vibration of $\Gamma = 6$ and $f = 200$ Hz at $t = 0$ s. As can be seen in figures 2.6(a) and (b), peaked noises are generated around $t = 0$ s. In order to avoid this problem, the vibration amplitude is gradually and linearly amplified during the short period $T_a = 0.5$ s as shown in figures. 2.6(c) and (d). This procedure enables us to erase peaked noises observed in figures 2.6(a) and (b). The time when vibration achieves the stable state is defined as $t = 0$ s, and the data after this moment are analysed. Therefore, the data around the angle of repose, which correspond to between the top grey and the second black profiles in figure 2.3, are not used for the analysis as the vibration amplitude is not constant.

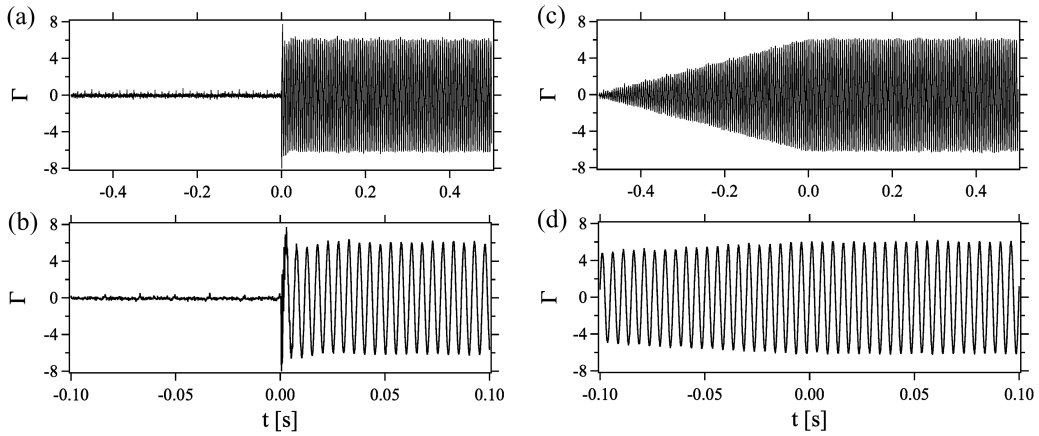

Figure 2.6: Raw acceleration data of vibration obtained by an accelerometer: (a) Data obtained when vibration is triggered at $t = 0$ s; (b) Magnified view of (a); (c) Data obtained when vibration amplitude is linearly amplified at $t = -T_a \sim 0$ s, where $T_a = 0.5$ s; (d) Magnified view of (c). $t = 0$ s corresponds to the moment when the steady vibration is achieved.

2.2.3 High-speed laser profilometry

The high-speed laser profiler (KEYENCE LJ-V7080, see figure 2.7) is employed to measure the surface profile of a relaxing heap. Horizontal measurement ranges are from the centre to the edge of the disk ($r = 0$–40 mm). The sampling rate is 50 Hz, and the horizontal spacial resolution is 50 μm/pix. The number of pixels is 800, which can just cover all profiles of $r = 0$–40 mm. The measurement error along the z axis is less than 50 μm. These high resolution and accuracy of the laser measurement enable us to precisely capture the grain-scale movement. Figure 2.8 shows the magnified view of two successive profiles. The small fluctuations of the profile (figure 2.8) reflect the typical grain size. It can be confirmed that the surface layer moves, almost keeping its profile pattern.

Figure 2.7: High-speed laser profiler (KEYENCE LJ-V7080) used to measure the profile of a relaxing granular heap.

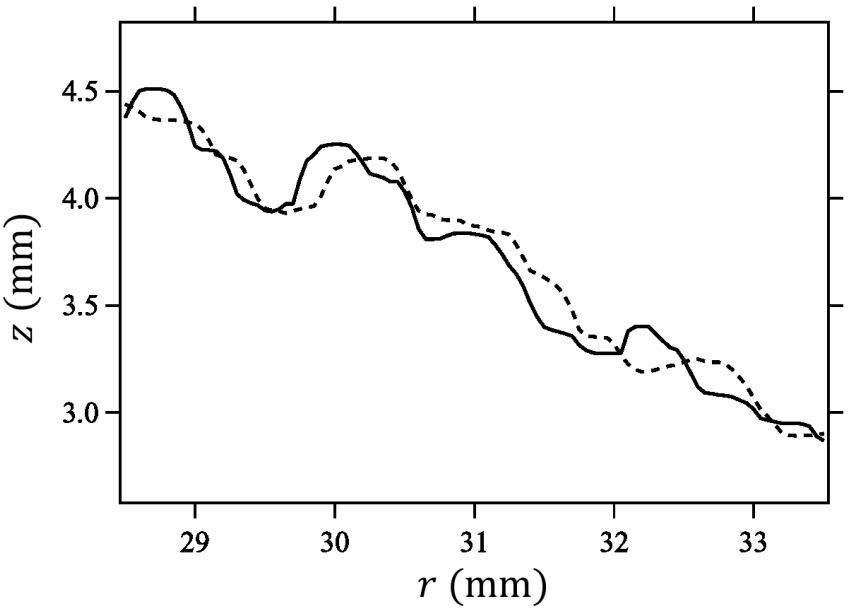

Figure 2.8: Magnified view of two successive profiles. Solid and dashed profiles correspond to $t = 0.78$ and 0.80 s. It seems that grains flow with the profile pattern almost kept. Cited from Tsuji et al. (2019).

3 Experimental result

3.1 Relationship between flux and slope

In the analysis, to confirm whether the Roering1999 model (1.54) holds, the flux and slope are measured at four different positions with the interval $\Delta r = 10$ mm ($r = 5, 15, 25, 35$ mm) at various times. Since the heap is relaxed axisymmetrically, the flux q at $r = r'$ and $t = t'$, which is defined as the volume of granular media flowing across unit length per unit time, is calculated as

$$q(r', t') = \frac{-1}{r'dt} \int_0^{r'} \{h(r, t' + dt) - h(r, t')\} \, r dr. \tag{3.1}$$

The detailed derivation of this equation is explained in Appendix A. Since the relaxation dynamics slows down as time goes on, logarithmically-increasing time bins are employed for dt, i.e., $dt = 0.1 \times \sqrt{2}^n$ s ($n = 0, 1, 2, \cdots$). The validity of these logarithmically-increasing time bins is discussed in Appendix B. The slope $|\nabla h|$ at position $r = r'$ is calculated by the least-squares method using profiles from $r = r' - \Delta r/2$ to $r = r' + \Delta r/2$.

The relation between q and $|\nabla h|$ is plotted in figure 3.1. The data suggest that q is not scaled by only $|\nabla h|$, but depends on the analysis position r. This is inconsistent with the argument of the Roering1999 model (1.54), i.e., the flux is determined by only the slope when the vibration conditions are fixed (section 1.3.3). Therefore, regarding the data obtained in our experimental system, comparing q with $|\nabla h|$ would not be appropriate when modelling the flow property with a sole transport model. To explain this complex flow property and reproduce the granular-heap relaxation, the transport model will be modified in the next subsection.

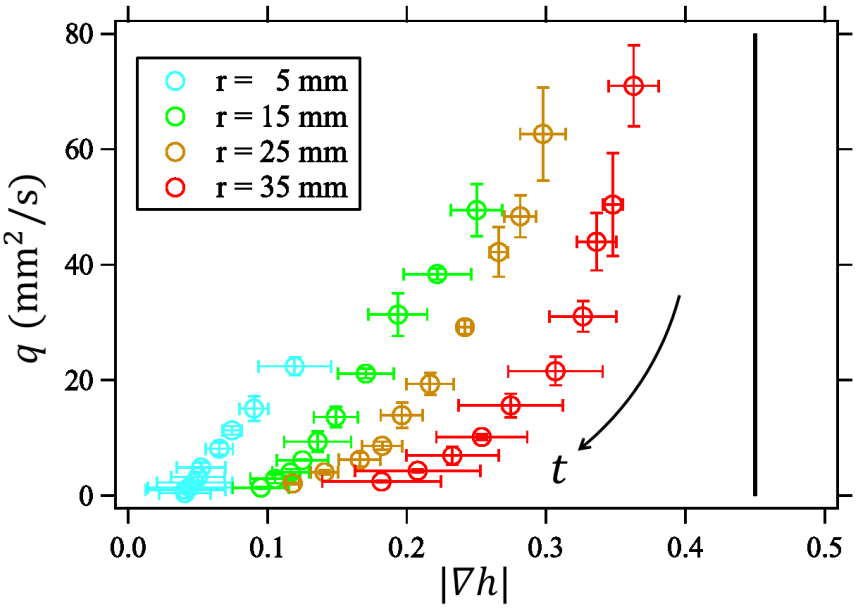

Figure 3.1: Relation between flux q and slope $|\nabla h|$. Colours represent analysis positions. A black line corresponds to the angle of repose: $|\nabla h| = \tan\theta_c$. Cited from Tsuji et al. (2018).

3.2 Nonlinear Diffusion Transport (NDT) model

The Roering1999 model (1.54) is derived assuming the shear-band structure that only a surface layer with constant thickness is fluidised. Rather than this, because the system is subjected to relatively strong vibration of $\Gamma \geq 2$ in this study, employed here is the all-layers-fluidisation assumption coupled with the sliding-block approximation. This approach resembles the one used to explain the spreading dynamics of a horizontally-vibrated granular heap (section 1.3.2). Other fundamental concepts of the model derivation are the same as proposed by Roering et al. (1999).

Let us consider the dynamics of an infinitesimal annular slice of granular media with width dr and height $h(r)$ as illustrated in figure 3.2. From the sliding-block approximation, this slice is regarded as a continuum block. Assuming the hydrostatic pressure and the incompressibility (i.e., the packing fraction ϕ is constant), the pressure gradient along the r direction can be written as $dP/dr = \rho_\phi g|\nabla h|$, where $\rho_\phi = \rho\phi$ is the bulk density. Thus, the force applied to the slice by the pressure gradient is calculated as

$$\begin{aligned} F_\mathrm{p} &= \int_0^{2\pi}\left(\int_0^{h(r)} \frac{dP}{dr} dr dz\right) r d\theta \\ &= 2\pi r \rho_\phi g h(r) dr |\nabla h| \\ &= mg|\nabla h|, \end{aligned} \tag{3.2}$$

where $m = 2\pi\rho_\phi h(r)dr$ is the mass of the slice. Likewise, the frictional force in motion F_f can be written as

$$F_\mathrm{f} = \mu mg. \tag{3.3}$$

The pressure gradient force always works along the positive direction of the r axis, while the frictional force is applied along the opposite direction of the motion.

As a next step, based on the energy-equipartition model proposed by Roering et al. (1999), we assume that the oscillating disk isotropically supplies energy ΔE to the granular heap during infinitesimal time Δt, such that the slice is able to move along all directions with equal probabilities like a random walk process. In other words, during Δt the vibration works to transport the slice to the positive direction of the r axis with velocity v_+ and probability $1/2$, while to the negative direction with velocity v_- and probability

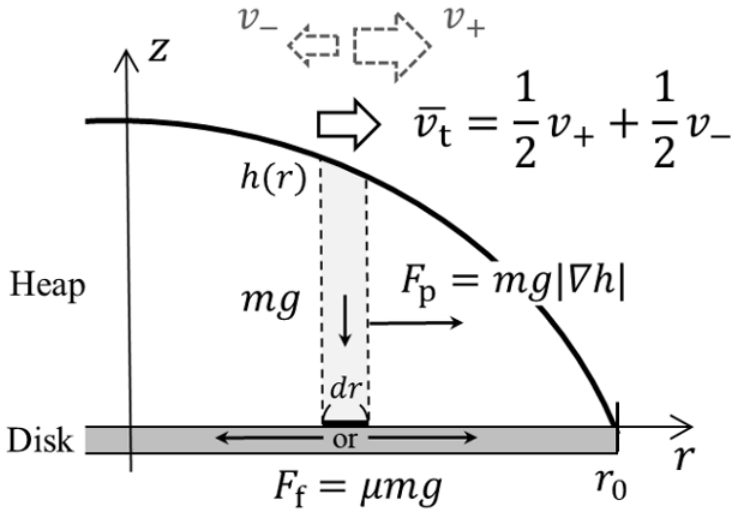

Figure 3.2: Image of the NDT model. The all-layers-fluidisation assumption coupled with the sliding-block approximation is used. The energy is supplied from the vibrating disk to the heap, based on the energy-equipartition model.

1/2 as well. This process is repeated as long as the vibration energy is injected. Similar modelling has also been developed for coarsening dynamics in a vibro-fluidised compartmentalised granular gas (van der Meer et al., 2004). The important point in this modelling is that the absolute value of v_+ is larger than v_- because the resistance force against the motion along the positive direction $F_+ = F_f - F_p$ is smaller than that along the negative direction $F_- = F_f + F_p$. Assuming that the inputted energy always balances the dissipative energy due to the resistance force, the average transport velocity along the r axis $\bar{v}_t$ can be written as

$$\begin{aligned} \bar{v}_t &= \frac{1}{2}v_+ + \frac{1}{2}v_- \\ &= \frac{1}{2}\frac{\Delta E}{\Delta t}\left(\frac{1}{F_+} - \frac{1}{F_-}\right) \\ &= \frac{W}{2mg}\left(\frac{1}{\mu - |\nabla h|} - \frac{1}{\mu + |\nabla h|}\right), \end{aligned} \tag{3.4}$$

where $W = \Delta E/\Delta t$ means the average work done per unit time, that is, power.

As a final step, let us express power W more specifically. The total vibration power

applied to the slice W_{vib} can be expressed as

$$W_{\mathrm{vib}} = mgv_{\mathrm{vib}}, \tag{3.5}$$

where $v_{\mathrm{vib}} = A(2\pi f)$ represents the maximum vibration velocity. Of course, 100% of W_{vib} can not be used for the horizontal granular transport. Therefore, let us suppose that a certain percentage of the vibration energy inputted vertically is used for the horizontal transport of the slice. This idea allows W to take the following simple form:

$$\begin{aligned} W &= cW_{\mathrm{vib}} \\ &= cmgv_{\mathrm{vib}}, \end{aligned} \tag{3.6}$$

where c means the energy conversion efficiency from vertical vibration to horizontal granular transport. Note that, however, taking the fluidisation condition into consideration, the energy conversion efficiency c takes two different forms:

$$c \begin{cases} > 0 & | \quad \text{if } \Gamma > \Gamma_{\mathrm{c}} \\ = 0 & | \quad \text{otherwise.} \end{cases} \tag{3.7}$$

The upper condition means that vibration fluidises the granular heap, while the lower condition corresponds to the situation that vibration is not strong enough to destabilise the granular heap, i.e., the impulsive force between the disk and granular layer is zero. Substituting equation (3.6) into equation (3.4), the average transport velocity $\bar{v}_{\mathrm{t}}$ can be rewritten as

$$\bar{v}_{\mathrm{t}} = \frac{cv_{\mathrm{vib}}}{\mu^2} \frac{|\nabla h|}{1 - (|\nabla h|/\mu)^2}. \tag{3.8}$$

According to this model, when $|\nabla h| \ll \mu$, the flux $q(= h\bar{v}_{\mathrm{t}})$ is almost proportional to $|\nabla h|$, which can be interpreted as Fick's law of diffusion. On the other hand, q diverges rapidly as $|\nabla h|$ approaches μ, indicating strong nonlinearity. Therefore, equation (3.8) is hereinafter referred to as the nonlinear diffusion transport (NDT) model. In the next subsection, we will verify whether the NDT model can consistently explain the experimental data.

3.3 Consistency between the NDT model and experimental data

3.3.1 Relationship between depth-averaged velocity and slope

In the actual data measurement, $\bar{v}_t$ corresponds to the depth-averaged velocity calculated as q/h. If the NDT model is correct, $\bar{v}_t(= q/h)$ must be a function of only $|\nabla h|$, in contrast to q which depends on both $|\nabla h|$ and r as shown in figure 3.1. Figure 3.3 shows the relation between $\bar{v}_t(= q/h)$ and $|\nabla h|$. As expected, all of the data are collapsed into a single curve and can be fitted by the NDT model (3.8). Here, the fitting parameter is only c because μ is fixed at $\tan\theta_c$ in table 2.1 on the basis of Amontons-Coulomb's friction law (1.1). Although more complex friction laws such as equations (1.5) and (1.53) could be implemented, this simplified relation often allows us to capture the overall trend of granular-flow properties as a first step (e.g., Savage and Hutter, 1989; Gray et al., 2003). In fact, it has been confirmed that the scaling of figure 3.3 is universal to all of experimental data. The inset of figure 3.3 shows analysis results for various vibration conditions, in which $\bar{v}_t$ is scaled by only $|\nabla h|$ as well and the data are also fitted well by the NDT model (3.8).

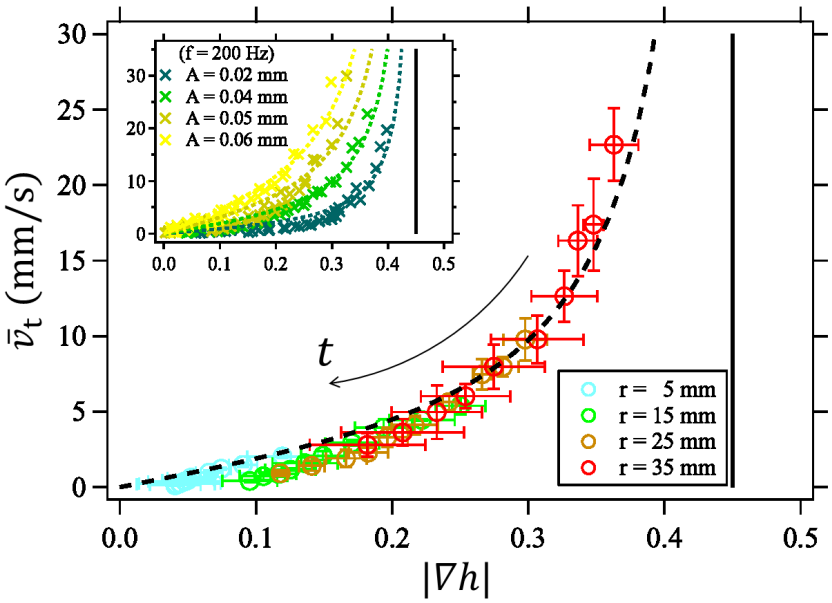

Figure 3.3: Relation between depth-averaged velocity $\bar{v}_t$ and slope $|\nabla h|$. Colours represent analysis positions. The data points shift to a smaller $|\nabla h|$ range as time passes. A vertical solid line corresponds to $|\nabla h| = \tan\theta_c$, where $\bar{v}_t$ diverges. A dashed curve shows the best fitting by the NDT model (3.8). Inset: Analysis results for various vibration strength. The axes are the same as the main panel. All of the data are also fitted by the NDT model (3.8).

3.3.2 Energy conversion efficiency for depth-averaged velocity

Another point that needs to be confirmed is the parameter dependence of c, which is the fitting parameter in figure 3.3. The values of c, which are calculated by the least-squares fitting to the NDT model (3.8), are plotted as a function of v_{vib} for various granular materials (table 2.1) in figure 3.4. The result suggests that c is almost independent of any experimental conditions and shows a nearly constant value:

$$c = 0.068 \pm 0.014. \tag{3.9}$$

Since c indicates the energy conversion efficiency from vertical vibration to horizontal granular transport, it is natural that c is less than 1 and uniquely determined by the system itself. In any case, the analysis results shown in figures 3.3 and 3.4 support the validity of the NDT model.

However, the specific value of c (equation (3.9)) indicates that only less than 10% of the inputted energy is used for the granular transport. Actually, in other types of experiments, it is known that the majority of inputted energy is not used for the granular transport. Let us take low-speed impact of a solid projectile onto a granular bed for example. In the crater formation process, a part of impactor's kinetic energy is used to transport (or excavate) granular media. Laboratory experiments by Hayashi and Sumita (2017); Takizawa and Katsuragi (2020) imply that the energy necessary to lift up granular mass equivalent to the crater volume against gravity is very small ($\lesssim 1\%$), compared with the kinetic energy.

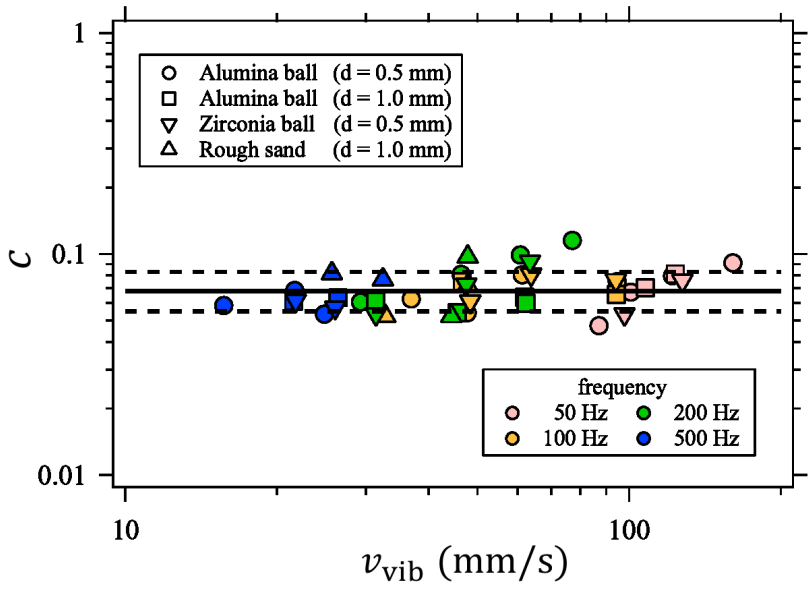

Figure 3.4: Energy conversion efficiency c as a function of the maximum vibration velocity v_{vib}. Colours and symbols represent vibration frequency f and granular materials listed in table 2.1, respectively. Solid and dashed lines show $c = 0.068$ with $1\sigma = 0.014$. Cited from Tsuji et al. (2018).

3.3.3 Relationship between surface velocity and slope

Next, we investigate whether the NDT model holds in particle scale. While the depth-averaged velocity is calculated from the relaxation of profiles, the surface velocity can also be estimated by the pattern matching of successive profile images. The applied algorithm is similar to the particle image velocimetry (PIV) method (Lueptow et al., 2000), although the profile data of this study is one-dimensional. Small spacial windows for the profile pattern matching are given by ±5 mm at each position ($r = 5, 15, 25, 35$ mm) as well as the computation of slope $|\nabla h|$. Adequate and appropriate time interval Δt is then chosen so that the distance of displacement can be clearly identified as seen in figure 2.8. This distance is determined by finding the position where one-dimensional cross-correlation function between two profiles shows the maximum value. Here, we define Δr as the r component of this displacement (not along the surface) as the depth-averaged velocity $\bar{v}_t$ is also measured along the r direction. Consequently, the surface velocity along the r direction v_{t0} can be estimated by $\Delta r/\Delta t$. The range of Δt is properly chosen so that the typical Δr is a few grain diameter. The detail of this pattern matching is summarised in Appendix C.

Figure 3.5 shows the comparison between v_{t0} and $|\nabla h|$, where the temporal resolution is the same as the depth-averaged velocity (figure 3.3). Interestingly, v_{t0} is scaled by only $|\nabla h|$ as well as $\bar{v}_t$ in figure 3.3, and the data can also be fitted by the NDT model:

$$v_{t0} = \frac{c_0 v_{vib}}{\mu^2} \frac{|\nabla h|}{1 - (|\nabla h|/\mu)^2}, \tag{3.10}$$

where c_0 is a constant, physically corresponding to the energy conversion efficiency for the surface flow. As can be seen in the inset of figure 3.5, this relation also holds for the other experimental data. The remarkable point is that the surface velocity does not depend on the height h. In other words, the surface velocity is constant whether the measurement position is upstream or downstream as long as the slope $|\nabla h|$ is the same.

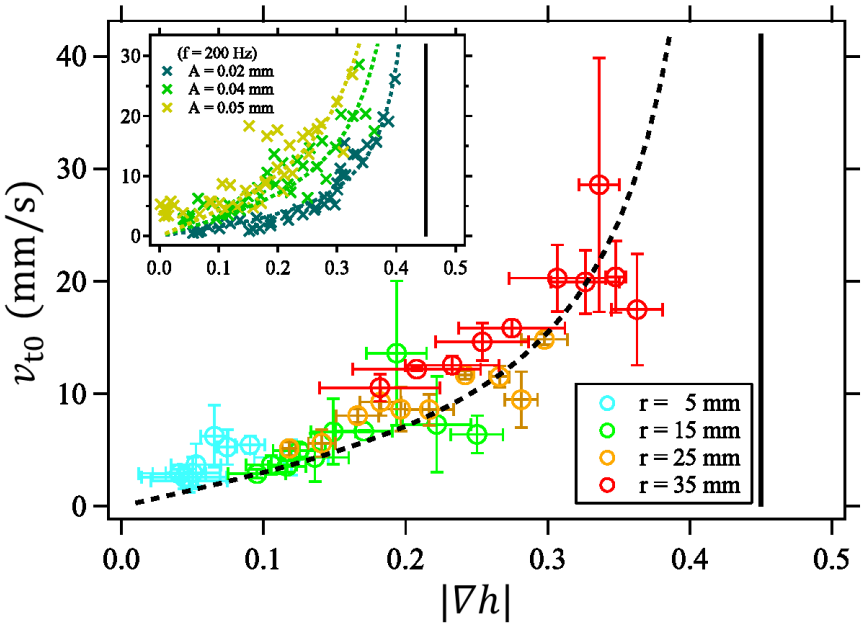

Figure 3.5: Relation between surface velocity v_{t0} and slope $|\nabla h|$. Colour represents analysis positions. A dashed curve and solid line show the best fitting by the NDT model for surface velocity (3.10) and the divergent point $|\nabla h| = \tan\theta_c$, respectively. The best fitted value of c_0 is 0.12. Inset: Analysis results for various vibration strength. The axes are the same as the main panel. All of the data are also fitted by the NDT model for surface velocity (3.10). Cited from Tsuji et al. (2019).

3.3.4 Energy conversion efficiency for surface velocity

Here we also investigate the dependence of c_0 on experimental conditions. Figure 3.6 plots c_0 versus v_{vib} for various granular materials (table 2.1). Note that the data in strong vibration conditions ($v_{\mathrm{vib}} > 70$ mm/s) is not plotted because the fluctuation of surface profiles is too large to apply the pattern matching algorithm. Although the data range is slightly limited, the same flat trend as in figure 3.4 is observed as well, showing the average value:

$$c_0 = 0.11 \pm 0.022. \tag{3.11}$$

The value of c_0 is approximately twice as large as c:

$$c_0 \approx 2c, \tag{3.12}$$

which suggests that the flow velocity on the top of the relaxing heap is also approximately twice as large as the depth-averaged velocity; and the flow has a structure that the velocity decreases as going deeper from the surface. This tendency is qualitatively consistent with shear-band structure of conventional heap flows introduced in section 1.2.5, i.e., a clearly fluidised region is localised around the surface.

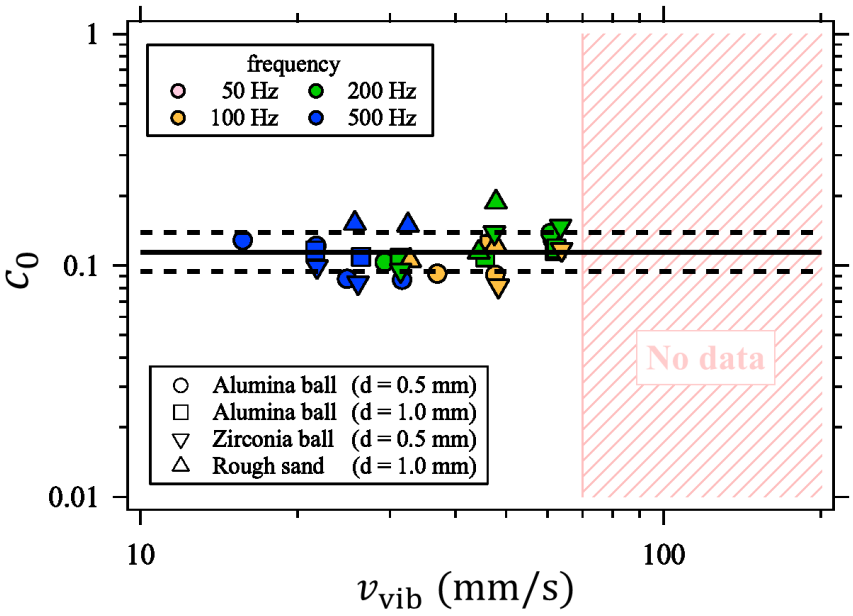

Figure 3.6: Fitting parameter of equation (3.10) c_0 as a function of the maximum vibration velocity v_{vib}. The value of c_0 physically corresponds to the energy conversion efficiency for the surface velocity. Black solid and dashed lines draw $c_0 = 0.11$ with $1\sigma = 0.022$. In the range of $v_{\mathrm{vib}} > 70$ mm/s, which is the area hatched in light red, the pattern matching algorithm cannot be used due to the strong fluctuation of profiles.

3.4 Reproduction of the relaxation process

Since the flux q can be given by $h\bar{v}_t$, the relaxation process of the heap can be reproduced by the equation of continuity:

$$\begin{aligned} \frac{\partial h}{\partial t} &= -\nabla \cdot q \\ &= \nabla \cdot \left(h \frac{c v_{\mathrm{vib}}}{\mu^2} \frac{\nabla h}{1 - (|\nabla h|/\mu)^2} \right). \end{aligned} \tag{3.13}$$

This equation, which governs the relaxation process, does not include the dependence on grain size d. This is because the relevant length scale governing the relaxation dynamics is the height $h(r)$ rather than d under the all-layers-fluidisation assumption. Figure 3.7 compares the numerically-reproduced relaxation profile with the actual experimental data. Note that, when solving equation (3.13), the following boundary conditions are imposed from the experimental configuration: $q = 0\ \mathrm{mm}^2/\mathrm{s}$ at $r = 0$ mm and $h_R(t) = h(t, R)$, where $h_R(t)$ is the thickness of a granular layer flowing out of the disk at a given time, which typically consists of a few grain diameters. Numerical profiles (red curves) agree well with the experimental data (grey curves), especially in early time. This agreement also supports the fact that the NDT model can appropriately capture the heap-flow property.

However, one might notice that model curves exhibit misfits with experimental data when slopes approach zero. Actually, figure 3.3 also shows the same trend. These facts suggest that when the shape of the heap get flattened to some extent, granular media reach a jammed state, where the relaxation almost halts. The detailed discussion for this point will be given later.

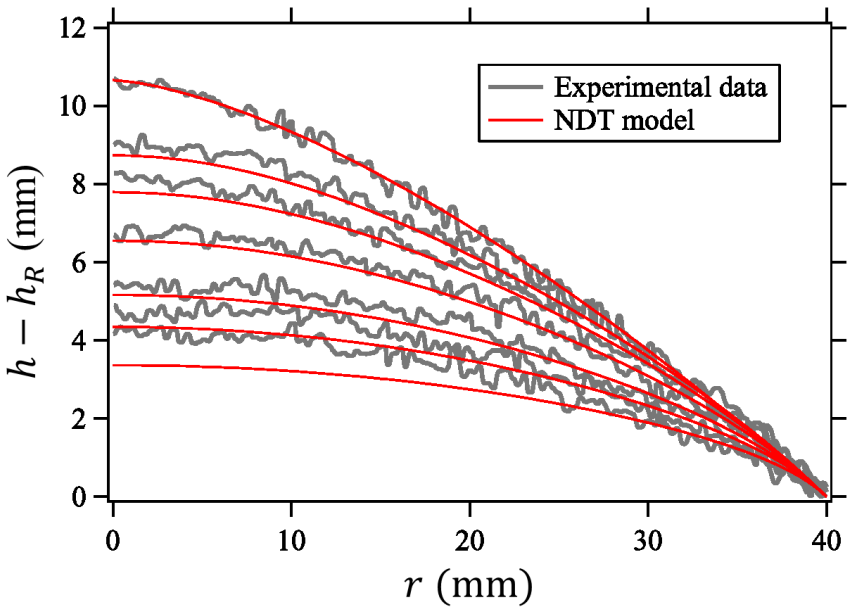

Figure 3.7: Comparison between profiles obtained by the laser profiler and those computed on a basis of the NDT model. The initial shape for the model computation is approximated by $h - h_R \sim (R^{1.6} - r^{1.6})$ with $R = 40$ mm. The time step and spatial resolution of the numerical calculation are 10^{-5} s and 0.5 mm, respectively. For computation, the central difference scheme is used. Cited from Tsuji et al. (2018).

3.5 Open issue

So far, with the aim of understanding the dynamics of heap flows under vertical vibration, systematic laboratory experiments have been conducted. The experimental result can be explained by the NDT model (3.8) that we propose, which differs from the Roering1999 model (1.54). The primary difference is that the NDT model relates the slope to the depth-averaged velocity, not the flux as in the Roering1999 model. However, although the NDT model is derived under the all-layers-fluidisation assumption, the surface velocity estimated by the profile pattern matching suggests that the flow velocity decreases with depth from the surface. To verify the consistency between this observed result and the NDT model, the internal velocity profile needs to be investigated. This point is also closely related to the following question: Why is the depth-averaged velocity determined by only the slope when the experimental conditions are fixed? On the analogy of conventional granular flows down an inclined plate as introduced in section 1.2.4, it might be more natural that the depth-averaged velocity also depends on the height of the heap. Additionally, it is also remarkable that the surface velocity does not show the dependence on the height. Discussing the internal velocity profile is necessary to develop a better understanding of heap-flow dynamics and could also be a key to give the clear reason why the difference between the NDT model and the Roering1999 model arises. To solve these open issues, numerical simulations are much more convenient than experimental approaches for the setup of this study (figure 2.1). From the next session, we will go into the discussion regarding numerical results.

4 Numerical setup

4.1 Discrete Element Method

Particle-scale simulations are performed in both two dimensions (2D) and three dimensions (3D) by means of the discrete element method (DEM) (Cundall and Strack, 1979). Modelled in this study are N polydisperse disks (2D) or spheres (3D) of constant material density with the maximum diameter d and mass m. A small polydispersity equally ranging from $d/\sqrt{2}$ to d is given in order to prevent the crystallisation (e.g., Iikawa et al., 2016). The position, velocity, and angular velocity of ith particle are denoted by $\boldsymbol{r}_i$, $\boldsymbol{v}_i$, and $\boldsymbol{\omega}_i$, respectively. The total force applied on ith particle is determined by a combination of gravity and the contact force with jth particle $\boldsymbol{f}_{ij}$, which consists of the normal part $\boldsymbol{f}_{ij}^{(\mathrm{n})}$ and tangential part $\boldsymbol{f}_{ij}^{(\mathrm{t})}$, i.e., $\boldsymbol{f}_{ij} = \boldsymbol{f}_{ij}^{(\mathrm{n})} + \boldsymbol{f}_{ij}^{(\mathrm{t})}$.

An image of the contact force in DEM simulations is drawn in figure 4.1. For a pair of two contacting ith and jth particles with diameters d_i and d_j, the normal compression δ_{ij} and relative velocity $v_{ij}^{(\mathrm{n})}$ are given by

$$\delta_{ij} = \left(d_i + d_j\right)/2 - \left|\boldsymbol{r}_{ij}\right|, \tag{4.1}$$

$$v_{ij}^{(\mathrm{n})} = \boldsymbol{v}_{ij} \cdot \boldsymbol{n}_{ij}, \tag{4.2}$$

where $\boldsymbol{r}_{ij} = \boldsymbol{r}_i - \boldsymbol{r}_j$, $\boldsymbol{v}_{ij} = \boldsymbol{v}_i - \boldsymbol{v}_j$, $\boldsymbol{n}_{ij} = \boldsymbol{r}_{ij}/\left|\boldsymbol{r}_{ij}\right|$. The normal contact force $\boldsymbol{f}_{ij}^{(\mathrm{n})}$ is modelled using a normal spring constant $k^{(\mathrm{n})}$ and viscous constant $\eta^{(\mathrm{n})}$ as

$$\boldsymbol{f}_{ij}^{(\mathrm{n})} = \Theta\left(\delta_{ij}\right)\left(k^{(\mathrm{n})}\delta_{ij} - \eta^{(\mathrm{n})}v_{ij}^{(\mathrm{n})}\right)\boldsymbol{n}_{ij}, \tag{4.3}$$

where $\Theta(x)$ is the Heaviside step function, i.e., $\Theta(x) = 1$ for $x \geq 0$ and $\Theta(x) = 0$ otherwise.

Meanwhile, the tangential contact force $\boldsymbol{f}_{ij}^{(\mathrm{t})}$ is modelled with a tangential spring constant $k^{(\mathrm{t})}$ as

$$\boldsymbol{f}_{ij}^{(\mathrm{t})} = -k^{(\mathrm{t})}\boldsymbol{u}_{ij}, \tag{4.4}$$

where the tangential displacement $\boldsymbol{u}_{ij}$ is obtained by integrating the tangential relative

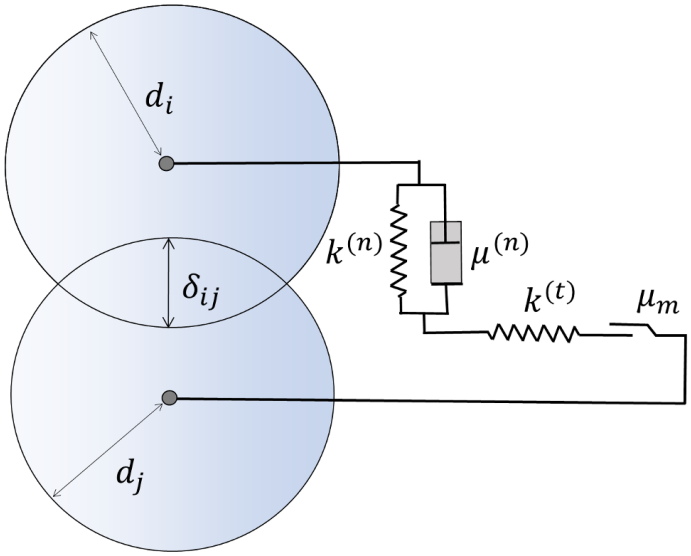

Figure 4.1: Image of the contact force in DEM simulations.

velocities $\boldsymbol{v}_{ij}^{(\mathrm{t})}$, which are expressed as

$$\boldsymbol{u}_{ij} = \int_{\mathrm{stick}} \left(\boldsymbol{v}_{ij}^{(\mathrm{t})} - \frac{(\boldsymbol{u}_{ij} \cdot \boldsymbol{v}_{ij})\boldsymbol{r}_{ij}}{\left|\boldsymbol{r}_{ij}\right|^2} \right) dt, \tag{4.5}$$

$$\boldsymbol{v}_{ij}^{(\mathrm{t})} = \boldsymbol{v}_{ij} - v_{ij}^{(\mathrm{n})}\boldsymbol{n}_{ij} - \frac{1}{2}\left(d_i\boldsymbol{\omega}_i + d_j\boldsymbol{\omega}_j\right) \times \boldsymbol{n}_{ij}, \tag{4.6}$$

where the second term in the integral of equation (4.5) insures that $\boldsymbol{u}_{ij}$ always lies on the tangent plane of the contact point. In equation (4.5), "stick" means that the integral is performed only when $\left|\boldsymbol{f}_{ij}^{(\mathrm{t})}\right| < \mu_m \left|\boldsymbol{f}_{ij}^{(\mathrm{n})}\right|$ is satisfied, where μ_m is a microscopic friction coefficient. This condition indicates that the Coulomb friction criterion holds in quasistatic motion: $\left|\boldsymbol{f}_{ij}^{(\mathrm{t})}\right| = k^{(\mathrm{t})}|\boldsymbol{u}_{ij}|$ in the "stick" region of $\left|\boldsymbol{u}_{ij}\right| < \mu_m \left|\boldsymbol{f}_{ij}^{(\mathrm{n})}\right| / k^{(\mathrm{t})}$, while $\left|\boldsymbol{f}_{ij}^{(\mathrm{t})}\right|$ remains $\mu_m \left|\boldsymbol{f}_{ij}^{(\mathrm{n})}\right|$ in the "slip" region of $\left|\boldsymbol{u}_{ij}\right| \geq \mu_m \left|\boldsymbol{f}_{ij}^{(\mathrm{n})}\right| / k^{(\mathrm{t})}$. In addition, the torque $\boldsymbol{T_i}$ of ith particle is given by

$$\boldsymbol{T}_i = -\sum_j \frac{d_i}{2}\boldsymbol{n}_{ij} \times \boldsymbol{f}_{ij}^{(\mathrm{t})}. \tag{4.7}$$

Using the above contact forces, the translational and rotational accelerations of ith

particle are determined by Newton's second law:

$$m_i \ddot{\boldsymbol{r}}_i = \sum_j \boldsymbol{f}_{ij} + m_i \boldsymbol{g}, \tag{4.8}$$

$$I_i \dot{\boldsymbol{\omega}}_i = \boldsymbol{T}_i, \tag{4.9}$$

where m_i and I_i are the mass and moment of inertia of ith grain, and $\boldsymbol{g} = (0, 0, -g)$ is gravity. In our simulation, d, m, and g are set to be unity, and all of the quantities are computed in dimensionless forms, where the unit time is $\sqrt{d/g}$. After the computation, we give dimensions to all quantities using the same units as the experiment ($d = 0.5$ mm, $m = 2.5 \times 10^{-4}$ g, and $g = 9800$ mm/s^2).

Another important point in DEM simulations is how to choose mechanical parameters; (i) $k^{(\mathrm{n})}$, (ii) $k^{(\mathrm{t})}$, (iii) $\eta^{(\mathrm{n})}$, and (iv) μ_m. In general, the appropriate setting of mechanical parameters are essential to reproduce the realistic behaviour of particles by DEM simulation. The values of the above four parameters that we used in the simulation are summarised in table 4.1, which are determined as follows: (i) This study adopts sufficiently hard spheres and disks ($k^{(\mathrm{n})} = 10^4$ $[mg/d]$) so that this choice does not have an influence on the simulation result. In fact, the simulation result changes mostly only within error even if $k^{(\mathrm{n})} = 10^5$ or 10^6 $[mg/d]$ is used. (ii) The ratio $k^{(\mathrm{t})}/k^{(\mathrm{n})}$ depends on the material property of particles, which is typically set to be $k^{(\mathrm{t})}/k^{(\mathrm{n})} = 2/7$–$2/3$ in DEM simulations. However, we found that the result is not sensitive to this ratio in this study. Although all of the results shown below are obtained with $k^{(\mathrm{t})}/k^{(\mathrm{n})} = 2/7$, the data using $k^{(\mathrm{t})}/k^{(\mathrm{n})} = 2/5$ or $2/3$ change only within error as well. (iii) The combination of $k^{(\mathrm{n})}$ and $\eta^{(\mathrm{n})}$ determines the coefficient of restitution e, which characterises the energy loss due to inelastic collisions. The coefficient of restitution e is defined as the ratio of the post-collisional to pre-collisional normal relative velocity, and can be analytically written as

$$e = \exp\left(-\eta^{(\mathrm{n})} t_{\mathrm{col}}/m\right), \tag{4.10}$$

where t_{col} is the collision time:

$$t_{\mathrm{col}} = \frac{\pi}{\sqrt{2k^{(\mathrm{n})}/m - {\eta^{(\mathrm{n})}}^2/m^2}} \tag{4.11}$$

To investigate the dependence on the degree of inelasticity, we vary e from 0.7 to 0.9 by arranging $\eta^{(\mathrm{n})}$. As a result, we have confirmed that e does not affect simulation results. Therefore, $e = 0.8$ is used in this study. (iv) In contrast, a microscopic friction coefficient μ_m has a little influence on the result. In this study, relatively large friction $\mu_m = 0.8$ is employed. The reason for this choice is that, as will be explained in section 4.2, the angle of repose θ_c approaches the experimental value most in the range of $\mu_c \geq 0.8$ (or even 0.6). Once μ_c is in this range, the bulk flow property does not change. The dependence on these four parameters (i)–(iv) is discussed in more detail in Appendix D. In the following, we use the parameter values in table 4.1 for the standard setting unless otherwise noted.

Last but not least, care must be taken for the time step of the calculation δt. In our simulation, when creating the heap with the angle of repose, $\delta t \approx t_{\mathrm{col}}/5$ is employed. When applying vibration, the bulk flow property is not sensitive to δt once it becomes less than $t_{\mathrm{col}}/20$. Therefore, all of the simulations during vibration are conducted with the time step $\delta t < t_{\mathrm{col}}/20$.

Note that numerical results presented in this thesis are slightly different from our published original paper (Tsuji et al., 2019), although their model specifics are identical. The reason is that we found a minor bug in the code: implementation of gravity was partially incorrect. However, the influence of this bug is rather limited because the driving force of a granular flow is dominated by vibration rather than gravity in this study as will be discussed in section 5.2. In fact, quantitative differences resulted from this bug are almost within the margin of error, and the eventual conclusion does not change at all.

Table 4.1: Microscopic mechanical parameters in DEM simulations. These values are used for the standard setting in this thesis unless otherwise noted.

Parameter	Value	Note
$k^{(\mathrm{n})}$	10^4 $[mg/d]$	Normal spring constant
$k^{(\mathrm{t})}/k^{(\mathrm{n})}$	$2/7$	Used to determine the tangential spring constant
$\eta^{(\mathrm{n})}$	10 $[m\sqrt{g/d}]$	Normal viscous coefficient
μ_m	0.8	Microscopic friction coefficient
e	0.8	Restitution coefficient determined by equation (4.10)

4.2 Simulation procedure

Here, the simulation procedure from the creation of a heap to vibration is explained. Firstly, particles are randomly filled into a triangle (2D) or cone (3D) space on a fixed base. In the 2D case, the base is composed of the same grains with diameter d, which are placed without gaps on a straight line. The circular base in the 3D case is created by setting grains with diameter d on intersections of a plane orthogonal grid with intervals of distance d. The system size is, unless otherwise noted, the same as the experiment ($R = 40$ mm). The initial packing fraction ϕ_{init} is set to be slightly smaller than the jamming point (Otsuki and Hayakawa, 2009): $\phi_{\mathrm{init}} = 0.75$ (2D) and 0.55 (3D). The slope of a filled triangle/cone is always larger than the angle of repose θ_{c}. The number of simulated particles is $\sim 5 \times 10^3$ (2D) and $\sim 5 \times 10^5$ (3D).

Next, by imposing gravity to all particles simultaneously, a heap with the angle of repose is spontaneously created. As reported by Zhou et al. (2001, 2002), it turns out that the angle of repose θ_{c} depends on the coefficient of microscopic friction μ_m. Figure 4.2 shows the relation between μ_m and $\tan\theta_{\mathrm{c}}$ in 2D simulations, which suggests that θ_{c} increases with μ_m and almost saturates in the range of $\mu_m \geq 0.8$ (or even 0.6). This trend is qualitatively consistent with the report by da Cruz et al. (2005), who also showed that the effective friction increases with μ_m but saturates at a certain point. Moreover, the asymptotic value of θ_c in figure 4.2 is less than θ_c of real grains listed in table 2.1. This is because simulated particles are completely spherical in contrast to real grains with surface roughness which leads to strengthening of the bulk frictional property. As shown in Appendix D, we have confirmed that the flow property does not change once μ_m exceeds 0.8 as the bulk frictional property does not change either. In order to reproduce as realistic a heap as possible, $\mu_m = 0.8$ is employed unless otherwise noted in this study. The resultant angle of repose is $\tan\theta_{\mathrm{c}} = 0.36$ (2D) and 0.39 (3D).

Finally, particles at the base are vertically vibrated with $A\sin(2\pi f)t$ in the same way as the experiment. Note that we use a smaller amplification period ($T_{\mathrm{a}} = 0.25$ s) than laboratory experiments so that the flow property can be measured in broad $|\nabla h|$ ranges. The time evolution of a simulated vibrated heap is shown in figure 4.3 for both 2D and 3D cases, where the vibration conditions are $A = 0.04$ mm and f = 200 Hz ($\Gamma = 6$). In this

vibration condition, the time step of the simulation is much less than the vibration period (i.e., $\delta t \ll f^{-1}$), and the overlap between particles is very small (i.e., $A(2\pi f)\,\delta t \ll d$). When numerical results are discussed, the above vibration conditions are also used for subsequent plots unless otherwise specified. More than 10 and 5 simulation runs for each set of conditions were conducted for the 2D and 3D cases, respectively.

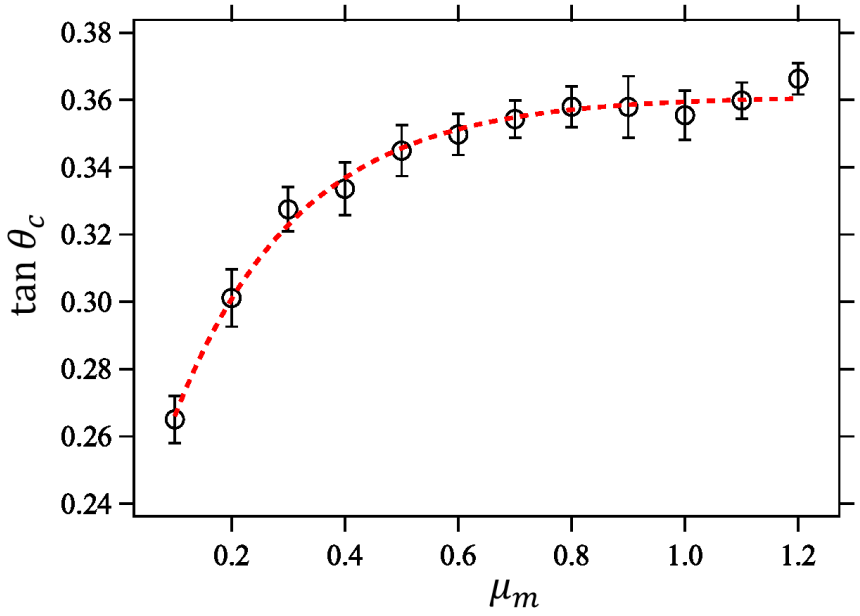

Figure 4.2: Relation between the angle of repose $\tan\theta_c$ and microscopic friction coefficient μ_m. The data are obtained in 2D simulations. A dashed curve is the best fit by an exponential function: $\tan\theta_c = 0.36 - 0.15\exp(-4.6\mu_m)$.

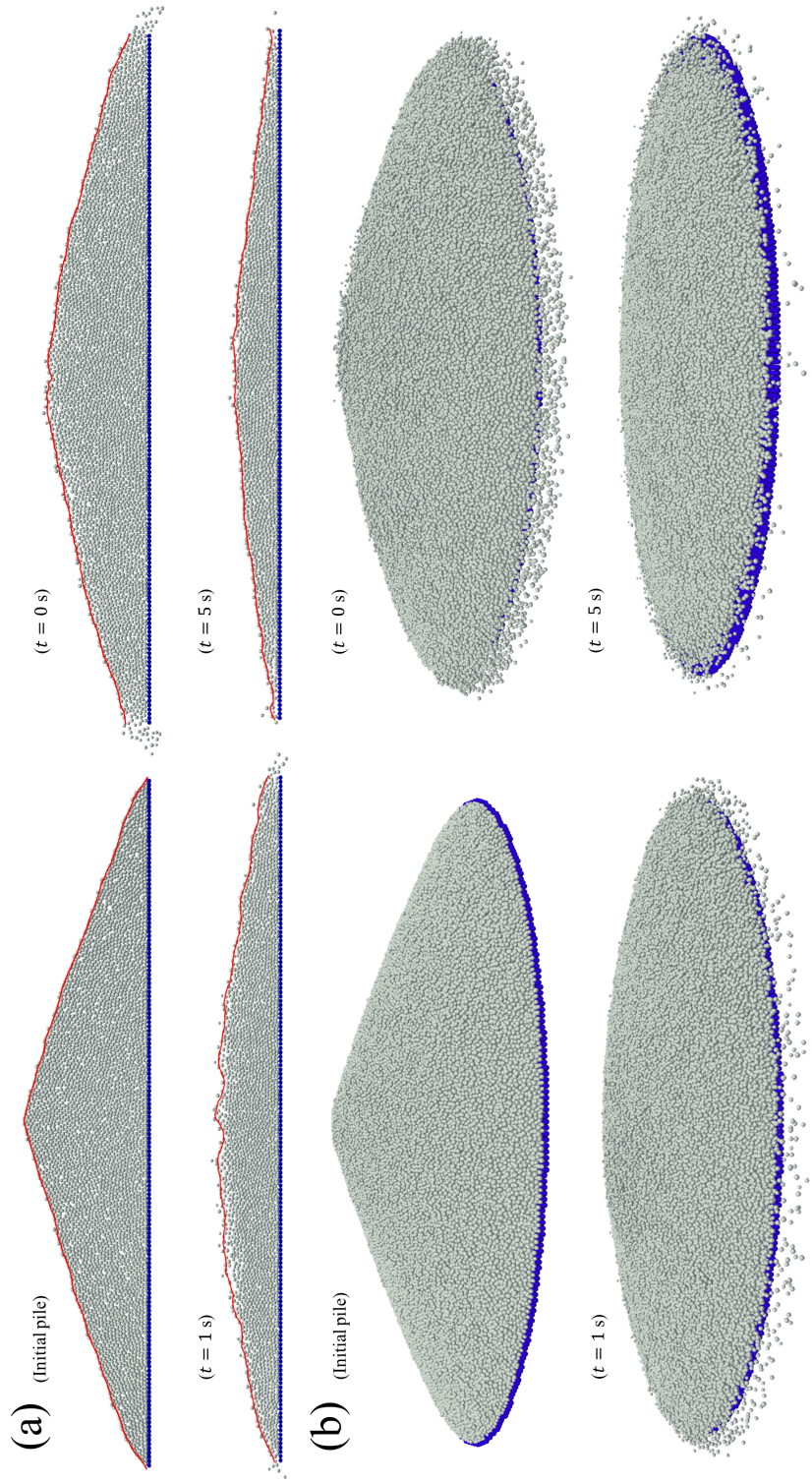

Figure 4.3: Reproduction of the experiment by the DEM simulation. Panels (a) and (b) depict the 2D and 3D simulations, respectively. Only vibrating bottom particles are coloured in dark blue. The first data are taken before applying vibration ($t = -T_a$), and the others are taken at $t = 0, 1, 5$ s. Red curves in Panel (a) are surface profiles computed by the method explained in section 4.3.

4.3 Measurement of surface profiles

From the obtained DEM data, the surface profile is created to confirm the consistency with the experiment. The resolution along the radial direction is set to be $1d$, in which the position of the highest-located particle is given as the actual height h_{act}. However, this raw profile scatters due to the saltation motion of particles, which could lead to a large error on the result. Therefore, to stabilize the data, we take the moving-average with a $5d$ window in the following way:

$$h(r) = \frac{1}{5} \sum_{n=r/d-2}^{r/d+2} h_{\mathrm{act}}(nd). \tag{4.12}$$

As an example, the surface profiles produced by equation (4.12) are drawn onto 2D heaps in figure 4.3(a), which are in good agreement with surface particles.

5 Numerical result

5.1 Consistency with the experimental result

5.1.1 Flux and depth-averaged velocity

The consistency between the experimental and numerical results is firstly confirmed. Figure 5.1 shows the relation between the flux q and slope $|\nabla h|$ obtained in 2D and 3D simulations. Although the flow properties are measured at only three different positions ($r = 10, 20, 30$ mm), other measurement methods are the same as the experiment. As well as the experimental data in figure 3.1, q is not scaled by only $|\nabla h|$. However, when plotting the depth-averaged velocity $\bar{v}_t$ with slope $|\nabla h|$, the data of both 2D and 3D simulations are collapsed into single curves as can be seen in figure 5.2, and can be fitted by the NDT model (3.8). It should be noted, however, that both μ and c are left as free fitting parameters in 2D cases. Although μ was fixed by $\tan\theta_c$ in the experiment using 3D grains (section 3.3.1), μ can be in general different from $\tan\theta_c$ (Ghazavi and Mollanouri, 2008) and also tends to decrease in the presence of vibration (Caballero-Robledo and Clément, 2009). As a matter of fact, $\mu = 0.29$ results in better agreements with the data in figure 5.2 than $\mu = \tan\theta_c = 0.36$. The μ value is almost independent of simulation conditions: μ in 2D cases varies only within 0.28 ± 0.014 (1σ) in the range of $v_{vib} = 30$–80 mm/s, $e = 0.7$–0.9 and $\mu_m = 0.6$–1.0. Thus, the fixed values $\mu = 0.29$, which is set relatively larger than average values to cover a wider $|\nabla h|$ range, are employed for all of the analyses of DEM simulations. In 3D cases, $\mu = \tan\theta_c = 0.39$ is employed, following the analysis method of experimental data using 3D grains.

5.1.2 Energy conversion efficiency for depth-averaged velocity

The dependence of c values on vibration conditions are investigated by varying amplitude with the fixed frequency $f = 200$ Hz. The results are plotted onto the experimental data in figure 5.3. It seems that there is no significant difference between simulations and experiments in terms of the c value. This result supports the fact that our DEM simulation can reproduce laboratory experiments well. In addition, c shows little dependence on spatial dimensions. Therefore, 2D simulations are used for the following analysis.

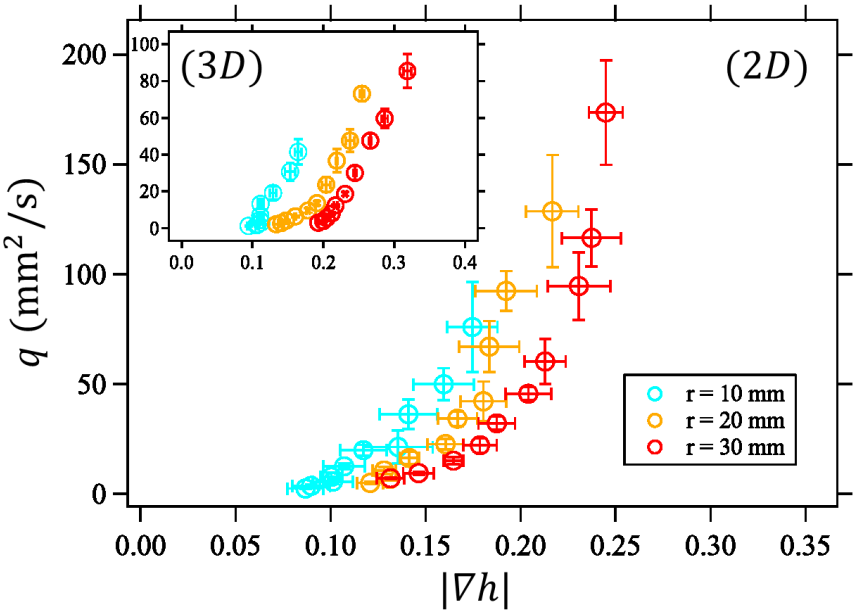

Figure 5.1: Relation between flux q and slope $|\nabla h|$. The main plot and inset correspond to the 2D and 3D cases, respectively. The axes of the inset are the same as the main plot. The colour represents the analysis position.

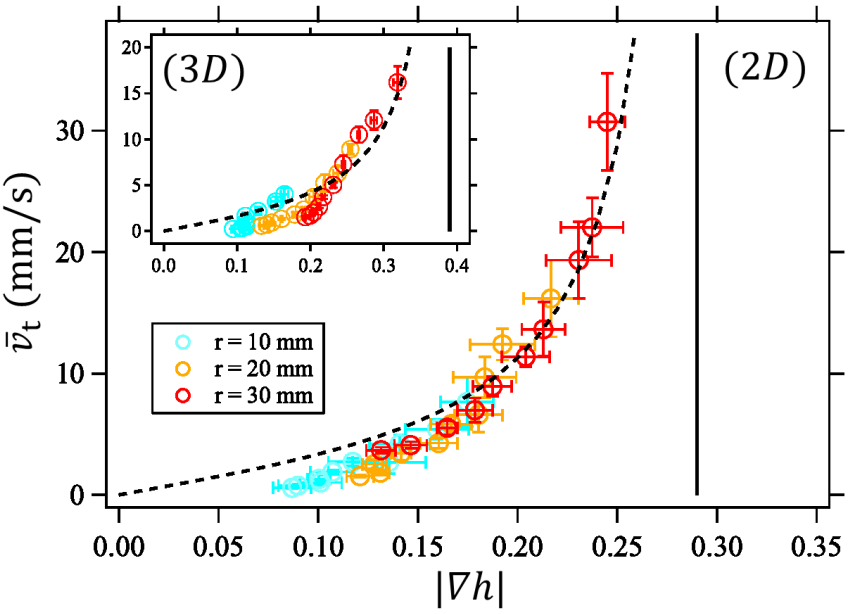

Figure 5.2: Relation between depth-averaged velocity $\bar{v}_t$ versus slope $|\nabla h|$. The main plot and inset correspond to the 2D and 3D cases, respectively. The axes of the inset are the same as the main plot. Both data can be fitted by the NDT model (3.8), which are drawn in dashed curves. The values of μ, drawn in vertical solid lines, are 0.29 (2D) and 0.39 (3D), while the values of c are 0.053 (2D) and 0.050 (3D).

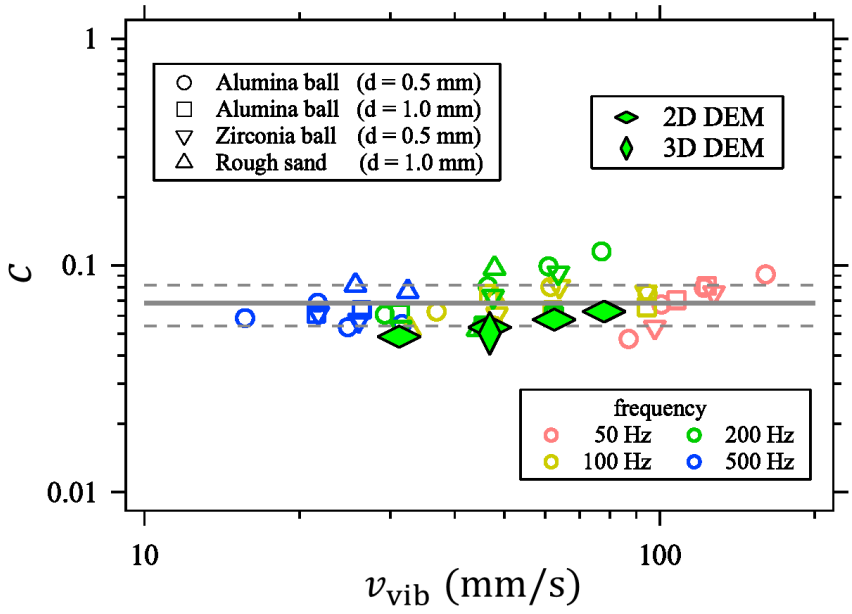

Figure 5.3: Energy conversion efficiency for depth-averaged velocity c as a function of the maximum vibration velocity v_{vib}. The c values computed by the DEM simulations (filled diamonds) are plotted onto experimental results (open circles) for comparison.

5.2 Power inputted by vibration

When deriving the NDT model (3.8) in section 3.2, the total vibration power inputted by vertical vibration W_{vib} is assumed by equation (3.5). The power used for the horizontal vibration W is then defined as W_{vib} multiplied by the energy conversion efficiency c (equation (3.6)). However, equation (3.5) was not directly confirmed by experiment, which gives rise to an uncertainty on the value of the energy conversion efficiency. In other words, if the genuine W_{vib} is less than mgv_{vib}, the value of c in the sense of the genuine energy conversion efficiency is larger, and vice versa. To verify this point, using the data of DEM simulations, we quantitatively evaluate this vibration power as follows.

If equation (3.5) is correct, the total vibration power applied to the whole heap with mass M, denoted by $W_{\mathrm{vib}}^{\mathrm{tot}}$ hereafter, should be

$$W_{\mathrm{vib}}^{\mathrm{tot}} = Mgv_{\mathrm{vib}}. \tag{5.1}$$

On the other hand, the actual vibration power in DEM simulations $W'^{\mathrm{tot}}_{\mathrm{vib}}$ can be directly measured by

$$W'^{\mathrm{tot}}_{\mathrm{vib}} = \frac{d}{dt}\int_{Z(t)}^{Z(t+dt)} -F_b(Z')\,dZ', \tag{5.2}$$

where $Z(t)$ is the position in the z axis at time t, and F_b is the z-component of the total force applied on all of the bottom particles placed at a given position. Figure 5.4 shows the ratio of $W'^{\mathrm{tot}}_{\mathrm{vib}}$ to $W_{\mathrm{vib}}^{\mathrm{tot}}$ for various time t, which suggests that $W'^{\mathrm{tot}}_{\mathrm{vib}}$ is smaller than $W_{\mathrm{vib}}^{\mathrm{tot}}$. This ratio can be understood using the average vibration velocity $\bar{v}_{\mathrm{vib}} = (2/\pi)v_{\mathrm{vib}}$. In figure 5.4, a red dashed line comparable to the simulation data represents $W'^{\mathrm{tot}}_{\mathrm{vib}}/W_{\mathrm{vib}}^{\mathrm{tot}} = 2/\pi$, which implies that the following relation holds:

$$\begin{aligned} W'^{\mathrm{tot}}_{\mathrm{vib}} &= \frac{2}{\pi}W_{\mathrm{vib}}^{\mathrm{tot}} \\ &= Mg\bar{v}_{\mathrm{vib}}. \end{aligned} \tag{5.3}$$

This means that the vibration energy defined by equation (3.5) is overestimated, and consequently the genuine c value should be estimated as $0.068 \times (\pi/2) \approx 0.11$. In any case, the fact remains that the energy conversion efficiency is rather small (~ 0.1).

The contribution of the potential energy also needs to be evaluated. When the heap relaxes, the potential energy that the heap originally holds should convert into the kinetic energy, which could affect the estimation of the energy conversion efficiency. The potential energy of the whole heap U_g can be estimated by

$$U_g = \sum_{i=1}^{N} m_i g h_i, \tag{5.4}$$

where m_i and h_i are the mass and height of ith particle, and the potential energy of particles flowing out of the disk is set zero. The ratio of $\dot{U}_g (= \partial U_g / \partial t)$ to $W^{\mathrm{tot}}_{\mathrm{vib}}$ is shown in the inset of figure 5.4, which indicates that the contribution of the potential energy is rather small. This is also why the bug in the numerical code addressed in section 4.1 did not influence the result.

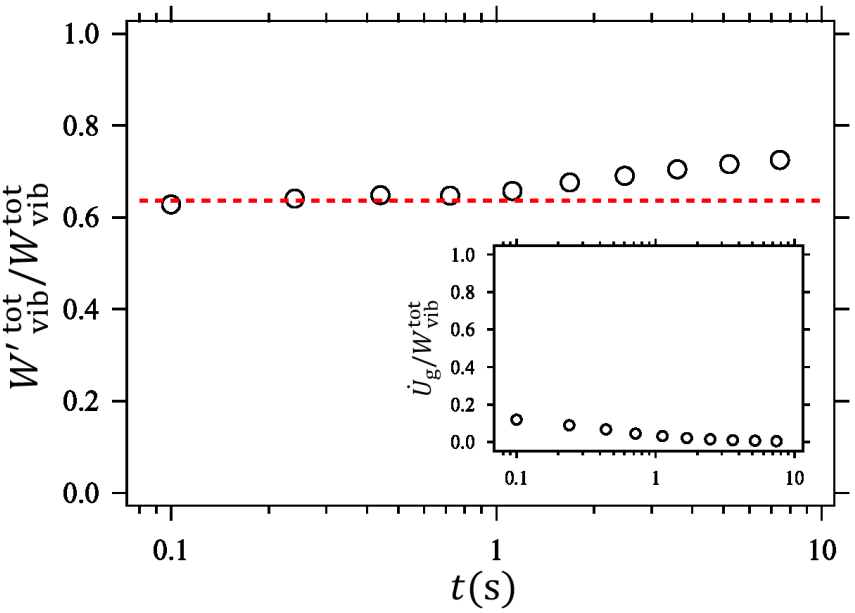

Figure 5.4: The ratio of the power $W'^{\mathrm{tot}}_{\mathrm{vib}}$ to $W^{\mathrm{tot}}_{\mathrm{vib}}$ obtained at various time t. A red line shows $W'^{\mathrm{tot}}_{\mathrm{vib}} = (2/\pi) W^{\mathrm{tot}}_{\mathrm{vib}}$, which is comparable to the simulation data. The value of this red line also corresponds to $\bar{v}_{\mathrm{vib}}/v_{\mathrm{vib}}$. Inset: The ratio of the decreasing rate of the potential energy $\dot{U}_g$ to $W^{\mathrm{tot}}_{\mathrm{vib}}$. When considering the driving force of the granular flow, $\dot{U}_g$ is almost negligible compared to $W^{\mathrm{tot}}_{\mathrm{vib}}$.

5.3 Internal flow dynamics

5.3.1 Velocity profile

The velocity profile inside the relaxing heap, which was technically difficult to address from experimental data, is measured from the simulation data. Here, we introduce the z' coordinate defined by the depth from the surface ($z' = h - z$) : $z' = 0$ and h correspond to the surface and bottom, respectively. The velocity profiles are measured as a function of z' at various times and $r = 10, 20, 30$ mm as figure 5.2 does. As an example, profiles obtained at $r = 20$ mm and various times are shown in figure 5.5. Since h and $|\nabla h|$ vary with t, velocity profiles depend on not only z' but also t.

From the analogy of steady heap flows (section 1.2.5), we found that the flow velocity $v_t(z', h, |\nabla h|)$ decreases almost exponentially with depth z', implying the presence of shear-band structure. The data are fitted by the following function:

$$v_t = v_{t0} \exp\left(-\frac{z'}{h_s}\right), \tag{5.5}$$

where v_{t0} and h_s represent the surface velocity and the characteristic thickness of a clearly fluidised layer, i.e., shear band. The dependence of v_t on h and $|\nabla h|$ does not explicitly appear in equation (5.5). Instead, v_{t0} and h_s should depend on h or $|\nabla h|$.

The fitting by the exponential function (5.5) is shown in the inset of figure 5.5. Despite being able to fit the data around the surface ($z' = 0$) in a good quality, as going deeper, profiles fluctuate and misfit to the exponential curve becomes obvious. This might be caused by the boundary effect as particles are almost trapped at the bottom, i.e., $v_t \approx 0$ at $z' = h$. On the other hand, when h is too small, an exponential profile cannot be distinguished from another functional form such as a linear profile. To avoid these matters in this study, only the upper halves ($z' > h/2$) of the sufficiently thick profile data ($h > 5d$) are used for the exponential fit (5.5). Figure 5.6 shows all of the profiles, where v_t and z' are scaled by v_{t0} and h_s. All of the data are collapsed into a single curve, which supports the validity of the exponential profile (5.5).

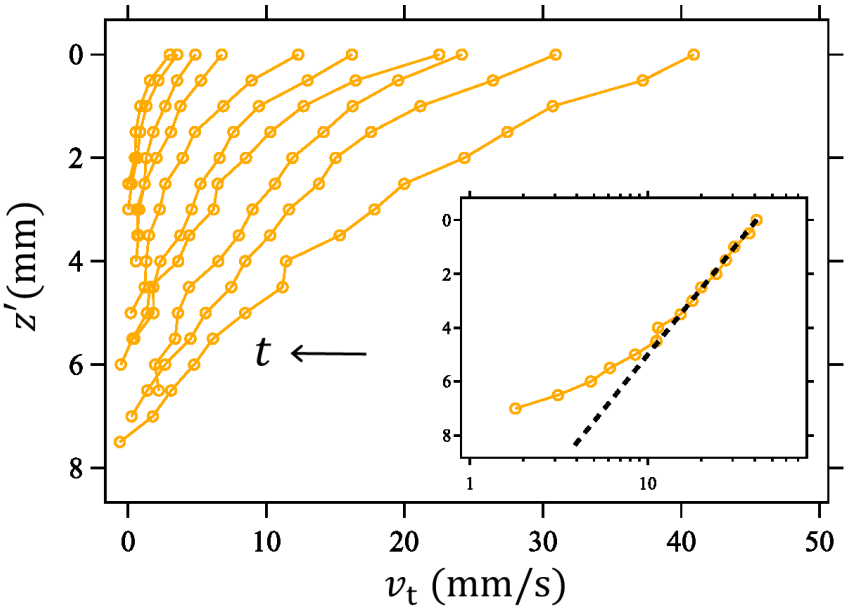

Figure 5.5: Velocity profiles obtained at $r = 20$ mm and various times. The velocity v_t decreases exponentially with depth z'. Inset: Example of the fitting by equation (5.5) in semi-log plot. The data is taken at $t = 0$ s and $r = 20$ mm.

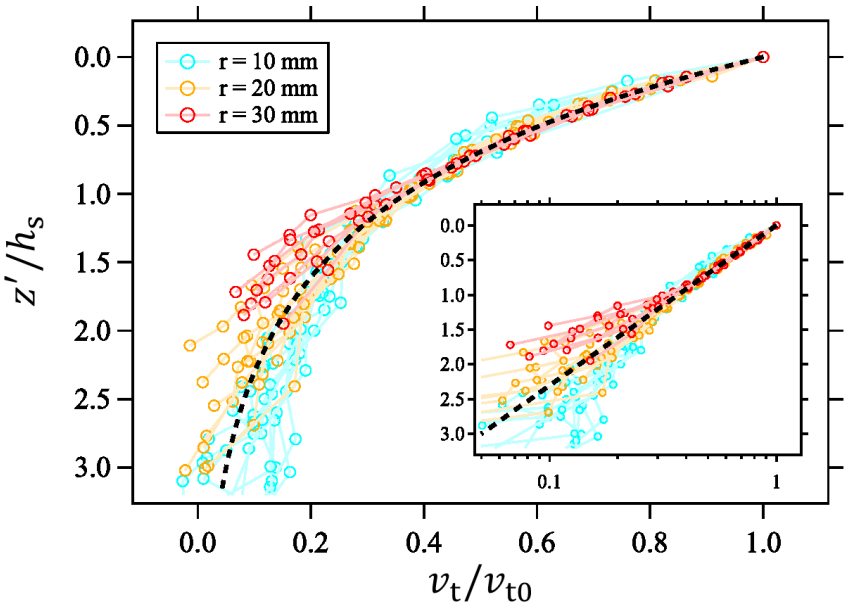

Figure 5.6: All of the scaled velocity profile data, which are collapsed into a single curve: $v_t/v_{t0} = \exp(-z'/h_s)$. The inset shows the same data in semi-log plot.

5.3.2 Packing fraction profile

The profile of packing fraction ϕ is also measured. Raw profiles obtained at $r = 20$ mm and various times are shown in figure 5.7(a). The result implies the following characteristics: ϕ decreases at around the surface layer ($z' = 0$); ϕ is almost constant ($\phi \approx 0.8$) in the middle z' range; and ϕ decreases again as approaching the bottom layer ($z' = h$). Similar features are observed in granular flow down an inclined plane (inset of figure 1.6(c)). To focus on the shear-band region, figure 5.7(b) plots ϕ as a function of scaled depth z'/h_s for all data. Scaled profiles with large h indicate that the region where ϕ decreases roughly corresponds to that where the shear band is created ($z'/h_s < 1$), although profiles with small h (especially data obtained at $r = 30$ mm) do not show this correspondence clearly. However, since fluctuations of ϕ-profiles are rather large, more qualitative discussion using those data might be difficult. In general, the rheological property of granular flow can depend on the packing fraction. Therefore, it is important for future work to investigate the packing fraction profile and also the velocity profile more accurately. To this end, it would be more suitable to time-average the packing fraction and flow velocity measured for a long time using the steady flow such as figure 1.11.

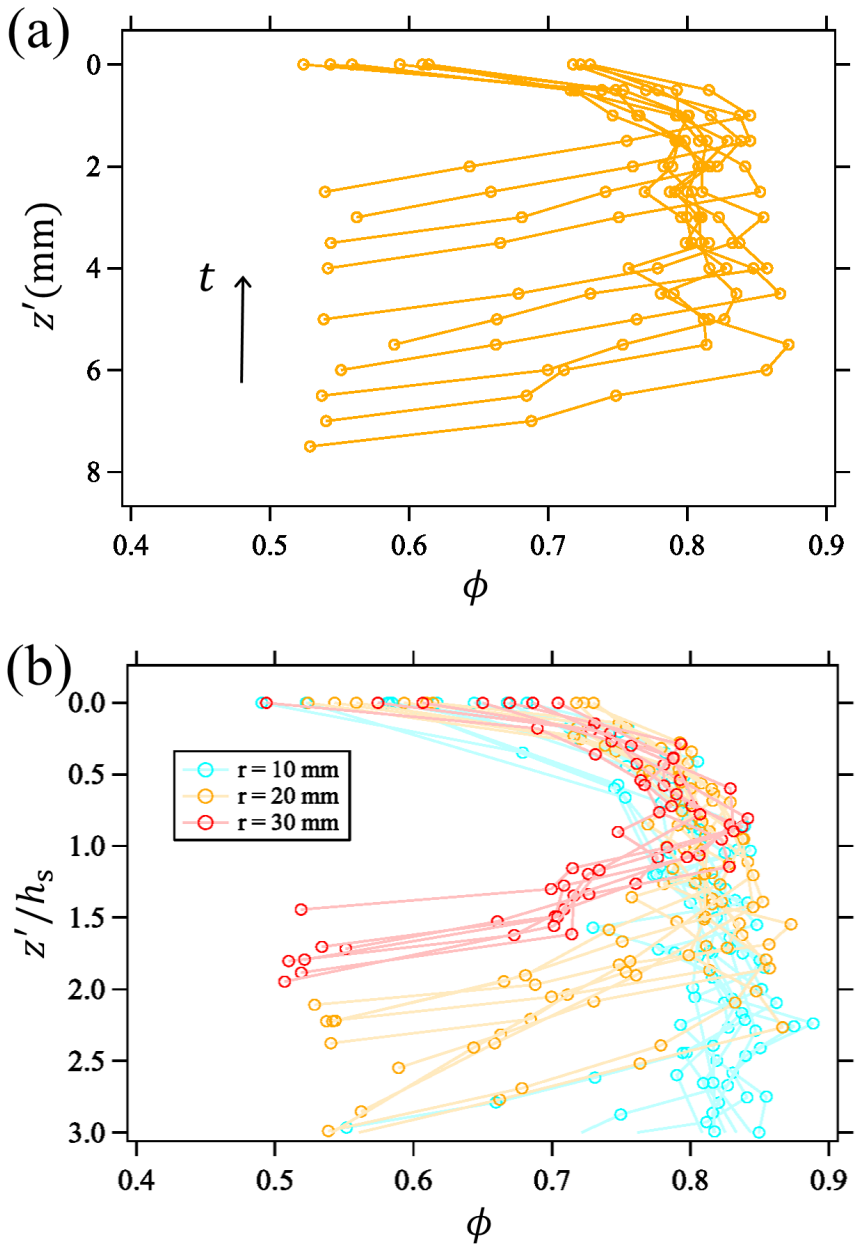

Figure 5.7: Packing fraction ϕ as a function of (a) depth z' and (b) depth scaled by shear-band thickness z'/h_s. The profiles in panel (a) are obtained at $r = 20$ mm, while those in panel (b) are obtained at three analysis positions ($r = 10, 20,$ and 30 mm). The data are measured at the same time as figures 5.5 and 5.6. In the region of shear band ($z'/h_s < 1$), ϕ decreases as approaching the surface ($z' = 0$).

5.3.3 Surface velocity

Next, according to the experimental result (figure 5.8), v_{t0} is a function of $|\nabla h|$, and can be fitted by the NDT model for surface velocity (3.10). Figure 5.8 shows the relation between v_{t0} and $|\nabla h|$ obtained by DEM simulation, where the NDT model for surface velocity (3.10) almost holds, suggesting the consistency with the experimental result. Let us note again that the surface velocity does not depend on the height h. Regarding the energy conversion efficiency, the best fit by the NDT model for surface velocity (3.10) suggests $c_0 = 0.12$, while $c = 0.053$ is estimated for the depth-averaged velocity in the main panel of figure 5.2. Therefore, as expected, the relation between c and c_0 (3.12) is also satisfied.

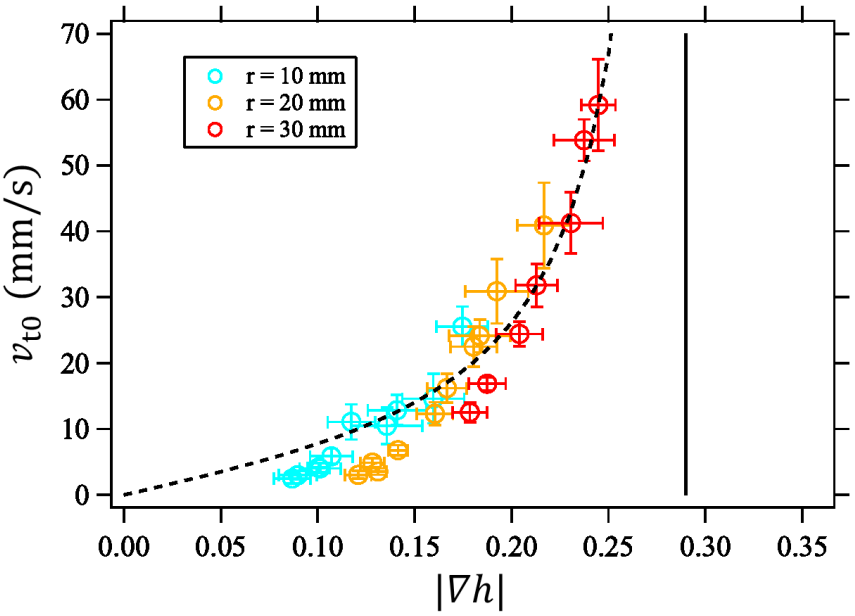

Figure 5.8: Surface velocity v_{t0} versus slope $|\nabla h|$. The data are fitted by the NDT model for surface velocity (3.10), where $c_0 = 0.12$ and $\mu = 0.29$.

5.3.4 Thickness of the shear band

Finally, we discuss how the thickness of the shear band h_s is determined. The relation between h_s and $|\nabla h|$ is shown in figure 5.9, which suggests complex dependence. h_s is a function of not only $|\nabla h|$ but also the analysis position r that can be read by $h(r)$. However, we empirically found that h_s/h is almost scaled by only $|\nabla h|$ as shown in figure 5.10, where a linear dependence can be observed:

$$\frac{h_s}{h} = a|\nabla h|, \tag{5.6}$$

where a is a constant, which is estimated as $a = 2.2$ by means of the least-squares method. This result means that relative thickness of the shear band (h_s/h) increases with the slope $|\nabla h|$. On the other hand, when $|\nabla h|$ is fixed, figures 5.9 and 5.10 suggest that h_s increases with h, but the ratio h_s/h is almost constant independent of h. The inset of figure 5.10 shows the analysis results obtained in various vibration conditions, where h_s/h is little influenced.

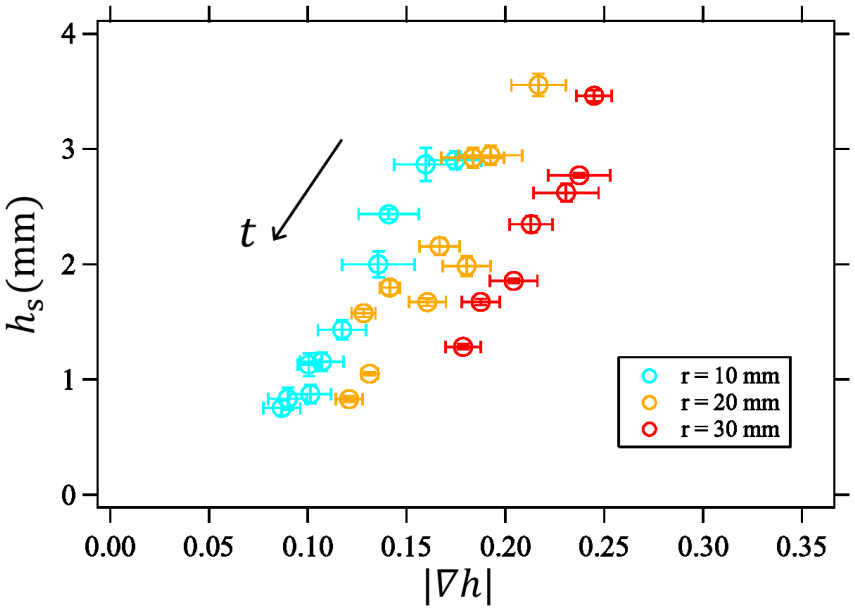

Figure 5.9: Characteristic thickness of the shear band h_s as a function of $|\nabla h|$ for three different analysis positions r. Since the heap relaxes gradually as time goes on, h_s and $|\nabla h|$ decrease with t, following the direction of the arrow.

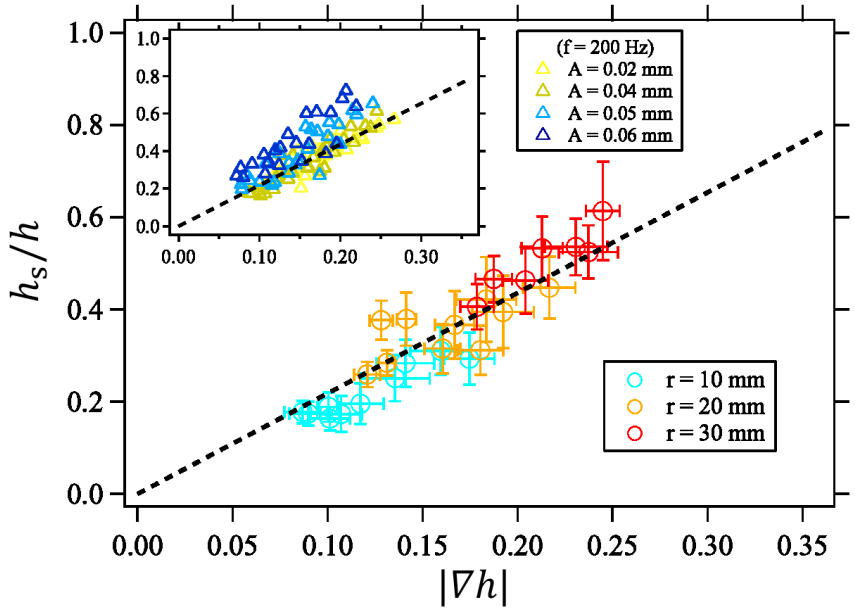

Figure 5.10: Scaled characteristic thickness of the shear band h_s/h as a function of $|\nabla h|$. Inset: Analysis data for various vibration strength. Dash lines show the linear relationship (5.6).

5.4 Dependence on the system size

So far, DEM simulations have consistently reproduced experimental results and given new insights into the internal structure. Using the same numerical method, we finally investigate the dependence on the system size. From the characteristics of the shear-band structure (equation (5.6) and figure 5.10), it can be anticipated that the result is not influenced by the system size R or the ratio R/d. In fact, the NDT model holds with the same value of c when R/d is varied by changing grain diameters ($d = 0.5$ and 1.0 mm) under the fixed system size ($R = 40$ mm) in the experiment. On the contrary, here we expand the understanding of the dependence on the system size by directly changing R.

The same DEM simulations are conducted under a larger plate $R = 80$ mm with grains of $d = 0.5$ mm. The velocity profile $v_t(z')$ is measured at three positions ($r = 20, 40$ and 60 mm) and various time t, and the characteristic thickness of the shear band h_s is estimated for each data as well. The result is shown in figure 5.11(a), which is compared to the data obtained with $R = 40$ mm (same data as figure 5.10). As expected, identical shear-band structure expressed by equation (5.6) can be observed even if we change R or R/d. In addition, as shown in figure 5.11(b), it has been confirmed that the bulk flow property characterised by $\bar{v}_t$ is independent of R or R/d, which is also consistent with the experimental result. The universality of this flow property will be helpful in terms of application.

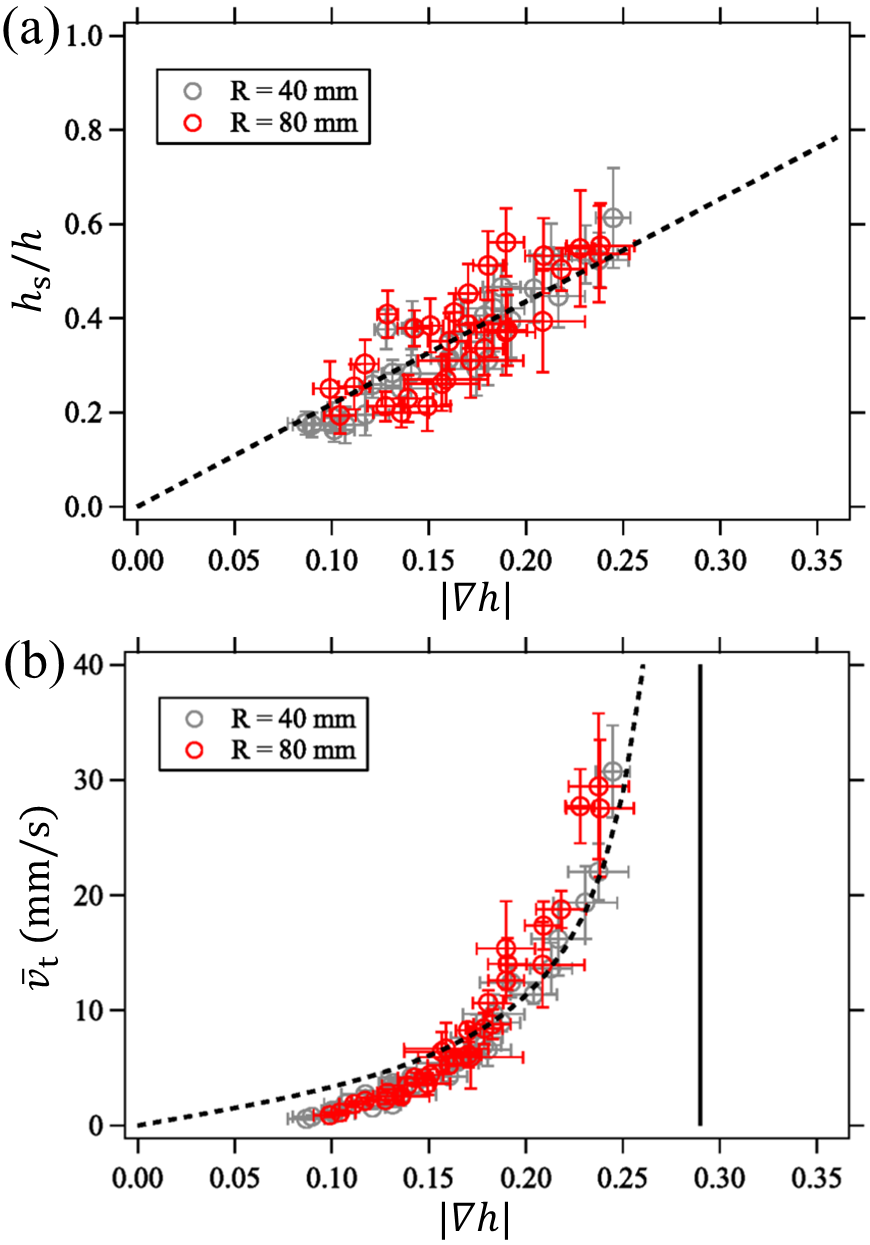

Figure 5.11: Numerical results under different system sizes are shown, which suggests that (a) the internal velocity profile and (b) the bulk flow property do not change. The black curves and lines represent the same ones used in figures 5.2 and 5.10.

6 Discussion

6.1 Bridging the internal velocity profile to depth-averaged velocity

6.1.1 Integration of the velocity profile

First of all, we discuss how the exponential velocity profile revealed by DEM simulation is related to the depth-averaged velocity predicted by the NDT model. In principle, the NDT model should be derived by integrating the velocity profile along the vertical direction. Using the velocity profile (5.5) and the shear-band property (5.6), the depth-averaged velocity $\bar{v}_\mathrm{t}$ can be computed as

$$\begin{aligned} \bar{v}_\mathrm{t} &= \frac{1}{h}\int_0^h v_\mathrm{t}(z')dz' \\ &= \frac{1}{h}\int_0^h v_{\mathrm{t}0}\exp\left(-\frac{z'}{h_\mathrm{s}}\right)dz' \\ &= \chi\left(|\nabla h|\right)\frac{c_0 v_\mathrm{vib}}{\mu^2}\frac{|\nabla h|}{1-(|\nabla h|/\mu)^2}, \end{aligned} \tag{6.1}$$

where

$$\chi\left(|\nabla h|\right) = a|\nabla h|\left\{1-\exp\left(-\frac{1}{a|\nabla h|}\right)\right\}. \tag{6.2}$$

Equations (6.1) and (6.2) are not equal to the NDT model (3.8). However, as mentioned in section 3.4, the NDT model does not hold in smaller $|\nabla h|$ ranges, where the relaxation almost halts leaving finite slopes. In fact, figures 3.3 and 5.2 show that the model curves exhibit misfits to the data as the slopes approach zero. With respect to this reason, it can be speculated that the inertial energy supplied to grains is insufficient to overcome potential barriers of their neighbors in small $|\nabla h|$ ranges (Jaeger et al., 1989; Roering, 2004). On the other hand, this fact suggests that the NDT model is mainly suitable to predict the bulk flow property in a large $|\nabla h|$ range, where non-linearity clearly appears and the relaxation dynamics is practically dominated. We therefore focus on how the function χ (equation (6.2)) behaves in the vicinity of a divergence point ($|\nabla h| \simeq \mu$).

To this end, we introduce a variable $\epsilon = \mu - |\nabla h|$, and equation (6.2) is subjected to

variable conversion:

$$\chi(\epsilon) = a(\mu - \epsilon)\left\{1 - \exp\left(-\frac{1}{a(\mu - \epsilon)}\right)\right\}. \tag{6.3}$$

In order to observe the behavior of this function around $\epsilon \to 0$ ($|\nabla h| \to \mu$), Taylor expansion is conducted as follows:

$$\begin{aligned}\chi(\epsilon) &= a\mu\left\{1 - \exp\left(-\frac{1}{a\mu}\right)\right\} + \\ &\quad \epsilon\left\{\left(a + \frac{1}{\mu}\right)\exp\left(-\frac{1}{a\mu}\right) - a\right\} + o(\epsilon^2) \\ &\sim 0.5 - \epsilon,\end{aligned} \tag{6.4}$$

where $a = 2.2$ and $\mu = 0.29$ are substituted. Therefore, in the limit of $\epsilon \to 0$, which is important for the fitting of the NDT model, equation (6.1) can be read as

$$\bar{v}_t \sim \frac{0.5 c_0 v_{vib}}{\mu^2}\frac{|\nabla h|}{1 - (|\nabla h|/\mu)^2}. \tag{6.5}$$

Since the NDT model (3.8) is identical to equation (6.5) with the relation between c and c_0 (3.12), the NDT model has been consistently reproduced from the integration of the velocity profile obtained by DEM simulation. For small $|\nabla h|$ regimes, c should decrease linearly as shown in figure 5.10 and equation (6.4). However, its effect is rather limited to discuss the practical relaxation of the heap.

6.1.2 Precise description for depth-averaged velocity

We also confirm whether experimental results are consistent with the precise description for the depth-averaged velocity revealed above. In figure 6.1, the data of the depth-averaged velocity $\bar{v}_t$ and slope $|\nabla h|$ are fitted by equation (6.1) with equation (6.2). The value of a for the experimental data cannot be obtained as the internal velocity profile is not accessible. Therefore, only a is left as a fitting parameter, and then the fitting is conducted with $\mu = 0.45$ and $c_0 = 0.12$ determined in section 3. As expected, the whole part of data, including not only large but also small $|\nabla h|$ ranges, can be fitted with more good quality than figure 3.3 using the NDT model.

As an additional test, using $a = 3.6$ determined by the fit in figure 6.1, the time evolution of the profile is reproduced by numerically solving the equation of continuity:

$$\frac{\partial h}{\partial t} = \nabla \cdot \left(h \chi (|\nabla h|) \frac{c_0 v_{\mathrm{vib}}}{\mu^2} \frac{\nabla h}{1 - (|\nabla h|/\mu)^2} \right), \tag{6.6}$$

where $\chi(|\nabla h|)$ is defined by equation (6.2). Numerical results are plotted onto the actual experimental profile in the inset of figure 6.1. Both are in better agreement overall with each other compared to figure 3.7. These results suggest that the characteristic shear band as expressed by equation (5.6) is also created in the experiment as well as the DEM simulation. Note that, however, $a = 3.6$ is relatively large as this value with equation (5.6) implies $h_s/h \approx 1$ at $|\nabla h| = 0.3$, which corresponds to the all-layers-fluidisation assumption. To check the validity of this value, more testing using larger system size or quasi-two-dimensional system are needed.

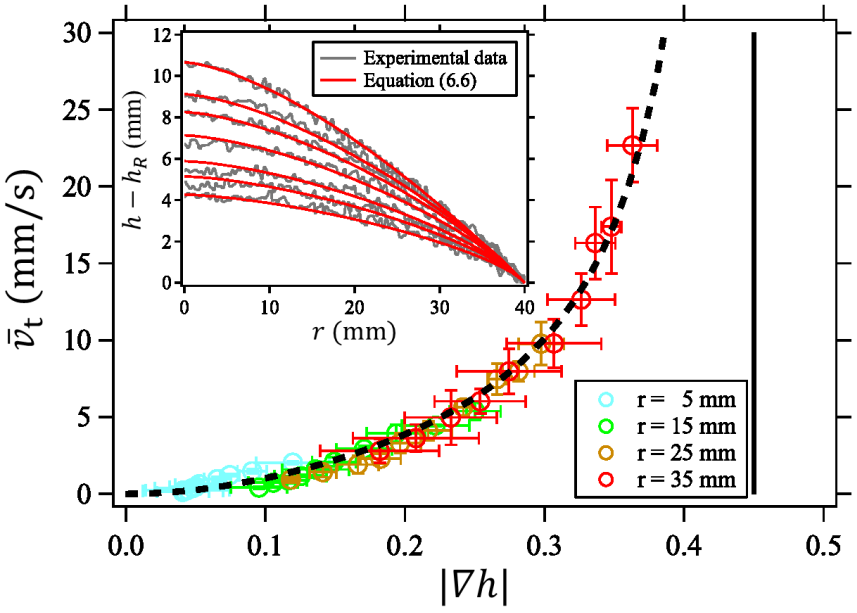

Figure 6.1: The best fit by the precise expression for depth-averaged velocity (6.1) and (6.2). The parameters are $\mu = 0.45$, $c_0 = 0.12$, and $a = 3.6$. Inset: Reproduction of the heap relaxation using the equation of continuity (6.6). The experimental data shown here are the same as figures 3.3 and 3.7.

6.1.3 Consistency with the all-layers-fluidisation assumption

Another remarkable point revealed by DEM simulation is that heap flows create shear-band structure. In other words, clearly fluidised regimes are localised around the surface with thickness h_s, below which creeping flows exhibit. This fact is in contrast to the all-layers-fluidisation assumption used in the derivation of the NDT model as illustrated in Fig. 6.2(a). Actually, however, h_s is proportional to h (equation (5.6)) when $|\nabla h|$ is fixed, which leads to a true image of the flow drawn in figure 6.2(b). Moreover, figures 5.6 and 5.10 imply that the velocity profile is similar at any position and time independent of heap size. This characteristic differs from a conventional shear-band structure with a constant thickness everywhere as observed in heap flows in the absence of vibration (section 1.2.5). Although the detailed pictures of figures 6.2(a) and (b) are different from each other, h determines the fluidised thickness h_s in both cases. This is why $\bar{v}_t = q/h (\propto q/h_s)$ can be described as a function of only $|\nabla h|$, and the NDT model derived on a basis of figure 6.2(a) is still valid for the granular flow consisting of peculiar shear-band structure as shown in figure 6.2(b).

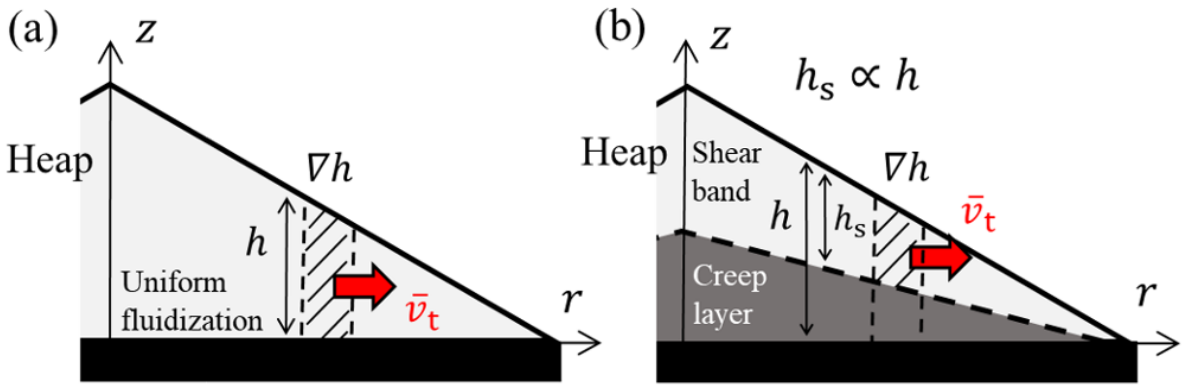

Figure 6.2: Schematic images of (a) the derivation of the NDT model and (b) the h-proportional shear-band structure revealed by DEM simulation.

6.2 Consistency between the NDT model and Roering1999 model

Next, we discuss the consistency between the Roering1999 model (1.54) and the NDT model (3.8):

$$q = \frac{K_d S}{1 - (S/S_c)^2} \tag{1.54}$$

$$\bar{v}_\mathrm{t} = \frac{c v_\mathrm{vib}}{\mu^2} \frac{|\nabla h|}{1 - (|\nabla h|/\mu)^2}, \tag{3.8}$$

where S and $|\nabla h|$ correspond to globally- and locally-measured slopes, respectively. The NDT model proposed in this study is in contrast to the Roering1999 model in terms of the structure of the shear band: the NDT model assumes that the thickness grows proportionally with the height (figure 6.2(b)), whilst the Roering1999 model is based on the shear band with a constant thickness independent of the height (figure 6.3(a)). Note that this difference is not attributed to the dimension of the flow as the NDT model is satisfied in both 2D and 3D cases. To reconcile those two types of shear band, let us consider a heap flow in a steady state using the NDT model.

To create a steady flow under vertical vibration with the NDT model satisfied, the thickness of shear band h_s and the depth-averaged velocity $\bar{v}_\mathrm{t}$ need to depend on position r. This prediction is illustrated in figure 6.3(b). In the following discussion, $r = 0$ and R correspond to the position where grains are injected and where they flow out of the system, respectively. Since the flux q $(= h\bar{v}_\mathrm{t})$ is conserved at any position in a steady state, the slope cannot be constant but larger as approaching the edge of the system (i.e., $r \to R$). The shape of this curved profile can be expressed as follows:

$$\begin{aligned} h(r) &= \frac{q}{\bar{v}_\mathrm{t}} \\ &= \frac{q}{c v_\mathrm{vib}} \frac{\mu^2 - |\nabla h|^2}{|\nabla h|}. \end{aligned} \tag{6.7}$$

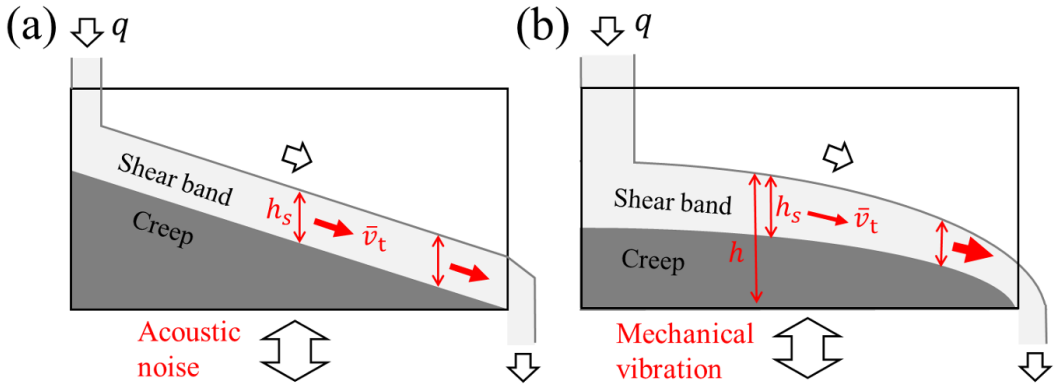

Figure 6.3: Images of a steady heap flow which satisfies (a) the Roering1999 model and (b) the NDT model. The primary difference is that the former considers conventional shear band with a constant thickness, while the latter assumes that the thickness grows proportionally with the height.

Solving this partial differential equation yields the following solution:

$$\begin{aligned} r &= R - \frac{cv_{\mathrm{vib}}}{4q\mu^2}h\left\{h + \sqrt{\left(\frac{2q\mu}{cv_{\mathrm{vib}}}\right)^2 + h^2}\right\} + \frac{q}{cv_{\mathrm{vib}}}\ln\left[\frac{cv_{\mathrm{vib}}}{2q\mu}\left\{-h + \sqrt{\left(\frac{2q\mu}{cv_{\mathrm{vib}}}\right)^2 + h^2}\right\}\right] \\ &= \xi(h), \end{aligned} \tag{6.8}$$

where the boundary condition is set as $h = 0$ at $r = R$ for simplicity (see Appendix E for the derivation). Defining ξ^{-1} as the inverse function of ξ, we can obtain

$$h = \xi^{-1}(r). \tag{6.9}$$

Using equation (6.9), we can predict a surface profile of a heap flow in a steady state for a given flux q and vibration velocity v_{vib}. Figure 6.4 shows a profile for $q = 100$ mm^2/s and $v_{\mathrm{vib}} = 47$ mm/s ($\Gamma = 6$ with $f = 200$ Hz), where the system size is set $R = 600$ mm, which is the same as the experiment of Roering et al. (2001). Here Material 1 in table 2.1 ($\mu = 0.45$) is assumed. The area filled in grey represents the predicted region where shear band is created, which is calculated by equation (5.6) with $a = 3.6$. Note that the profile at around $r = R$ shows unrealistic negative values due to the simplification of the boundary condition. Interestingly, the profile looks almost linear particularly in the middle r-range, where the thickness of shear band is approximately constant as well. This

is consistent with the experimental observation of Roering et al. (1999) (section 1.3.3). In addition, the same data trend as figure 1.11 can be reproduced using equation (6.9). Let the global slope S be $\{h(0) - h(R)\}/R$. Figure 6.4 plots S calculated for various q. A similar nonlinear relation to figure 1.11 is observed. These data can also be well fitted by the Roering1999 model (1.54) using two free fitting parameters K_d and S_c, which is drawn in red.

From these results, it would be possible to understand the difference between the Roering1999 model and the NDT model as follows. Roering et al. (2001) focus on only a linear regime in the middle r-range, and compare global slope S with flux q. Since q can be simply calculated from the flowing volume of grains, we do not need to consider the detail of shear-band structure. Because of this simplification, however, two variable fitting parameters K_d and S_c are needed to fit the data. On the other hand, in this study, the transport property of grains is more locally analysed. We measure local slope $|\nabla h|$ and then compare them with depth-averaged velocity $\bar{v}_t$, not flux q. Although calculating $\bar{v}_t$ requires us to take the height or the shear band into consideration, the NDT model needs only constant fitting parameters c and μ.

Each model has their own advantage. The Roering1999 model is useful particularly when the situation is complex as in nature and flow properties are difficult to measure. Once two fitting parameters K_d and S_c are set, the observed data might be practically characterised. In fact, the Roering1999 model has been employed for the crater relaxation model introduced in section 1.3.4. In contrast, the NDT model will work well when the transport property can be accurately measured. Additionally, compared to K_d, a fitting parameter c gives us more clear information on how much energy is transmitted from the source of disturbance to the horizontal transport causing the heap relation.

We should also note that Roering et al. (2001) used random acoustic noise to agitate grains, which differs from mechanical vibration used in this study. Therefore, energy transmission process must be different from each other, which could affect the transport property. Additionally, the level of vibration strength in this study could be significantly different from Roering et al. (2001). Let us compare the transport coefficient K_d of this study and Roering et al. (2001). In this study, the best fit in figure 6.4 shows K_d =

1.0×10^3 mm^2/s, which can be interpreted as $K_d \sim 10^1$ g cm^{-1} s^{-1}, assuming $\rho = 2.6$ g/cm^3 and $\phi = 0.5$. This value is obviously larger than $K_d = 0.77$ g cm^{-1} s^{-1} as in figure 1.11(c). This comparison also suggests that the vibration acceleration in the experiment by Roering et al. (2001) could be partially lower than Γ_c. If that is the case, the dynamics of the flow could be fundamentally different. To confirm these points, it is desired in the future study to experimentally create a steady heap flow under mechanical vibration and directly confirm whether the discussion above is correct.

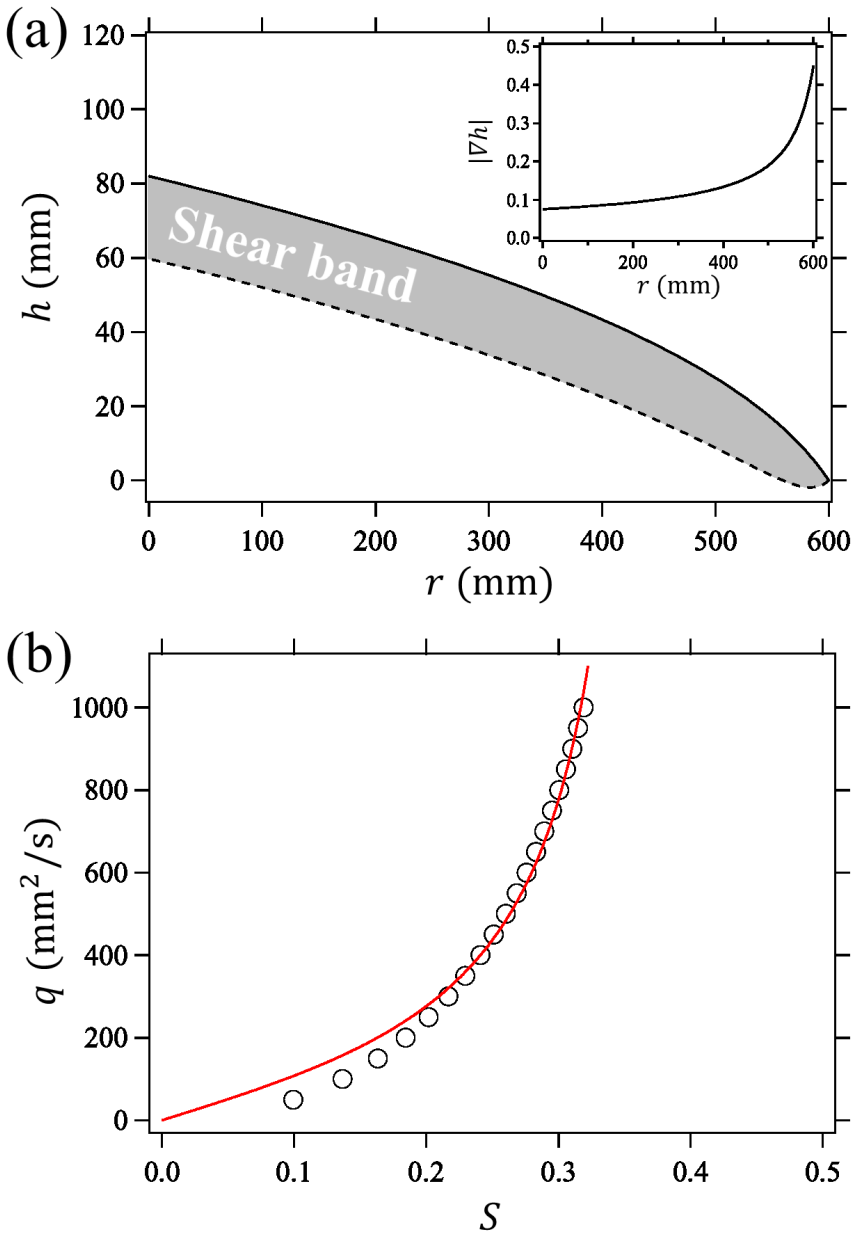

Figure 6.4: (a) Predicted steady profile based on equation (6.9). Material 1 in table 2.1 ($\mu = 0.45$) is assumed for granular material, and the flux and vibration conditions are set as $q = 100$ mm^2/s and $v_{\mathrm{vib}} = 47$ mm/s. The shear-band region filled in grey is calculated by equation (5.6) with $a = 3.6$. Note that the profile at around $r = R$ shows unrealistic negative values due to the simplification of the boundary condition $h(R) = 0$. Inset: Local slope calculated by the differentiation of the profile. (b) Predicted global slope S calculated for various flux q. Vibration conditions are the same as panel (a). A red curve shows the best fit by the Roering1999 model (1.54). The fitting parameters are $K_d = 1.0 \times 10^3$ mm^2/s and $S_c = 0.38$.

6.3 Energy conservation law

When the NDT model is derived, we assume that a flow is quasi-steady for simplicity. In other words, unlike the Navier-Stokes equation as in fluid mechanics, the NDT model cannot predict the time evolution of acceleration as the inputted energy always balances the dissipation energy of friction and pressure gradient. In reality, however, there should be a period when a granular bed gradually accelerates until reaching a steady state. For instance, granular media begin to move right after turning on a vibrator, whereas the NDT model cannot describe this process unfortunately.

In addition, the derivation of the NDT model assumes an asymmetric random walk process, i.e., energy is repeatedly supplied along a random direction. The average of the velocities along plus and minus directions corresponds to the NDT model (3.8) (section 3.2). If the description of this random walk is correct, the velocity can be temporarily negative. However, the transport velocity predicted by the NDT model is always positive.

To solve these two problems, we consider the transport of the granular slice (figure 3.2) based on the energy conservation law. Through this discussion, the physical meaning of the c value can be more clarified. In the following, the sliding-block approximation is used again, and the internal structure is ignored.

Firstly, we assume that the kinetic energy of the granular slice E evolves based on the energy conservation law:

$$\frac{\partial E(t)}{\partial t} = \Omega\left(T_c\right) cmgv_{\mathrm{vib}} - \left\{\mu mg - mg|\nabla h| \operatorname{sgn}\left(v_{\mathrm{t}}\right)\right\} v_{\mathrm{t}}, \tag{6.10}$$

where v_{t} is (not averaged) transport velocity, and $\Omega\left(T_c\right)$ is a random walk variable replaced by $+1$ and -1 by turn at intervals of random-walk cycle T_c. To allow E to be negative and consider the motion along the negative direction, E is defined as follows:

$$E = \operatorname{sgn}\left(v_{\mathrm{t}}\right) \frac{1}{2} m v_{\mathrm{t}}^2. \tag{6.11}$$

Namely, when the granular slice move to the minus direction, the kinetic energy E be-

comes negative. To recover the transport velocity v_t from the kinetic energy E, we use

$$v_\mathrm{t} = \mathrm{sgn}\,(E)\ \sqrt{|E|}. \tag{6.12}$$

For simplicity, the energy conservation law (6.10) is divided by m:

$$\frac{\partial E'(t)}{\partial t} = \Omega\,(T_c)\,cgv_\mathrm{vib} - \{\,\mu g - g|\nabla h|\,\mathrm{sgn}\,(v_\mathrm{t})\,\}\,v_\mathrm{t}, \tag{6.13}$$

where

$$E' = \frac{E}{m}. \tag{6.14}$$

Next, the NDT model is reproduced by numerically solving equation (6.13). Using A and f^{-1} as unit length and time, the energy conservation law (6.10) is nondimensionalised:

$$\frac{\Gamma}{(2\pi)^2}\,\frac{\partial \hat{E}'(\hat{t})}{\partial \hat{t}} = \Omega\,(\hat{T}_c)\,2\pi c - \{\,\mu - |\nabla h|\,\mathrm{sgn}\,(\hat{v}_\mathrm{t})\,\}\,\hat{v}_\mathrm{t}. \tag{6.15}$$

The important point when solving this nondimensional energy conservation law is how random-walk cycle $\hat{T}_c$ is determined. The most natural assumption is

$$\hat{T}_c = 1, \tag{6.16}$$

which implies that an impulsive force from the vibrating disk to the granular layer is applied in every vibration cycle. DEM simulations can directly give a constrain on this expectation. The time evolution of the total force applied on the bottom particles F_b is shown in figure 6.5, which is consistent with the random-walk cycle (6.16).

Applying the above random-walk cycle, the time evolution of transport velocity v_t is obtained by numerically solving the nondimensional energy conservation law (6.15) with the random-walk cycle (6.16). Figure 6.6(a) shows the result for a fixed slope $|\nabla h| = 0.2$ and various vibration conditions. Random walk behaviour, which results from a random walk variable $\Omega\,(\hat{T}_c)$, can be observed. On the other hand, the black dashed line represents

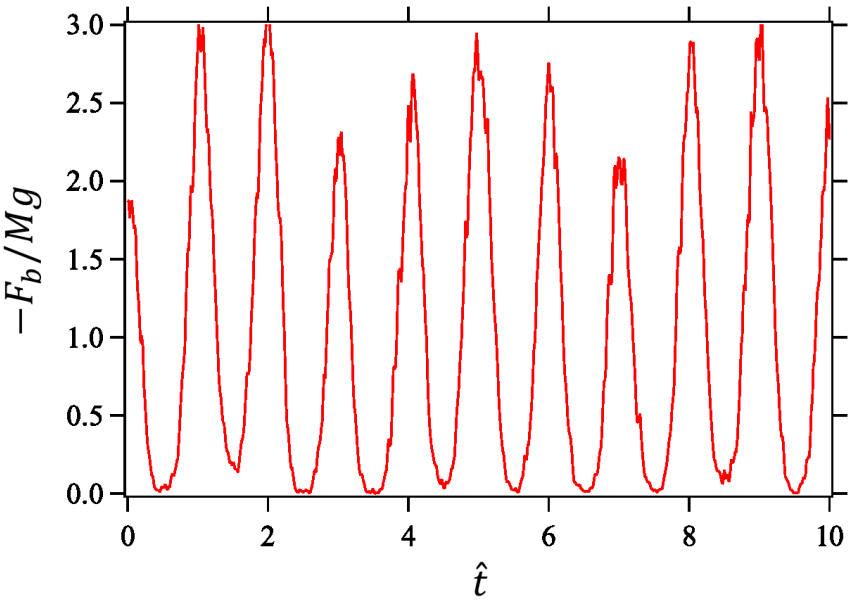

Figure 6.5: Total force applied on the bottom particles F_b as a function of time $\hat{t}$. To observe the data at the same level, F_b is scaled by Mg. Note that this result is obtained from one simulation run.

the average transport velocity calculated by the nondimensional NDT model:

$$\hat{\bar{v}}_{\mathrm{t}} = \frac{2\pi c}{\mu^2} \frac{|\nabla h|}{1 - (|\nabla h|/\mu)^2}, \tag{6.17}$$

where the dependence on vibration conditions does not appear. According to the derivation process of the NDT model (section 3.2), $\hat{\bar{v}}_{\mathrm{t}}$ corresponds to the average of two extreme velocities $\hat{v}_+$ and $\hat{v}_-$ drawn by two grey dashed lines in figure 6.6(a), which are expressed as

$$\hat{v}_+ = \frac{2\pi c}{\mu - |\nabla h|}, \tag{6.18}$$

$$\hat{v}_- = -\frac{2\pi c}{\mu + |\nabla h|}. \tag{6.19}$$

During every random-walk cycle (6.16), the transport velocity v_{t} oscillates between these two velocities $\hat{v}_+$ and $\hat{v}_-$, which means that the NDT model (6.17) gives a good approximation to the average transport velocity. We have also confirmed that the average of velocity fluctuation is almost consistent with the NDT model even if $\Omega(\hat{T}_c)$ is replaced by

+1 and −1 not by turns but random.

However, this consistency breaks as increasing the slope $|\nabla h|$. Figure 6.6(b) shows the numerical solution obtained for a fixed vibration condition and various slopes. Although the average of v_t with small $|\nabla h|$ seems consistent with the NDT model, considerable disagreement is observed between the NDT model and the average of v_t with large $|\nabla h|$. This result suggests that it takes more time to achieve the extreme velocity when the slope is larger. In fact, when $|\nabla h| = 0.1, 0.2, 0.3, 0.4$ with $\Gamma = 6$, it takes $\hat{T} \approx 0.72, 1.4, 4.0, 35$ respectively to achieve $\hat{v} = 0.9\hat{v}_+$ from $\hat{v} = 0$. If real grains actually behave following this random walk model, this discussion should also be related to the genuine value of the energy conversion efficiency c. In any case, to confirm the accuracy of the random walk model in the future, it might be more suitable to investigate a granular flow keeping a fixed slope, such as the one introduced in section 1.2.4.

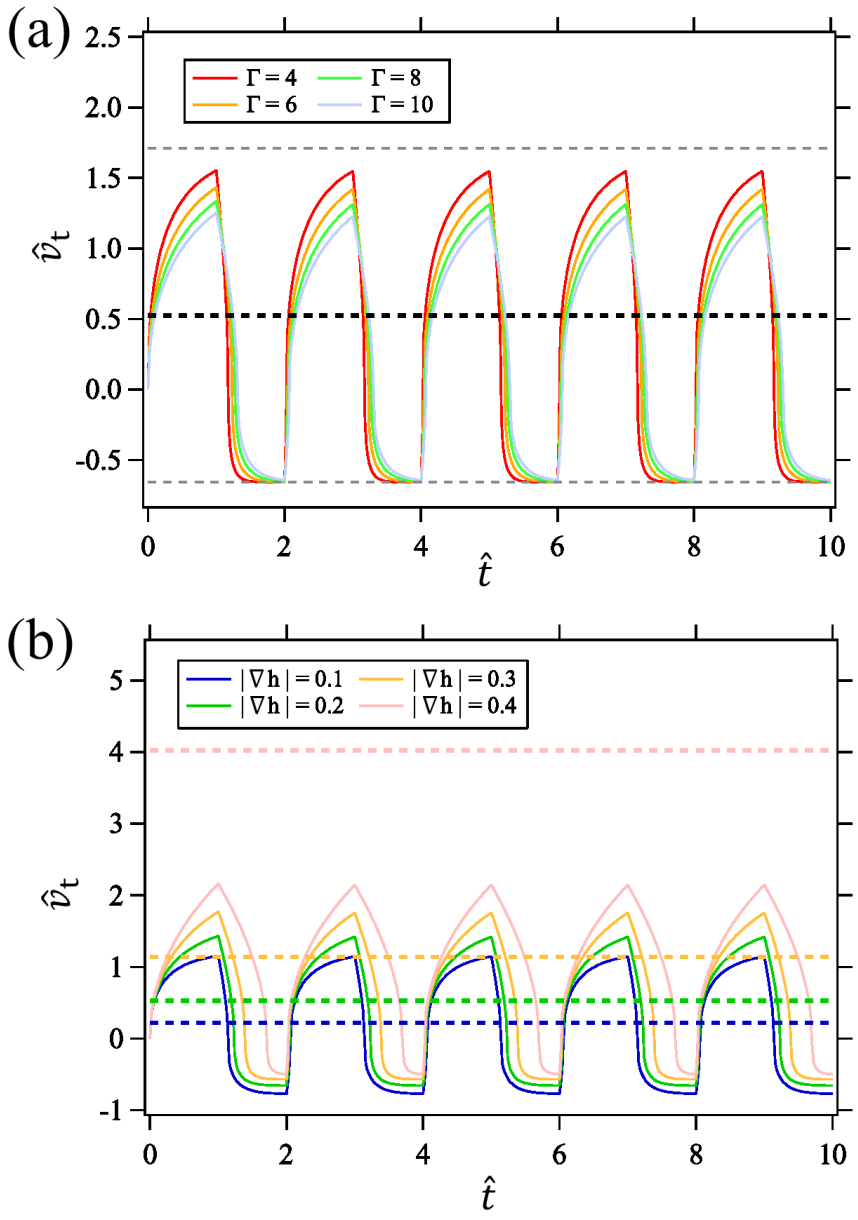

Figure 6.6: Time evolution of the transport velocity $\hat{v}_t$ calculated by numerically solving the nondimensional energy conservation law (6.15) with the random-walk cycle (6.16). In panel (a) a slope is fixed at $|\nabla h| = 0.2$ and vibration conditions are varied, while in panel (b) vibration conditions are fixed ($\Gamma = 6$) and slopes are varied. Colours represent vibration conditions in panel (a) and slopes in panel (b), respectively. Thick dashed lines in panels (a) and (b) indicate the average transport velocity calculated by the NDT model (6.17), while thin dashed lines in panel (a) correspond to two extreme velocities $\hat{v}_+$ (6.18) and $\hat{v}_-$ (6.19).

6.4 Application of the NDT model

Next, we show a simple application of the NDT model toward the crater relaxation process caused by impact-induced seismic shaking (figure 1.13). Let us consider the crater erasure by a meteorite impact with diameter 4 m onto asteroid Itokawa. By this impact, the entire surface of Itokawa is shaken with $\Gamma > 1$ (Yamada et al., 2016). The detailed condition of this seismic vibration can be estimated as follows.

To predict the Γ value of impact-induced global seismic event on asteroid Itokawa as a function of the time elapsed after the impact t and impactor diameter $D_{\rm imp}$, the following model has been proposed (Richardson Jr. et al., 2005; Miyamoto et al., 2007; Yamada et al., 2016):

$$\Gamma(t, D_{\rm imp}) = \frac{3 f_{\rm seis} v_{\rm imp}}{G} \sqrt{\eta \frac{\rho_{\rm imp} {D_{\rm imp}}^3}{{\rho_{\rm ito}}^3 {D_{\rm ito}}^5}} \exp\left(-\frac{2\pi f_{\rm seis}}{Q} t\right), \tag{6.20}$$

where what each symbol means is summarised in table 6.1. The exponential term in equation (6.20) indicates the attenuation of the seismic energy due to the inelasticity of the internal structure of an asteroid. From the definition of Γ, the maximum vibration velocity $v_{\rm vib}$ can be written as:

$$\begin{aligned} v_{\rm vib}(t, D_{\rm imp}) &= \frac{\Gamma g_{\rm ito}}{2\pi f_{\rm seis}} \\ &= \frac{3 g_{\rm ito} v_{\rm imp}}{2\pi G} \sqrt{\eta \frac{\rho_{\rm imp} {D_{\rm imp}}^3}{{\rho_{\rm ito}}^3 {D_{\rm ito}}^5}} \exp\left(-\frac{2\pi f_{\rm seis}}{Q} t\right). \end{aligned} \tag{6.21}$$

Substituting specific parameter values shown in table 6.1 into equation (6.21), $v_{\rm vib}(t, 4\ {\rm m})$ is quantitatively expressed as

$$v_{\rm vib}(t, 4\ {\rm m}) = 5.7 \times 10^{-2} \exp\left(-\frac{2\pi f_{\rm seis}}{Q} t\right)\ [{\rm m/s}]. \tag{6.22}$$

From this relation, the typical vibration velocity can be given as $V_{\rm seis} \sim 10^{-2}$ m/s. For the typical vibration duration, we employ $T_{\rm seis} = Q/(2\pi f_{\rm seis}) \sim 10^1$ s, which corresponds to the time at which the vibration velocity attenuates by a factor of $1/e$.

Getting the discussion back to the crater relaxation, the crater with diameter $D_{\rm cra}$ and depth $H_{\rm cra}$ is erased when the mass of granular flows exceeds the crater volume. The order

Table 6.1: Parameter values used in equation (6.20), which are cited from Yamada et al. (2016).

Parameter	Typical value	Note
$\rho_{\rm ito}$	1900 kg m^{-3}	Density of Itokawa
$\rho_{\rm imp}$	2500 kg m^{-3}	Density of impactor
$D_{\rm ito}$	400 m	Diameter of Itolawa
$v_{\rm imp}$	5300 m s^{-1}	Mean velocity of meteorite impacts
$f_{\rm seis}$	20 Hz	Dominant frequency of impact-induced seismic waves on Itokawa
η	10^{-4}	Seismic efficiency: conversion rate from impactor's kinetic energy into seismic energy
Q	2000	Seismic quality factor: inverse of attenuation rate of seismic energy density
$g_{\rm ito}$	10^{-4} m s^{-2}	Itokawa's surface gravity
G	6.7×10^{-11} m^3 kg^{-1} s^{-2}	Gravitational constant

estimate of this mass balance is expressed as

$$\bar{v}_{\rm t} H_{\rm cra} D_{\rm cra} T_{\rm seis} \sim D_{\rm cra}^2 H_{\rm cra}, \tag{6.23}$$

where the left- and right- hand sides represent the the mass of granular flows driven by a single impact and the volume of a crater, respectively. By neglecting the nonlinear term in the NDT model (3.8) which is important only for steep slopes, the above mass balance leads to

$$D_{\rm cra} \sim c V_{\rm seis} \mu^{-2} |\nabla H| T_{\rm seis}. \tag{6.24}$$

The typical μ value on asteroid Itokawa is $\tan 35^\circ$ (Fujiwara et al., 2006) and $|\nabla H| \sim H/D \sim 10^{-1}$ (Hirata et al., 2009; Katsuragi, 2016), and the value of c does not depend on the system size (section 5.4). Substituting the specific parameter values into equation (6.24), the maximum crater diameter erased by this impact-induced shaking is estimated as $D_{\rm cra} \sim 10^{-3}$ m. This value is comparable with actual grain (regolith) size (Fujiwara et al., 2006), which means that the the accumulation of multiple impacts is needed to

erase large craters. The above discussion is the first attempt to apply the physical model for granular flow to the crater relaxation process, although more careful computation as in Yamada et al. (2016) is necessary to estimate the relaxation timescale more precisely.

Note that the global seismic shaking cannot be accomplished on larger planets (e.g., Moon and Mars) (Yamada et al., 2016). Even on such a planet, however, the shape of craters exhibits relaxation, and its reason could be due to the local seismic shaking where seismic waves propagate not globally but locally (Fassett and Thomson, 2014). One possible approach to model crater relaxation by a local seismic event is deriving a scaling law which describes vibration velocity as a function of impactor's size and distance from the impact site (e.g., Teanby, 2015; Tsuji and Teanby, 2016), and then implementing it into the NDT model.

As for another possible application, sediment transport from soil-mantled hillslopes on the Earth could be considered. The relation between sediment flux and hillslope gradient exhibits nonlinearity like the NDT model. In other words, the flux increases divergently as the slope approaches a certain critical slope, which is reported by field observations (Roering et al., 1999) and field measurements (Gabet, 2003), where environmental disturbance (e.g., earthquakes, rainsplash and biogenic activity) is thought to mobilise soil particles. As partly introduced in section 1.3.3, this natural process has been mimicked by granular flows with acoustic noise in laboratory experiments (Roering et al., 2001; Roering, 2004; Furbish et al., 2008); with random perturbation in DEM simulations (Ben-Dror and Goren, 2018; Ferdowsi et al., 2018). Although those applied perturbation types are different from mechanically-controlled vibration used in our study, similar nonlinear transport properties are reported. Therefore, it can be speculated that the framework of our modelling for heap flows in the presence of vibration will be potentially applicable to various situations with different disturbance types.

Despite such plentiful applicability, we should always keep in mind that natural granular flows can be different from ideal granular flows we have discussed. When applying the model from a physical point of view, numerous complex factors in nature (e.g., cohesion and boundary condition) need to be carefully considered (Jerolmack and Daniels, 2019).

6.5 Limitation and future work

Finally, important open questions, which would significantly contribute to the development of granular physics if addressed, are presented here.

- **Which vibration range can the NDT model be applied in?**
  This study focuses on the vibration conditions of v_{vib} = 10–200 mm/s and Γ = 2–10. When increasing the vibration strength above this range, the transition into a granular-gas phase (section 1.1.4) will occur, where the NDT model is no longer suitable. Conversely, as approaching a critical fluidisation condition $\Gamma = \Gamma_c$, the NDT model will break down at some point, where the characteristic shear band drawn in figure 6.2(b) will not be created. The critical conditions to distinguish these multiple regimes need to be investigated.

- **What underlying nature determines the energy conversion efficiency c?**
  Since the value of c is much less than 1, most of the inputted energy is not used for the bulk granular transport. One might notice that the modelling in this study completely neglects the contribution of velocity fluctuation, which can be another consumption source of the inputted energy. According to a kinetic theory for dense fluidised flows (e.g., Jenkins and Berzi, 2012), granular temperature affects the transport velocity in general. It is also not clear whether the condition of bottom particles influences the bulk flow property. In any case, to understand the origin of the c value, it might be necessary to fully evaluate the energy partition among dissipation (inelasticity and friction), random motion (granular temperature), and collective motion (mean flow determining the value of c).

- **Why does the fluidised layer create the height-proportional shear band?**
  The structure of the shear band that this study have revealed is obviously different from the conventional understanding that grains flow holding a constant fluidised thickness. Since the driving force of granular flow is not gravity but vibration, the mobility of particles should be determined by how much kinetic energy particles receive at each position. Therefore, the energy propagation process from the vibrating bottom layer, including the boundary condition to be satisfied (e.g., Richman,

1993), needs to be considered to more theoretically understand this issue.

- **How can the NDT model be related to the existing rheological model?**
  The bulk frictional coefficient μ, which is defined as the ratio of the shear stress to the pressure, is assumed to be constant for the sake of simplicity. Meanwhile, as introduced in section 1.3.2, the dependence of μ on vibration conditions under horizontal vibration has been investigated. Using such a complicated frictional model, one might speculate that the dynamics of heap flows under vibration could be discussed on the analogy of local rheology. If we can associate the NDT model with such an existing model in some way, the understanding of the modelling will be dramatically improved.

7 Conclusion

This thesis has investigated dense granular-heap flows under vertical vibration. Our main focus is cast particularly at transient states where morphological structure of a granular bed always evolves, which has been relatively little studied so far despite the importance in geophysical application. As a result, we have revealed various new aspects of granular flows through the extensive analysis involving experimental, numerical, and theoretical approaches. Our main achievement can be digested as follows.

Laboratory experiments have been conducted to observe the relaxation dynamics of a granular heap on a vertically vibrating plate. Using a high-speed laser profiler, the time evolution of the surface profile of a relaxing heap was measured. Vibration conditions and type of granular materials were also systematically changed.

To explain the experimental result, the nonlinear diffusion transport (NDT) model has been proposed based on Roering et al. (1999, 2001), which can describe the depth-averaged transport velocity of granular flows as a function of slope. Implementing the NDT model into the equation of continuity, the relaxation profile have been successfully reproduced. In this model, we introduce the energy conversion efficiency from vertical vibration into horizontal granular transport. Comparison of the data in various conditions yields that the energy conversion efficiency can be considered a universal constant and the value is ~ 0.068. This result suggests that only less than 10% of the inputted vibration energy is used for the granular transport. We have also confirmed that the NDT model holds for the surface velocity as well, and its energy conversion efficiency is almost twice as large as the one of the depth-averaged velocity.

To reproduce the laboratory experiment and perform in-depth analyses, a numerical code using Discrete Element Method (DEM) has been developed. Numerical results satisfy the NDT model as well, and are not sensitive to microscopic mechanical parameters in DEM simulation, which supports the universality of the NDT model. Using the numerical data, we have investigated the internal velocity profile which was difficult to access by experiment. It has been revealed that the flow velocity exponentially decays with depth from the surface. Moreover, it turned out that the characteristic thickness of the clearly fluidised region (i.e., shear band) grows proportionally with the height. Since this shear-

band structure is obviously different from a conventional understanding, this result must give a new insight into the property of granular-heap flows in a vibrating system.

By mutually complementary analyses of both experimental and numerical results, we have extended the understanding of heap-flow properties. Specifically, we have proved that the integration of the internal velocity profile is consistent with the depth-averaged velocity predicted by the NDT model. Furthermore, assuming a steady heap flow with the NDT model satisfied, we theoretically drew a surface profile in a steady state, which consistently captures the main feature of previous experiments by Roering et al. (2001). Finally, to propose a way of application, the NDT model is implemented into crater relaxation dynamics on asteroid Itokawa, which is actively discussed in planetary science. The theoretical prediction based on the NDT model suggests that the accumulation of multiple impact events is necessary to erase the whole structure of a crater.

Lastly, despite these progresses, as implied in introduction, the establishment of a comprehensively applicable model is challenging. In fact, there are still a number of issues to be considered even within this research subject. However, I believe that results presented here shed light on a new rheological property of granular media. It is hoped that this thesis attracts the interest of not only granular physics community but also other research area, and then helps to develop a new theory in the future.

Appendix A Measurement of flux

The measurement method of the flux described as equation (3.1) can be generally derived from the mass conservation law in a cylindrical coordinate system:

$$\frac{\partial \rho_\phi}{\partial t} + \nabla \cdot (\rho_\phi \mathbf{v}) = 0, \tag{A.1}$$

where ρ_ϕ and $\mathbf{v} = (v_r, v_\theta, v_z)$ represent the bulk density and flow velocity, respectively. Assuming incompressibility of the whole heap, the geometrical configuration of the experimental system (figure A.1(a)) is expressed by the density distribution:

$$\rho_\phi = \begin{cases} \text{const. } (>0) & | \quad \text{if } 0 \le r \le r_0, 0 \le \theta < 2\pi, 0 \le z \le h(r,\theta) \\ 0 & | \quad \text{otherwise.} \end{cases} \tag{A.2}$$

Note that the height of a heap $h(r,\theta)$ is measured from $z = 0$. Then, equation (A.1) is integrated with equation (A.2) along the z direction:

$$\frac{\partial h}{\partial t} + \frac{1}{r}\frac{\partial}{\partial r}(r q_r) + \frac{1}{r}\frac{\partial}{\partial \theta}(q_\theta) = 0, \tag{A.3}$$

where $\mathbf{q} = (q_r, q_\theta, 0)$ is the flux defined as the volume flowing across unit length per unit time:

$$q_r = \int_0^h v_r \, dz \qquad \text{and} \qquad q_\theta = \int_0^h v_\theta \, dz. \tag{A.4}$$

According to the experimental observations, the heap is relaxed axisymmetrically, which suggests that grains flow mostly along the r direction and the flow along the θ direction is negligible, i.e., $q_r \gg q_\theta$ or $h(r,\theta) \simeq h(r)$. Therefore, equation (A.3) is reduced to:

$$\frac{\partial h}{\partial t} + \frac{1}{r}\frac{\partial}{\partial r}(r q) = 0, \tag{A.5}$$

where $q = |\mathbf{q}| \simeq q_r$. This approximation allows us to simplify the relaxation dynamics using a collection of flowing annular slices as discussed in section 3.2.

The mass (volume) conservation holds within each annular slice with thickness dr as

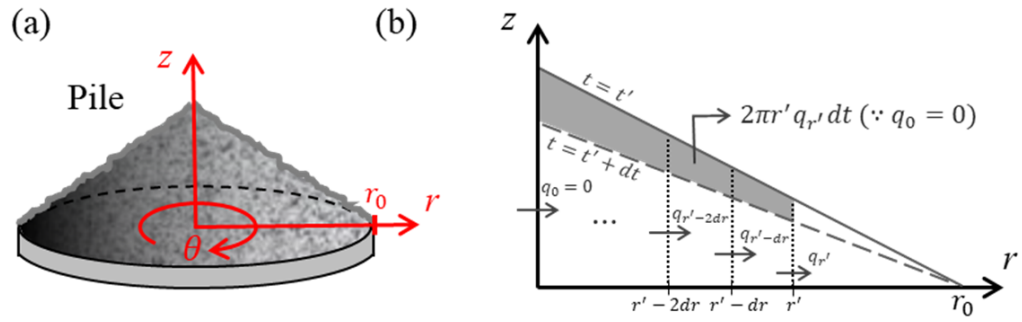

Figure A.1: (a) Experimental system: r, θ, and z are radial, angular, and height coordinates, respectively. (b) Image of equation (A.6). Solid and dashed lines represent profiles at $t = t'$ and $t' + dt$, respectively. From the conservation law, $2\pi r q_{r'} dt$ corresponds to the volume of granular media flowing at position r' (highlighted in grey). Cited from Supplemental Material of Tsuji et al. (2018).

well, which is expressed by integrating equation (A.5) in the r direction. In the range from $r = r'$ to $r = 0$, we obtain the following set of equations for all annular slices:

$$\begin{cases} \frac{1}{dt}\int_{r'-dr}^{r'} (h(r,t'+dt) - h(r,t'))\, rdr + [rq]_{r'-dr}^{r'} = 0 \\ \frac{1}{dt}\int_{r'-2dr}^{r'-dr} (h(r,t'+dt) - h(r,t'))\, rdr + [rq]_{r'-2dr}^{r'-dr} = 0 \\ \qquad\qquad\qquad \vdots \\ \frac{1}{dt}\int_{0}^{dr} (h(r,t'+dt) - h(r,t'))\, rdr + [rq]_{0}^{dr} = 0. \end{cases} \tag{A.6}$$

Summing up all factors of equation (A.6) and considering that there is no influx ($q = 0$) at $r = 0$, the following expression is finally obtained:

$$q(r',t') = \frac{-1}{r'dt}\int_0^{r'} \{h(r,t'+dt) - h(r,t')\}\, rdr, \tag{A.7}$$

where the image of this integration is shown in figure A.1(b). This relation corresponds to equation (3.1) in the main text, which enables us to measure the flux q at a given position by calculating the rate of volumetric change at $t = t'$–$t' + dt$.

Appendix B Logarithmically-increasing time bins

Here, we describe how to choose suitable dt when computing the flux from the obtained experimental data. To calculate an instantaneous flux q in equation (A.7), flows are assumed to be quasi-steady during $t = t'–t' + dt$. Ideally, dt should be a constant infinitesimal time step. In this study, however, a heap is continuously relaxed during vibration, which indicates that the characteristic timescale of the relaxation varies with time. Therefore, in order to accurately measure the flux with a suitable time range, dt must be changed depending on time, or relaxation conditions. In section 3.1, logarithmically-increasing time bins are employed for dt. The reason for this temporal discretisation is explained below.

To specifically express dt that can vary with the relaxation condition, dt is given by $\tau(t)\, d\tilde{t}$, where $\tau(t)$ and $d\tilde{t}$ are the characteristic relaxation time and a dimensionless unit time. Using the characteristic height $H_{\mathrm{ch}}(t)$ and its decreasing rate $\dot{H}_{\mathrm{ch}}(t)$, τ can be written as:

$$\tau(t) \sim \frac{H_{\mathrm{ch}}(t)}{\dot{H}_{\mathrm{ch}}(t)}, \tag{B.1}$$

where one of the most natural options for H_{ch} and $\dot{H}_{\mathrm{ch}}$ is:

$$\begin{aligned} H_{\mathrm{ch}}(t) &= \frac{1}{r_0}\int_0^{r_0} h(r)\, dr \\ \dot{H}_{\mathrm{ch}}(t) &= \frac{dH_{\mathrm{ch}}}{dt}. \end{aligned} \tag{B.2}$$

Figure B.1 shows $\tau(t)$ computed using equations (B.1) and (B.2). The linear data trend in a semi-log plot indicates an exponential growth of $\tau(t)$ as a function of time. From this reason, logarithmically-increasing time bins are employed for dt in this study.

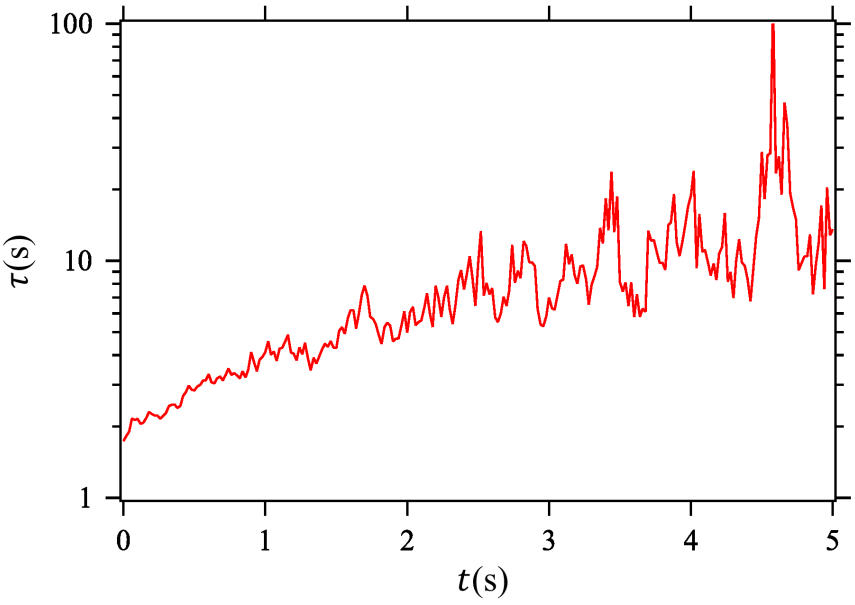

Figure B.1: Characteristic relaxation time $\tau(t)$ computed from the same data as figure 2.3(a). Cited from Supplemental Material of Tsuji et al. (2018).

Appendix C Algorithm of profile pattern matching

Here the way of estimating Δr is explained. Since Δr is defined as the r component of the distance for which a profile moves during Δt, firstly a profile, which is actually inclined along slope, is projected onto the horizontal axis. To this end, as illustrated in figure C.1, a profile $h(r)$ is fitted by a linear function ($g(r) = a_0 + a_1 r$, where a_0 and a_1 are fitting parameters), and then the profile along the r axis $h'(r)$ is created as

$$h'(r) = h(r) - g(r). \tag{C.1}$$

Δr can be determined by finding the position where one-dimensional cross-correlation function $f_{cc}(\delta r)$ between two profiles $h'(r, t)$ and $h'(r, t + \Delta t)$ shows the maximum value. The cross-correlation function is defined as

$$f_{cc}(\delta r) = \frac{1}{H'(t)} \int_{r_s}^{r_e} h'(r, t) h'(r + \delta r, t + \Delta t) dr, \tag{C.2}$$

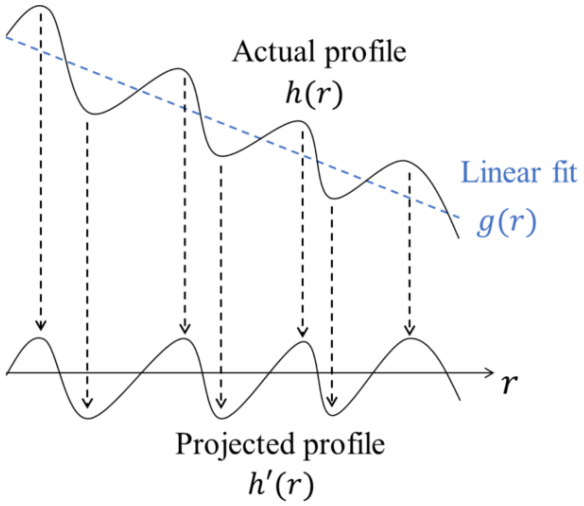

Figure C.1: Schematic image of the projection of a profile onto the horizontal axis. Cited from Tsuji et al. (2019).

where r_s and r_e represent the start- and end-points of the spacial window considered for the analysis, and the normalisation term $H'(t)$ is given by

$$H'(t) = \int_{r_s}^{r_e} h'(r,t)^2 dr. \tag{C.3}$$

Here, $r_e - r_s = 10$ mm is employed as explained in section 3.3.3. Since the correlation function is normalised by $H'(t)$ in equation (C.2), $f_{cc}(\delta r) = 1$ corresponds to the complete match of two profiles. By changing δr systematically, Δr can be estimated, where $f_{cc}(\Delta r)$ shows the peak value of the correlation function. In this study, six different Δt are applied to obtain reliable data, which increase consecutively at intervals of the temporal resolution of the profile measurement by the laser (0.02 s). Hereafter, six different Δt are denoted by Δt_k, and their corresponding Δr are expressed as Δr_k, where $k = 1, 2, \cdots, 6$. Δt_k is given by $\Delta t_0 + 0.02k$ s, where a constant Δt_0 depends on the analysis position r. In general, the surface velocity increases with r as a local slope gets steeper. Therefore, it is preferable for the accurate measurement that smaller Δt_0 is chosen for larger r ranges. Table C.1 shows the list of Δt_0 for various analysis positions ($r = 5, 15, 25, 35$ mm). These values are chosen in order for the typical value of Δr to be a few grain diameter.

Finally, the surface velocity v_{t0} is estimated using the weighted average:

$$v_{t0} = \sum_{k=1}^{6} \left(\frac{\Delta r_k}{\Delta t_k} \cdot \frac{f_{cc}(\Delta r_k)^2}{f_{cc}^{tot}} \right), \tag{C.4}$$

where $f_{cc}^{tot} = \sum_{i=1}^{6} f_{cc}(\Delta r_k)^2$. Note that only the velocity with $f_{cc}(\Delta r_k) > 0.4$ is used to calculate v_{t0} so that the data obtained by low-correlated matching, which could be inaccurate, can be removed. We have confirmed that the result does not change once this threshold value becomes larger than 0.4.

Table C.1: List of Δt_0 for various analysis positions r.

r (mm)	5	15	25	35
Δt_0 (s)	0.12	0.08	0.04	0.00

Appendix D Dependence on simulation parameters

The dependence on four simulation parameters ($k^{(n)}$, $k^{(t)}$, $\eta^{(n)}$, and μ_m) is discussed by showing the relation between depth-averaged velocity $\bar{v}_t$ and slope $|\nabla h|$. Although the choice of these parameters does not affect numerical results significantly as presented below, it would be helpful for future studies to show specific results here. In the following, we independently vary the above four parameters, fixing the others as in table 4.1.

D.1 Normal spring constant

First of all, using various $k^{(n)}$ values, the depth-averaged velocity $\bar{v}_t$ and slope $|\nabla h|$, which are calculated by the same procedure as figure 3.3, are compared in figure D.1(a). Although the data using $k^{(n)} = 10^5$ and 10^6 [mg/d] slightly fluctuate, their error bars are mostly overlapped with those of the data using $k^{(n)} = 10^4$ [mg/d]. This result implies that, in the range of $k^{(n)} \geq 10^4$ [mg/d], simulated particles reach the hard limit, where the result no longer changes. This order is also consistent with the report by Silbert et al. (2001): They simulated granular flows down an inclined plane, and concluded that the variations of flow properties induced by the difference of $k^{(n)}$ are negligible once $k^{(n)}$ exceeds $\sim 10^4$ [mg/d].

D.2 Tangential spring constant

Second, we vary the ratio $k^{(t)}/k^{(n)}$ from 2/7 to 2/3, keeping $k^{(n)} = 10^4$ [mg/d]. Figure D.1(b) shows the result with various $k^{(t)}/k^{(n)}$, which remains unchanged. This independence is also consistent with Silbert et al. (2001). Therefore, $k^{(n)} = 10^4$ [mg/d] and $k^{(t)}/k^{(n)} = 2/7$ are used for the standard setting of spring constants in our DEM simulations.

D.3 Normal viscous coefficient

Next, by tuning the value of $\eta^{(n)}$ with $k^{(n)}$ fixed, the influence of the restitution coefficient e is also investigated here. The restitution coefficient is determined by equation (4.10). Figure D.1(c) shows the result for $e = 0.7$–0.9, which shows no clear difference.

This can be understood in the following sense: As mentioned in section 1.2.1, da Cruz et al. (2005) report that e has no influence on the bulk frictional property in plane shear flows. In fact, the value of μ determined by the fitting of the NDT model (3.8) is little influenced by e as explained in section 5.1.1. Given that the frictional property does not depend on e in our system, the forces considered in the derivation of the NDT model (section 3.2) are not influenced. Therefore, the bulk flow property characterised by $\bar{\nu}_t$ does not depend on e.

D.4 Microscopic friction coefficient

Finally, the dependence on the microscopic friction coefficient μ_m is discussed. According to section 4.2, the angle of repose is not increased once μ_m exceeds 0.6, which suggests that the bulk flow property does not change in this high μ_m limit. From the same reason as the above insensitivity to the restitution coefficient e, the result should not depend on the value of μ_m. To check this, we have conducted the simulation using grains with μ_m = 0.6–1.0, and the result is shown in figure D.1(d). As expected, all of the data do not show a clear difference.

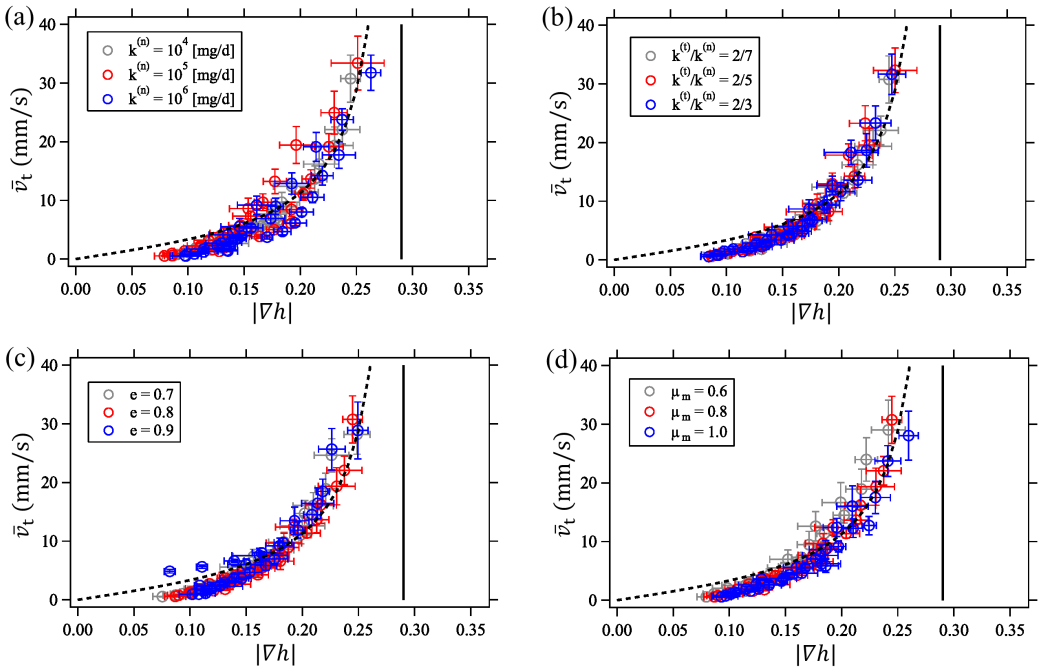

Figure D.1: Dependence on mechanical parameters in DEM simulations. By showing the relation between depth-averaged velocity $\bar{v}_t$ and slope $|\nabla h|$, the independence on (a) normal spring constant $k^{(n)}$, (b) tangential spring constant $k^{(t)}$, (c) restitution coefficient e, and (d) microscopic friction coefficient μ_m is proved in each panel. The black dashed curves and solid lines represent the same ones used in figure 5.2.

Appendix E Derivation of equation (6.8)

Here we show that equation (6.8) can be obtained by solving the partial differential equation (6.7). Firstly, equation (6.7) is simplified by as

$$h(r) = -Q_0 \frac{M_0 - h'(r)^2}{h'(r)}, \tag{E.1}$$

where

$$Q_0 = \frac{q}{c v_{\mathrm{vib}}}, \qquad M_0 = \mu^2, \qquad h' = -|\nabla h|. \tag{E.2}$$

Equation (E.1) has two analytical solutions:

$$r + c_1 = \frac{Q_0}{4}\left\{ \frac{h\left(-h + \sqrt{4{Q_0}^2 M_0 + h^2}\right)}{{Q_0}^2 M_0} + 4\ln\left(h + \sqrt{4{Q_0}^2 M_0 + h^2}\right)\right\} \tag{E.3}$$

$$r + c_2 = \frac{-Q_0}{4}\left\{ \frac{h\left(h + \sqrt{4{Q_0}^2 M_0 + h^2}\right)}{{Q_0}^2 M_0} - 4\ln\left(-h + \sqrt{4{Q_0}^2 M_0 + h^2}\right)\right\}, \tag{E.4}$$

where c_1 and c_2 are integral constants. These solutions are obtained using a computational knowledge engine Wolfram|Alpha [†]. Employing the boundary condition of $h = 0$ at $r = R$ for simplicity, c_1 and c_2 are determined as

$$c_1 = c_2 = -R + Q_0 \ln \sqrt{4{Q_0}^2 M_0}. \tag{E.5}$$

Substituting equation (E.5) into equations (E.3) and (E.4) yields

$$\begin{aligned} r &= R + \frac{h\left(-h + \sqrt{4{Q_0}^2 M_0 + h^2}\right)}{4 Q_0 M_0} + Q_0 \ln\left(\frac{h + \sqrt{4{Q_0}^2 M_0 + h^2}}{\sqrt{4{Q_0}^2 M_0}}\right) \\ &= \xi_1(h) \end{aligned} \tag{E.6}$$

[†]Online service is available from `https://www.wolframalpha.com/`

$$\begin{aligned} r &= R - \frac{h\left(h + \sqrt{4{Q_0}^2 M_0 + h^2}\right)}{4Q_0 M_0} + Q_0 \ln\left(\frac{-h + \sqrt{4{Q_0}^2 M_0 + h^2}}{\sqrt{4{Q_0}^2 M_0}}\right) \\ &= \xi_2(h) \end{aligned} \tag{E.7}$$

Figure E.1 draws two profiles:

$$h = {\xi_1}^{-1}(r) \tag{E.8}$$

$$h = {\xi_2}^{-1}(r), \tag{E.9}$$

where ${\xi_1}^{-1}$ and ${\xi_2}^{-1}$ are defined as inverse functions of ξ_1 and ξ_2. This figure suggests that equation (E.9) should be selected as an expected profile since h is positive in the range of $0 < r < R$. Therefore, ξ_2 corresponds to ξ, which is obtained by substituting equation (E.2) into equation (E.7):

$$\begin{aligned} \xi(h) &= \xi_2(h) \\ &= R - \frac{cv_{\mathrm{vib}}}{4q\mu^2} h \left\{ h + \sqrt{\left(\frac{2q\mu}{cv_{\mathrm{vib}}}\right)^2 + h^2} \right\} + \frac{q}{cv_{\mathrm{vib}}} \ln\left[\frac{cv_{\mathrm{vib}}}{2q\mu} \left\{ -h + \sqrt{\left(\frac{2q\mu}{cv_{\mathrm{vib}}}\right)^2 + h^2} \right\} \right]. \end{aligned} \tag{E.10}$$

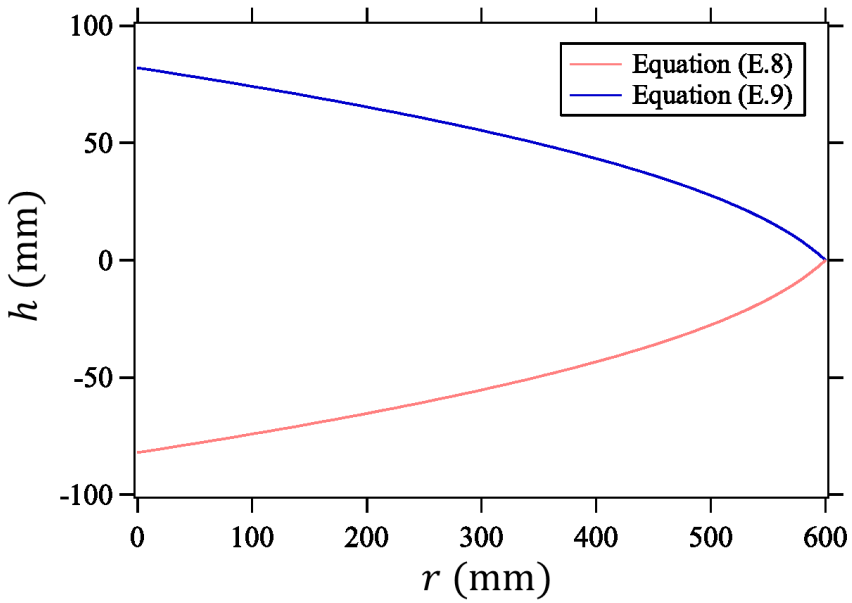

Figure E.1: Comparison between equations (E.8) and (E.9). The values of parameters are the same as those used in section 6.2: $q = 100$ mm^2/s, $c = 0.068$, $v_{\text{vib}} = 47$ mm/s, $\mu = 0.45$, and $R = 600$ mm.

References

Al-Hashemi, H. M. B., Al-Amoudi, O. S. B., 2018. A review on the angle of repose of granular materials. Powder Technology 330, 397–417.

Amon, D. L., Niculescu, T., Utter, B. C., 2013. Granular avalanches in a two-dimensional rotating drum with imposed vertical vibration. Phys. Rev. E 88, 012203.

Ancey, C., Coussot, P., Evesque, P., 1999. A theoretical framework for granular suspensions in a steady simple shear flow. J. Rheol. 43, 1673–1699.

Andreotti, B., Forterre, Y., Pouliquen, O., 2013. Granular Media: Between Fluid and Solid. Cambridge University Press, Cambridge, U.K.

Aoki, K. M., Akiyama, T., Maki, Y., Watanabe, T., 1996. Convective roll patterns in vertically vibrated beds of granules. Phys. Rev. E 54, 874–883.

Bagnold, R. A., 1954. Experiments on a gravity-free dispersion of large solid spheres in a newtonian fluid under shear. Proceedings of the Royal Society of London A: Mathematical, Physical and Engineering Sciences 225, 49–63.

Bak, P., Tang, C., 1989. Earthquakes as a self-organized critical phenomenon. J. Geophys. Res.: Solid Earth 94, 15635–15637.

Bak, P., Tang, C., Wiesenfeld, K., 1987. Self-organized criticality: An explanation of the $1/f$ noise. Phys. Rev. Lett. 59, 381–384.

Baker, J. L., Barker, T., Gray, J. M. N. T., 2016. A two-dimensional depth-averaged $\mu(I)$-rheology for dense granular avalanches. J. Fluid Mech. 787, 367–395.

Baran, O., Ertaş, D., Halsey, T. C., Grest, G. S., Lechman, J. B., 2006. Velocity correlations in dense gravity-driven granular chute flow. Phys. Rev. E 74, 051302.

Barker, T., Schaeffer, D. G., Bohorquez, P., Gray, J. M. N. T., 2015. Well-posed and ill-posed behaviour of the $\mu(I)$ -rheology for granular flow. J. Fluid Mech. 779, 794–818.

Barker, T., Schaeffer, D. G., Shearer, M., Gray, J. M. N. T., 2017. Well-posed continuum equations for granular flow with compressibility and $\mu(I)$-rheology. Proceedings of the Royal Society A: Mathematical, Physical and Engineering Sciences 473, 20160846.

Barton, J. M. H., Buchberger, S. G., 2003. Geometrical analysis of sand piles on small platforms. Phys. Rev. E 68, 011303.

Bates, L., 2006. The need for industrial education in bulk technology. Bulk Solids Handling 26, 464–474.

BenDror, E., Goren, L., 2018. Controls over sediment flux along soil-mantled hillslopes: Insights from granular dynamics simulations. Journal of Geophysical Research: Earth Surface 123, 924–944.

Breu, A. P. J., Ensner, H.-M., Kruelle, C. A., Rehberg, I., 2003. Reversing the brazil-nut effect: Competition between percolation and condensation. Phys. Rev. Lett. 90, 014302.

Buckingham, E., 1914. On physically similar systems; illustrations of the use of dimensional equations. Phys. Rev. 4, 345–376.

Buckingham, E., 1915. The principle of similitude. Nature 96, 396–397.

Caballero-Robledo, G. A., Clément, E., 2009. Rheology of a sonofluidized granular packing. Eur. Phys. J. E 30, 395–401.

Coulomb, C., 1773. In: Memoir de Mathematique et de Physique. Vol. 7. Academie des Sciences, L'Imprimerie Royale, Paris, pp. 343–382.

Cundall, P., Strack, O., 1979. A discrete numerical model for granular assemblies. Géotechnique 29, 47–65.

da Cruz, F., Emam, S., Prochnow, M., Roux, J.-N., Chevoir, F., 2005. Rheophysics of dense granular materials: Discrete simulation of plane shear flows. Phys. Rev. E 72, 021309.

Diodati, P., Marchesoni, F., Piazza, S., 1991. Acoustic emission from volcanic rocks: An example of self-organized criticality. Phys. Rev. Lett. 67, 2239–2243.

Doane, T. H., Roth, D. L., Roering, J. J., Furbish, D. J., 2019. Compression and decay of hillslope topographic variance in fourier wavenumber domain. J. Geophys. Res.: Earth Surface 124, 60–79.

Duran, J., 2000. Sands, Powders, and Grains: An Introduction to the Physics of Granular Materials. Springer, New York, U.S.

Ehrichs, E. E., Jaeger, H. M., Karczmar, G. S., Knight, J. B., Kuperman, V. Y., Nagel, S. R., 1995. Granular convection observed by magnetic resonance imaging. Science 267, 1632–1634.

Eshuis, P., van der Meer, D., Alam, M., van Gerner, H. J., van der Weele, K., Lohse, D., 2010. Onset of convection in strongly shaken granular matter. Phys. Rev. Lett. 104, 038001.

Eshuis, P., van der Weele, K., van der Meer, D., Lohse, D., 2005. Granular leidenfrost effect: Experiment and theory of floating particle clusters. Phys. Rev. Lett. 95, 258001.

Evesque, P., Rajchenbach, J., 1989. Instability in a sand heap. Phys. Rev. Lett. 62, 44–46.

Faraday, M., 1831. On a peculiar class of acoustical figures; and on certain forms assumed by groups of particles upon vibrating elastic surfaces. Phil. Trans. R. Soc. 52, 299–340.

Fassett, C. I., Thomson, B. J., 2014. Crater degradation on the lunar maria: Topographic diffusion and the rate of erosion on the moon. Journal of Geophysical Research: Planets 119, 2255–2271.

Ferdowsi, B., Ortiz, C. P., Jerolmack, D. J., 2018. Glassy dynamics of landscape evolution. PNAS 115, 4827–4832.

Forterre, Y., Pouliquen, O., 2008. Flows of dense granular media. Annual Review of Fluid Mechanics 40, 1–24.

Fujiwara, A., Kawaguchi, J., Yeomans, D. K., Abe, M., Mukai, T., Okada, T., Saito, J., Yano, H., Yoshikawa, M., Scheeres, D. J., Barnouin-Jha, O., Cheng, A. F., Demura, H., Gaskell, R. W., Hirata, N., Ikeda, H., Kominato, T., Miyamoto, H., Nakamura, A. M., Nakamura, R., Sasaki, S., Uesugi, K., 2006. The rubble-pile asteroid itokawa as observed by hayabusa. Science 312, 1330–1334.

Furbish, D. J., Schmeeckle, M. W., Roering, J. J., 2008. Thermal and force-chain effects in an experimental, sloping granular shear flow. Earth Surf. Process. Landforms 33, 2108–2117.

Gabet, E. J., 2003. Sediment transport by dry ravel. Journal of Geophysical Research: Solid Earth 108, 2049.

Garcimartín, A., Maza, D., Ilquimiche, J. L., Zuriguel, I., 2002. Convective motion in a vibrated granular layer. Phys. Rev. E 65, 031303.

Gaudel, N., Kiesgen de Richter, S., 2019. Effect of vibrations on granular material flows down an inclined plane using dem simulations. Powder Technol. 346, 256–264.

GDR MiDi, 2004. On dense granular flows. Eur. Phys. J. E 14, 341–365.

Ghazavi, M.and Hosseini, M., Mollanouri, M., 2008. A comparison between angle of repose and friction angle of sand. The 12th International Conference of International Association for Computer Methods and Advances in Geomechanics, 1272–1275.

Goldhirsch, I., 2003. Rapid granular flows. Annual Review of Fluid Mechanics 35, 267–293.

Gray, J. M. N. T., Edwards, A. N., 2014. A depth-averaged $\mu(I)$-rheology for shallow granular free-surface flows. J. Fluid Mech. 755, 503–534.

Gray, J. M. N. T., Tai, Y.-C., Noelle, S., 2003. Shock waves, dead zones and particle-free regions in rapid granular free-surface flows. J. Fluid Mech. 491, 161–181.

Hayashi, K., Sumita, I., 2017. Low-velocity impact cratering experiments in granular slopes. Icarus 291, 160 – 175.

Heyman, J., Delannay, R., Tabuteau, H., Valance, A., 2017. Compressibility regularizes the $\mu(I)$-rheology for dense granular flows. J. Fluid Mech. 830, 553–568.

Hirata, N., Barnouin-Jha, O. S., Honda, C., Nakamura, R., Miyamoto, H., Sasaki, S., Demura, H., Nakamura, A. M., Michikami, T., Gaskell, R. W., Saito, J., 2009. A survey of possible impact structures on 25143 itokawa. Icarus 200, 486–502.

Iikawa, N., Bandi, M. M., Katsuragi, H., 2015. Structural evolution of a granular pack under manual tapping. J. Phys. Soc. Jpn. 84, 094401.

Iikawa, N., Bandi, M. M., Katsuragi, H., 2016. Sensitivity of granular force chain orientation to disorder-induced metastable relaxation. Phys. Rev. Lett. 116, 128001.

Jackson, R., 1983. Some mathematical and physical aspects of continuum models for the motion of granular materials. In: Meyer, R. E. (Ed.), Theory of Dispersed Multiphase Flow. Academic Press, pp. 291–337.

Jaeger, H. M., Liu, C.-h., Nagel, S. R., 1989. Relaxation at the angle of repose. Phys. Rev. Lett. 62, 40–43.

Jaeger, H. M., Nagel, S. R., Behringer, R. P., 1996. Granular solids, liquids, and gases. Rev. Mod. Phys. 68, 1259–1273.

Jenkins, J. T., Berzi, D., 2012. Kinetic theory applied to inclined flows. Granular Matter 14, 79–84.

Jerolmack, D., Daniels, K., 2019. Viewing earth's surface as a soft-matter landscape. arXiv:1903.04462.

Jop, P., 2015. Rheological properties of dense granular flows. Comptes Rendus Physique 16, 62–72.

Jop, P., Forterre, Y., Pouliquen, O., 2005. Crucial role of sidewalls in granular surface flows: consequences for the rheology. J. Fluid Mech. 541, 167–192.

Jop, P., Forterre, Y., Pouliquen, O., 2006. A constitutive law for dense granular flows. Nature 441, 727–730.

Joseph, D. D., Saut, J. C., 1990. Short-wave instabilities and ill-posed initial-value problems. Theoretical and Computational Fluid Dynamics 1, 191–227.

Kamrin, K., Henann, D. L., 2015. Nonlocal modeling of granular flows down inclines. Soft Matter 11, 179–185.

Katsuragi, H., 2016. Physics of Soft Impact and Cratering. Springer, Tokyo.

Katsuragi, H., Abate, A. R., Durian, D. J., 2010. Jamming and growth of dynamical heterogeneities versus depth for granular heap flow. Soft Matter 6, 3023–3029.

Khefif, S. M., Valance, A., Ould-Kaddour, F., 2018. Spreading of a granular droplet under horizontal vibrations. Phys. Rev. E 97, 062903.

King, P. J., Swift, M. R., Benedict, K. A., Routledge, A., 2000. Surface stability of granular systems under horizontal and vertical vibration: The applicability of a coefficient of friction. Phys. Rev. E 62, 6982–6988.

Knight, J. B., Ehrichs, E. E., Kuperman, V. Y., Flint, J. K., Jaeger, H. M., Nagel, S. R., 1996. Experimental study of granular convection. Phys. Rev. E 54, 5726–5738.

Komatsu, T. S., Inagaki, S., Nakagawa, N., Nasuno, S., 2001. Creep motion in a granular pile exhibiting steady surface flow. Phys. Rev. Lett. 86, 1757–1760.

Kuwano, O., Ando, R., Hatano, T., 2013. Crossover from negative to positive shear rate dependence in granular friction. Geophys. Res. Lett. 40, 1295–1299.

Lagrée, P.-Y., Staron, L., Popinet, S., 2011. The granular column collapse as a continuum: validity of a two-dimensional navier-stokes model with a $\mu(I)$-rheology. J. Fluid Mech. 686, 378–408.

Lemieux, P.-A., Durian, D. J., 2000. From avalanches to fluid flow: A continuous picture of grain dynamics down a heap. Phys. Rev. Lett. 85, 4273–4276.

Liu, C.-h., Jaeger, H. M., Nagel, S. R., 1991. Finite-size effects in a sandpile. Phys. Rev. A 43, 7091–7092.

Lueptow, R. M., Akonur, A., Shinbrot, T., 2000. Piv for granular flows. Experiments in Fluids 28, 183–186.

Michel, P., O'Brien, D., Abe, S., Hirata, N., 2009. Itokawa's cratering record as observed by hayabusa: Implications for its age and collisional history. Icarus 200, 503–513.

Miles, S., Ho, C., 1999. Rigorous landslide hazard zonation using newmark's method and stochastic ground motion simulation. Soil Dyn. Earthq. Eng. 18, 305–323.

Miyamoto, H., Yano, H., Scheeres, D. J., Abe, S., Barnouin-Jha, O., Cheng, A. F., Demura, H., Gaskell, R. W., Hirata, N., Ishiguro, M., Michikami, T., Nakamura, A. M., Nakamura, R., Saito, J., Sasaki, S., 2007. Regolith migration and sorting on asteroid itokawa. Science 316, 1011–1014.

Newmark, N., 1965. Effects of earthquakes on dams and embankments. Géotechnique 15, 139–160.

Nowak, E., Knight, J., Povinelli, M., Jaeger, H., Nagel, S., 1997. Reversibility and irreversibility in the packing of vibrated granular material. Powder Technol. 94, 79–83.

Otsuki, M., Hayakawa, H., 2009. Critical behaviors of sheared frictionless granular materials near the jamming transition. Phys. Rev. E 80, 011308.

Pak, H. K., Behringer, R. P., 1993. Surface waves in vertically vibrated granular materials. Phys. Rev. Lett. 71, 1832–1835.

Pouliquen, O., 1999. Scaling laws in granular flows down rough inclined planes. Phys. Fluids 11, 542–548.

Pouliquen, O., Cassar, C., Jop, P., Forterre, Y., Nicolas, M., 2006. Flow of dense granular material: towards simple constitutive laws. J. Stat. Mech. 2006, P07020.

Pouliquen, O., Chevoir, F., 2002. Dense flows of dry granular material. Comptes Rendus Physique 3, 163–175.

Reynolds, O., 1885. On the dilatancy of media composed of rigid particles in contact. Philos. Mag. 20, 469–481.

Richard, P., Nicodemi, M., Delannay, R., Ribiere, P., Bideau, D., 2005. Slow relaxation and compaction of granular systems. Nature materials 4, 121–128.

Richardson, J. E., Melosh, H. J., Greenberg, R., 2004. Impact-induced seismic activity on asteroid 433 eros: A surface modification process. Science 306, 1526–1529.

Richardson Jr., J. E., Melosh, H. J., Greenberg, R. J., O'Brien, D. P., 2005. The global effects of impact-induced seismic activity on fractured asteroid surface morphology. Icarus 179, 325–349.

Richman, M., 1993. Boundary conditions for granular flows at randomly fluctuating bumpy boundaries. Mechanics of Materials 16, 211–218.

Roering, J. J., 2004. Soil creep and convex-upward velocity profiles: theoretical and experimental investigation of disturbance-driven sediment transport on hillslopes. Earth Surf. Process. Landforms 29, 1597–1612.

Roering, J. J., Kirchner, J. W., Dietrich, W. E., 1999. Evidence for non-linear, diffusive sediment transport on hillslopes and implications for landscape morphology. Water Resour. Res. 35, 853–870.

Roering, J. J., Kirchner, J. W., Sklar, L. S., Dietrich, W. E., 2001. Hillslope evolution by nonlinear creep and landsliding: An experimental study. Geology 29, 143–146.

Roux, J.-N., Combe, G., 2002. Quasistatic rheology and the origins of strain. Comptes Rendus Physique 3, 131–140.

Sánchez, I., Raynaud, F., Lanuza, J., Andreotti, B., Clément, E., Aranson, I. S., 2007. Spreading of a granular droplet. Phys. Rev. E 76, 060301.

Sano, O., 2005. Dilatancy, buckling, and undulations on a vertically vibrating granular layer. Phys. Rev. E 72, 051302.

Savage, S. B., 1984. The mechanics of rapid granular flows. Advances in Applied Mechanics 24, 289–366.

Savage, S. B., Hutter, K., 1989. The motion of a finite mass of granular material down a rough incline. J. Fluid Mech. 199, 177–215.

Schaeffer, D. G., Barker, T., Tsuji, D., Gremaud, P., Shearer, M., Gray, J. M. N. T., 2019. Constitutive relations for compressible granular flow in the inertial regime. J. Fluid Mech. 874, 926–951.

Schofield, A., Wroth, P., 1968. Critical state soil mechanics. Vol. 310. McGraw-Hill London.

Shinoda, A., Fujiwara, S., Niiya, H., Katsuragi, H., 2018. Void structure stability in wet granular matter and its application to crab burrows and cometary pits. Sci. Rep. 8, 15784.

Silbert, L., Landry, J., Grest, G., 2003. Granular flow down a rough inclined plane: Transition between thin and thick piles. Phys. Fluids 15, 1–10.

Silbert, L. E., Ertaş, D., Grest, G. S., Halsey, T. C., Levine, D., Plimpton, S. J., 2001. Granular flow down an inclined plane: Bagnold scaling and rheology. Phys. Rev. E 64, 051302.

Swisher, N. C., Utter, B. C., 2014. Flow profile of granular avalanches with imposed vertical vibration. Granular Matter 16, 175–183.

Taberlet, N., Richard, P., Valance, A., Losert, W., Pasini, J. M., Jenkins, J. T., Delannay, R., 2003. Superstable granular heap in a thin channel. Phys. Rev. Lett. 91, 264301.

Taguchi, Y.-h., 1992. New origin of a convective motion: Elastically induced convection in granular materials. Phys. Rev. Lett. 69, 1367–1370.

Takada, S., Saitoh, K., Hayakawa, H., 2014. Simulation of cohesive fine powders under a plane shear. Phys. Rev. E 90, 062207.

Takizawa, S., Katsuragi, H., 2020. Scaling laws for the oblique impact cratering on an inclined granular surface. Icarus 335, 113409.

Teanby, N. A., 2015. Predicted detection rates of regional-scale meteorite impacts on mars with the insight short-period seismometer. Icarus 256, 49–62.

Tsuji, D., Katsuragi, H., 2015. Temporal analysis of acoustic emission from a plunged granular bed. Phys. Rev. E 92, 042201.

Tsuji, D., Otsuki, M., Katsuragi, H., 2018. Relaxation dynamics of a granular pile on a vertically vibrating plate. Phys. Rev. Lett. 120, 128001.

Tsuji, D., Otsuki, M., Katsuragi, H., 2019. Laboratory experiment and discrete-element-method simulation of granular-heap flows under vertical vibration. Phys. Rev. E 99, 062902.

Tsuji, D., Teanby, N. A., 2016. Europa's small impactor flux and seismic detection predictions. Icarus 277, 39–55.

van der Meer, D., van der Weele, K., Lohse, D., 2004. Coarsening dynamics in a vibrofluidized compartmentalized granular gas. J. Stat. Mech.: Theor. Exp. 2004, P04004.

Yamada, T., 2016. Experimental and modeling study for asteroidal resurfacing process induced by regolith convection. Ph.D. thesis, Nagoya University.

Yamada, T. M., Ando, K., Morota, T., Katsuragi, H., 2016. Timescale of asteroid resurfacing by regolith convection resulting from the impact-induced global seismic shaking. Icarus 272, 165–177.

Yamada, T. M., Katsuragi, H., 2014. Scaling of convective velocity in a vertically vibrated granular bed. Planet. and Space Sci. 100, 79–86.

Zaalouk, A., Zabady, F., 2009. Effect of moisture content on angle of repose and friction coefficient of wheat grain. Misr. J. Agric. Eng. 26, 418–427.

Zhou, Y., Xu, B., Yu, A., Zulli, P., 2002. An experimental and numerical study of the angle of repose of coarse spheres. Powder Technology 125, 45–54.

Zhou, Y. C., Xu, B. H., Yu, A. B., Zulli, P., 2001. Numerical investigation of the angle of repose of monosized spheres. Phys. Rev. E 64, 021301.

Supporting research papers

1. Tsuji, D, Otsuki, M, and Katsuragi, H, *Physical Review Letters* **120**, 128001 (2018) *Relaxation dynamics of a granular pile on a vertically-vibrating plate*

2. Tsuji, D, Otsuki, M, and Katsuragi, H, *Physical Review E* **99**, 062902 (2019) *Laboratory experiment and discrete-element-method simulation of granular-heap flows under vertical vibration*